



HAL
open science

Brain tumor growth modeling: application to radiotherapy

Matthieu Lê

► **To cite this version:**

Matthieu Lê. Brain tumor growth modeling: application to radiotherapy. Other. Université Nice Sophia Antipolis, 2016. English. NNT: 2016NICE4034 . tel-01376688v2

HAL Id: tel-01376688

<https://theses.hal.science/tel-01376688v2>

Submitted on 19 Mar 2020

HAL is a multi-disciplinary open access archive for the deposit and dissemination of scientific research documents, whether they are published or not. The documents may come from teaching and research institutions in France or abroad, or from public or private research centers.

L'archive ouverte pluridisciplinaire **HAL**, est destinée au dépôt et à la diffusion de documents scientifiques de niveau recherche, publiés ou non, émanant des établissements d'enseignement et de recherche français ou étrangers, des laboratoires publics ou privés.

UNIVERSITÉ NICE - SOPHIA ANTIPOLIS
ÉCOLE DOCTORALE STIC
SCIENCES ET TECHNOLOGIES DE L'INFORMATION
ET DE LA COMMUNICATION

THÈSE

pour l'obtention du grade de

Docteur en Sciences

de l'Université de Nice - Sophia Antipolis

**Mention : AUTOMATIQUE, TRAITEMENT DU SIGNAL ET
DES IMAGES**

Présentée et soutenue par

Matthieu LÊ

Modélisation de la Croissance de Tumeurs Cérébrales, Application à la Radiothérapie

Thèse dirigée par Nicholas AYACHE et Hervé DELINGETTE

préparée à l'Inria Sophia Antipolis, projet ASCLEPIOS

soutenue le 23 Juin 2016

Jury:

<i>Rapporteurs :</i>	Elsa ANGELINI	-	Telecom Paristech
	Olivier SAUT	-	CNRS, IMB, Inria (MONC)
<i>Directeur :</i>	Nicholas AYACHE	-	Inria (Asclepios)
<i>Co-Directeur :</i>	Hervé DELINGETTE	-	Inria (Asclepios)
<i>Président :</i>	Nikos PARAGIOS	-	École Centrale Paris (CVC)
<i>Examineurs :</i>	Bjoern MENZE	-	TU München
	Jan UNKELBACH	-	Massachusetts General Hospital, Harvard University

UNIVERSITY OF NICE - SOPHIA ANTIPOLIS
DOCTORAL SCHOOL STIC
SCIENCES ET TECHNOLOGIES DE L'INFORMATION
ET DE LA COMMUNICATION

PHD THESIS

to obtain the title of

PhD of Science

of the University of Nice - Sophia Antipolis

Specialty : CONTROL, SIGNAL, AND IMAGE PROCESSING

Defended by

Matthieu LÊ

Brain Tumor Growth Modeling, Application to Radiotherapy

Thesis Advisors: Nicholas AYACHE and Hervé DELINGETTE

prepared at Inria Sophia Antipolis, ASCLEPIOS Team

defended on June 23, 2016

Jury :

<i>Reviewers :</i>	Elsa ANGELINI	-	Telecom ParisTech
	Olivier SAUT	-	CNRS, IMB, Inria (MONC)
<i>Advisor :</i>	Nicholas AYACHE	-	Inria (Asclepios)
<i>Co-Advisor :</i>	Hervé DELINGETTE	-	Inria (Asclepios)
<i>President :</i>	Nikos PARAGIOS	-	École Centrale Paris (CVC)
<i>Examiners :</i>	Bjoern MENZE	-	TU München
	Jan UNKELBACH	-	Massachusetts General Hospital, Harvard University

Résumé

Les glioblastomes comptent parmi les cas les plus répandus et agressifs de tumeurs cérébrales. Ils sont généralement traités avec une combinaison de résection chirurgicale, suivie de chimiothérapie et radiothérapie. Cependant, le caractère infiltrant de la tumeur rend son traitement particulièrement délicat.

La personnalisation de modèles biophysiques permet d'automatiser la mise au point de thérapies spécifiques au patient, en maximisant les chances de survie. Dans cette thèse nous nous sommes attachés à élaborer des outils permettant de personnaliser la radiothérapie des glioblastomes.

Nous avons tout d'abord étudié l'impact de la prise en compte de l'œdème vasogénique. Notre étude rétrospective se fonde sur une base de donnée de patients traités avec un médicament anti-angiogénique, révélant a posteriori la présence de l'œdème.

Ensuite, nous avons étudié le lien entre l'incertitude due à la segmentation de la tumeur et la distribution de la dose. Pour se faire, nous avons mis au point une méthode permettant d'échantillonner efficacement de multiples segmentations réalistes, à partir d'une unique segmentation clinique.

De plus, nous avons personnalisé un modèle de croissance tumorale aux images IRM de sept patients. La méthode Bayésienne adoptée permet notamment d'estimer l'incertitude sur les paramètres personnalisés.

Finalement, nous avons montré comment cette personnalisation permet de définir automatiquement la dose à prescrire au patient, en combinant le modèle de croissance tumoral avec un modèle de réponse à la dose délivrée.

Les résultats prometteurs présentés ouvrent de nouvelles perspectives pour la personnalisation de la radiothérapie des tumeurs cérébrales.

MOT CLÉS: Imagerie médicale, modèle biophysique, personnalisation, radiothérapie, segmentation, incertitude

Abstract

Glioblastomas are among the most common and aggressive primary brain tumors. It is usually treated with a combination of surgical resection, followed with concurrent chemo- and radiotherapy. However, the infiltrative nature of the tumor makes its control particularly challenging.

Biophysical model personalization allows one to automatically define patient specific therapy plans which maximize survival rates. In this thesis, we focused on the elaboration of tools to personalize radiotherapy planning.

First, we studied the impact of taking into account the vasogenic edema into the planning. We studied a database of patients treated with anti-angiogenic drug, revealing a posteriori the presence of the edema.

Second, we studied the relationship between the uncertainty in the tumor segmentation and dose distribution. For that, we present an approach in order to efficiently sample multiple plausible segmentations from a single expert one.

Third, we personalized a tumor growth model to seven patients' MR images. We used a Bayesian approach in order to estimate the uncertainty in the personalized parameters of the model.

Finally, we showed how combining a personalized model of tumor growth with a dose response model could be used to automatically define patient specific dose distribution.

The promising results of our approaches offer new perspectives for personalized therapy planning.

KEY WORDS: Medical imaging, biophysical model, personalization, radiotherapy, segmentation, uncertainty

Acknowledgments

I would like to warmly thank my advisors Nicholas Ayache and Hervé Delingette for their guidance and support during the last four years. You were always present to help and motivate me with your deep knowledge, unshakable enthusiasm, and strong passion. Hervé, thank you for the time and work you put in this thesis which were determinant to shape it. Nicholas, thank you for your help and vision, and accepting me within the team, where you created a friendly research atmosphere.

I am extremely grateful to Jan Unkelbach for inviting me at the Massachusetts General Hospital for the first year of my thesis. You gave me a wonderful opportunity to work closer to the clinic in Boston. I really appreciated our numerous meetings and your inputs which were necessary to complete this thesis. I would also like to thank Jayashree Kalpathy Cramer, Ender Konukoglu, and Elizabeth Gerstner at the Martinos Center for their help and the data they provided.

I am extremely grateful to Elsa Angelini and Olivier Saut for accepting to be my reviewers, and for spending their precious time to read and correct this manuscript. I warmly thank them for their sharp and constructive comments on my work and for their encouraging compliments. I am also thankful to Bjoern Menze and Nikos Paragios, who accepted to be members of my jury and to come to my defense. It has been a great honor for me to have such an outstanding jury.

My sincere thanks to all my Asclepios colleagues who made the last four years such a pleasure. I want to give a special thanks to my office mates Chloé and Nicolas, and more recently Schuman. I would like to thank Jàn and Loïc L.F. for their wonderful help and insights on machine learning and probabilistic models. Thank you to Bishesh, Marco, Thomas B., and Vikash for the good times spent not skiing in Auron. A special thanks to Mehdi and Rocio who motivated me to join the mud race (unfortunately for them). I would like to thank Loïc C., Marc-Michel, Nina, Pawel, Roch, Sophie, and Thomas D. for the good times shared inside and outside of the lab. The team's atmosphere would not have been as friendly and chill without Alan, Anant, Arnaud, Aurélie, Aziz, Brina, Erin, Ezequiel, Federico, Florent, Florian, Hakim, Héloïse, Hervé L., Hugo, Kristin, Maxime, Mike, Nicolas D., Pauline, Pietro, Raphaël, Sonia, Xavier,...

And of course, I thank Isabelle Strobant, for her support, patience and kind help when organizing my different trips.

Last but not least, I want to thank my family who was always here for me. Regularly coming back to Lyon was always motivating.

Merci à tous!

Contents

1	Introduction	1
1.1	Context	1
1.2	Objectives	1
1.3	Main Contributions and Organization of the Manuscript	2
2	Glioblastoma: Imaging and Therapy	5
2.1	Biological Context	5
2.1.1	Gliomas	5
2.1.2	GBM Growth	7
2.2	Treatment	9
2.3	Glioblastoma Imaging	12
2.4	Radiotherapy Planning	15
3	Glioblastoma: Modeling and Personalization	17
3.1	Tumor Growth Models - State-of-the-Art	17
3.1.1	Reaction-Diffusion Models	18
3.1.2	Effect of Therapy	19
3.1.3	Reaction-Diffusion Equation	19
3.1.4	Multi-Compartment Models	22
3.2	Personalization - State-of-the-Art	26
3.2.1	Anatomical Personalization	26
3.2.2	Inverse Problem	27
4	Multimodal Analysis of Vasogenic Edema in Glioblastoma Patients for Radiotherapy Planning	29
4.1	Introduction	31
4.2	Material and Methods	32
4.3	Results	36
4.3.1	Comparison between the Three Experiments	36
4.3.2	Application to radiotherapy	38
4.4	Conclusion	39
5	Sampling Image Segmentations for Uncertainty Quantification	41
5.1	Introduction	43
5.2	Existing Generative Models of Segmentations	44
5.3	GPSSI	45
5.3.1	Definition	45
5.3.2	Geodesic Distance Map	46
5.3.3	GPSSI	47
5.3.4	Efficient Sampling	48

5.4	Parameter Settings	49
5.5	Segmentation Sampling	51
5.6	GPSSI Extensions	51
5.6.1	Several Neighboring Structures	51
5.6.2	Accounting for Under and Over Segmentation	52
5.6.3	Inclusion or Exclusion of Structures	53
5.6.4	General Covariance Matrix Using Supervoxels	54
5.6.5	Plausibility of the Samples: Evaluation on multiple segmentations	56
5.7	Tumor Delineation Uncertainty in Radiotherapy	58
5.8	Conclusion	60
6	MRI Based Bayesian Personalization of a Brain Tumor Growth Model	61
6.1	Introduction	63
6.1.1	Motivations	63
6.1.2	Clinical Background	64
6.1.3	Modeling: Previous Work	64
6.1.4	Personalization: Previous Work	65
6.1.5	Contributions of the Chapter	66
6.2	Model	66
6.2.1	The Reaction-Diffusion Model	66
6.2.2	Model and MRIs	67
6.3	Simulation	68
6.3.1	Preprocessing of the data	68
6.3.2	Lattice Boltzmann Method	69
6.3.3	Initialization	69
6.4	Personalization	70
6.4.1	Spherical Asymptotic Analysis	71
6.4.2	BOBYQA Optimization	72
6.4.3	Bayesian Personalization	72
6.5	Results	74
6.5.1	Synthetic Case	74
6.5.2	Glioblastoma Patients	75
6.6	Discussion	78
6.7	Perspectives	80
7	Personalized Radiotherapy Planning Based on a Computational Tumor Growth Model	81
7.1	Introduction	83
7.2	Segmentation Samples	84
7.3	Tumor Growth Model	86
7.4	Personalization	86
7.4.1	Scenario 1: One time point only	87

7.4.2	Scenario 2: Two time points	87
7.4.3	Scenario 3: Two time points and segmentation uncertainty	87
7.5	Radiotherapy Planning	88
7.5.1	Cell survival	88
7.5.2	Prescription Dose Optimization	89
7.5.3	IMRT Planning	90
7.6	Results	92
7.7	Second Patient	102
7.8	Conclusion	109
8	Conclusion and Perspectives	111
8.1	Main Contributions	111
8.1.1	Analysis of the Vasogenic Edema	111
8.1.2	Segmentation Sampling for Uncertainty Quantification	112
8.1.3	Bayesian Personalization of a Tumor Growth Model	112
8.1.4	Personalized Radiotherapy Planning	113
8.2	Perspectives	113
8.2.1	Segmentation Sampling	113
8.2.2	Imaging Gliomas	113
8.2.3	Tumor Growth Model Improvements	114
8.2.4	Personalization Strategies	114
8.2.5	Dose Response Model Improvements	114
9	List of Publications	115
9.1	First Author	115
9.2	Co-author	116
9.3	Invited Talks	116
9.4	Challenge Participation	117
9.5	Award	117
A	Complex Tumor Growth Model Implementation	119
A.1	Diffusion	119
A.2	Proliferation	121
A.3	Transitions	121
A.4	Vascularization	121
A.5	Algorithm	122
B	Lattice Boltzmann Method	123
B.1	Reaction-Diffusion Equation	123
B.2	The Lattice Boltzmann Method	123
B.3	Comparison with Analytic Solution	125
	Bibliography	129

List of Figures

2.1	Distribution of Primary Brain and CNS Tumors by Histology	6
2.2	Distribution of Primary Brain and CNS Gliomas by Histology Subtypes	7
2.3	Glioblastoma occupying a large portion of the right hemisphere	8
2.4	Glioblastoma histologic slice	8
2.5	Angiogenesis process	9
2.6	Typical therapy schedule	9
2.7	T2-FLAIR before and after resection	10
2.8	Gantry and patient's couch for photon therapy	10
2.9	T2-FLAIR before and after anti-angiogenic therapy	11
2.10	MRI sequences used for diagnosis and treatment planning	12
2.11	Contrasts observed on MRIs for glioblastomas	13
2.12	Structures of the glioblastoma	14
2.13	Fractional anisotropy image	14
2.14	Radiotherapy planning	16
3.1	3D simulation of a tumor growth	20
3.2	1D simulations with different invisibility indexes	21
3.3	1D simulations with different speed	21
3.4	Relationship between MRIs and tumor cell density	22
3.5	Axial slice for the multi-compartment model simulation	23
3.6	Coronal slice for the multi-compartment model simulation	24
3.7	Sagittal slice for the multi-compartment model simulation	24
3.8	Segmentations of the structures of interest	27
4.1	Response to anti-angiogenic therapy for two patients	31
4.2	The distribution of responsive and non responsive voxels to antian- giogenic therapy	33
4.3	Example of some of the features used for the learning	35
4.4	Area under the ROC curve	36
4.5	Feature importance	36
4.6	DICE coefficient	37
4.7	Segmentation of vasogenic edema	38
4.8	Radiotherapy plans taking into account the presence of vasogenic edema	39
5.1	Segmentation samples using STAPLE and the log-odds.	45
5.2	Segmentation samples using GPSSI	46
5.3	Computation time and comparison with the ground truth for GPSSI sampling algorithms	47
5.4	Relationship between samples variability and GPSSI parameters	50
5.5	Selection of a region of confidence for the segmentation samples	51

5.6	Sampling two non-overlapping structures	52
5.7	Excluding regions from the segmentation samples	53
5.8	Using supervoxels to define spatially varying correlation lengths	54
5.9	Segmentation samples using spatially varying correlation lengths	56
5.10	Comparison between segmentation samples and several expert segmentations	57
5.11	Segmentation sampling for radiotherapy planning uncertainty quantification	59
6.1	Brain MRI and tumor growth model personalization	63
6.2	Preprocessing pipeline	68
6.3	Swanson's personalization method	70
6.4	Invisibility index and speed of growth function of the abnormalities radii	70
6.5	Synthetic tumor growth	73
6.6	Comparison with grid samples	74
6.7	Personalization of the synthetic case	75
6.8	Maximum a posteriori fit for two patients	76
6.9	Personalization of the seven patients	79
6.10	Uncertainty in the personalization	80
7.1	Summary of the method: the personalization of a tumor growth model is combined with a dose response model to optimize the prescription dose	84
7.2	Clinical data used for the personalization and MAP tumor cell density	85
7.3	Segmentation samples used for the personalization	92
7.4	Histogram of the invisibility index λ	93
7.5	Posterior density of the joint probability $P(D, \rho S)$	94
7.6	Visualization of the 3D tumor cell density profile extracted along 2 lines	94
7.7	MAP, mean, and standard deviation of the tumor cell density	95
7.8	Prescription MAP doses for the clinical plan and the three different personalized scenarios	96
7.9	IMRT MAP doses for the clinical plan and the three different personalized scenarios	97
7.10	Prescription probabilistic doses for the clinical plan and the three different personalized scenarios	98
7.11	IMRT probabilistic doses for the clinical plan and the three different personalized scenarios	99
7.12	DICE coefficient of the dose for the three different scenarios	100
7.13	Prescription and IMRT corrected doses	100
7.14	Dose volume histogram for the brainstem and the target volume	101
7.15	Surviving tumor cell density after therapy	101
7.16	Segmentation samples used for the personalization	102

7.17	Histogram of the invisibility index λ	103
7.18	Posterior density of the joint probability $P(D, \rho S)$	103
7.19	MAP, mean, and standard deviation of the tumor cell density	104
7.24	DICE coefficient of the dose for the three different scenarios	104
7.20	Prescription MAP doses for the clinical plan and the three different personalized scenarios	105
7.21	IMRT MAP doses for the clinical plan and the three different personalized scenarios	106
7.22	Prescription probabilistic doses for the clinical plan and the three different personalized scenarios	107
7.23	IMRT probabilistic doses for the clinical plan and the three different personalized scenarios	108
7.25	Prescription and IMRT corrected doses	109
7.26	Dose volume histogram for the brainstem and the target volume	110
B.1	Lattice Boltzmann Method, D3Q7 scheme	125
B.2	Lattice Boltzmann Method, boundary conditions	125
B.3	Comparison between analytic solution and LBM simulation	127
B.4	Dice coefficient between analytic solution and LBM simulation	128

List of Tables

3.1	Equations of the complex multi-compartment model of brain tumor growth	25
3.2	Parameters used for the simulation of the multi-compartment model	26
6.1	Results of the personalization on seven patients	78
7.1	Objective function parameters for the IMRT optimization.	91

Introduction

Contents

1.1	Context	1
1.2	Objectives	1
1.3	Main Contributions and Organization of the Manuscript	2

1.1 Context

The mathematical modeling of brain tumor growth has been the topic of many studies in the last 30 years. With the most recent results came the hope that personalizing such computational models on specific patients could help better understand the disease, predict the future behavior of the tumor, assess the impact of therapy, and personalize therapy plans. With no less than 60, 000 patients newly diagnosed with brain tumors each year in the United States [Dolecek et al., 2012], this could have important beneficial impact [Coons, 1999].

With roughly 10, 000 new cases each year in the United States, glioblastoma is the most common and aggressive sub-type of primary brain tumors. Despite the recent advances in therapy planning, the prognosis remains very poor, with a 1 year survival rate of 35%. The mathematical modeling of glioblastoma is made difficult by the infiltrative nature of the disease; the relationship between the routinely acquired Magnetic Resonance Images (MRIs) and the presence of tumor cells is not well understood.

Radiation therapy is one of the most effective therapeutic course of action against the progression of glioblastoma; it is proposed to every single patient. However, the infiltrative nature of the disease, and the difficulty to analyze MRIs, make it hard to define consistent and personalized radiotherapy plans. To try to alleviate this issues, different guidelines have been issued by several organizations [Mason et al., 2007]. However, most of the decision making is left at the discretion of the radiotherapist.

1.2 Objectives

In this thesis, we focus on modeling the growth of glioblastoma, the most virulent primary brain tumor. We investigate the possibility of defining consistent, patient-

specific radiotherapy plans based on the personalization of a tumor growth model. The main questions we investigated are:

- What parts of the tumor is the MRI revealing ?
- How can we take into account the uncertainty in the tumor segmentation?
- Can we personalize brain tumor growth models to a patients MRI, while taking into account the uncertainty in the parameters and the input of the model ?
- Can we use tumor growth models to automatically define consistent and personalized radiation therapy plans ?

1.3 Main Contributions and Organization of the Manuscript

The main contributions of our work are the following:

- We present the problem of detecting the vasogenic edema, and its implication on radiotherapy planning.
- We present a method to sample plausible segmentations from a single expert one. This is used to assess the uncertainty in radiotherapy planning due to the segmentation process.
- We present a method for the Bayesian personalization of a tumor growth model. This method allows one to personalize a model to patients' MRIs, while providing a quantification of the uncertainty in the personalization.
- We present a method to propose automatic, consistent, and personalized radiotherapy plans, which take into account the uncertainty in the parameters of the model, as well as the uncertainty in the clinician segmentations of the tumor.

The thesis is organized as follow:

Chapter 2 provides general information on brain tumors, and the processes involved in tumor progression. We present the different MRI modalities which are used to diagnose, grade, and describe brain tumors. An overview of current therapeutic course of action is presented, with a focus on radiation therapy.

Chapter 3 presents the state-of-the-art in tumor growth modeling, and model personalization. The emphasis is put on the presentation of the reaction-diffusion model and its variations. The recent advances in glioblastoma modeling is presented with the introduction of a complex multi-compartment model. We present the different strategies that have been used in the model personalization communities,

from direct optimization to Bayesian inference.

Chapter 4 formulates the problem of detecting the vasogenic edema of glioblastomas. Distinguishing vasogenic edema from infiltrative tumor could have impact on improving radiotherapy planning. In this chapter we study a data set of 17 glioblastoma patients treated with anti-angiogenic therapy for which a fast decrease of T2 FLAIR hypersignal is observed, which indicates the resolution of vasogenic edema. We investigate if multimodal MRI acquisitions including diffusion tensor imaging can distinguish between vasogenic edema and tumor infiltration prior to therapy. Using a random forest classifier, we show that, in this study, morphological information based on the contrast enhanced T1 image explains up to 75% of the extent of vasogenic edema. The information from different imaging modalities did not significantly improve the classification. We then show that delineating the vasogenic edema prior to therapy can have substantial impact on radiotherapy target delineation, leading to smaller treatment volumes and reducing potentially harmful radiation dose to normal brain tissue.

Chapter 5 presents a method to automatically produce plausible image segmentation samples from a single expert segmentation. A probability distribution of image segmentation boundaries is defined as a Gaussian process, which leads to segmentations that are spatially coherent and consistent with the presence of salient borders in the image. The proposed approach is computationally efficient, and generates samples which are visually plausible. The sample variability is mainly governed by a parameter which may be correlated with a simple DICE score, or easily set by the user from the definition of probable regions of interest. The method is extended to the case of several neighboring structures, but also to account for under or over segmentation, and the presence of excluded regions. We also detail a method to sample segmentations with more general non-stationary covariance functions which relies on supervoxels. Furthermore, we provide some insights on the plausibility of the generated segmentations by comparing them with several manual clinical segmentations of a brain tumor. Finally, we show how this approach can have useful applications in the field of uncertainty quantification of radiotherapy planning, where segmentation sampling is applied to both the clinical target volume and the organs at risk.

Chapter 6 presents our approach for the Bayesian personalization of a brain tumor growth model, which is based on the reaction-diffusion equation model. Studies suggests that the diffusion coefficient and the proliferation rate can be related to clinically relevant information, namely the invisibility index and the speed of growth. However, estimating the parameters of the reaction-diffusion model is difficult because of the lack of identifiability of the parameters, the uncertainty in the tumor segmentations, and the model approximation, which cannot perfectly capture the complex dynamics of the tumor evolution. Our approach aims at analyzing the uncertainty in the patient specific parameters of a tumor growth model,

by sampling from the posterior probability of the parameters knowing the magnetic resonance images of a given patient. The estimation of the posterior probability is based on: i) a highly parallelized implementation of the reaction-diffusion equation using the Lattice Boltzmann Method (LBM), and ii) a high acceptance rate Monte Carlo technique called Gaussian Process Hamiltonian Monte Carlo (GPHMC). We compare this personalization approach with two commonly used approaches based on the spherical asymptotic analysis of the reaction-diffusion model, and on a derivative-free optimization algorithm. We demonstrate the performance of the method on synthetic data, and on seven patients with a glioblastoma, the most aggressive primary brain tumor. This Bayesian personalization produces more informative results. In particular, it provides samples from the regions of interest and highlights the presence of several modes for some patients. In contrast, previous approaches based on optimization strategies fail to reveal the presence of different modes, and correlation between parameters.

Chapter 7 combines a computational model of brain tumor growth with a dose response model to optimize radiotherapy planning. The Bayesian personalization of the growth model to patients' magnetic resonance images (MRIs) takes into account the uncertainty in the model parameters, together with the uncertainty in the segmentations of the tumor on the different MRI modalities. We present and compare three different scenarios. In the first one, we only consider one MRI acquisition before therapy, as it would usually be the case in clinic. In the second one, we use two time points in order to personalize the model and plan radiotherapy. In the third one, we include the uncertainty in the segmentation process. Based on those different scenarios, we proposed three principled approaches to compute the prescription dose based on the probabilistic distribution of the tumor cell density. First, we minimize the surviving fraction of tumor cells after irradiation in the most probable case. Second, we minimize the expected survival fraction tumor cells after irradiation. Third, we present an approach to correct the prescription dose to take into account the presence of adjacent organs at risk. Finally, we present Intensity Modulated Radiation Therapy (IMRT) of the three prescription doses. This method allows to automatically generate prescription doses conformal to the targeted tumor. We present the results of our approach on two patients diagnosed with high grade glioma. We detail the results in terms of dose volume histograms of the target volume and organs at risk.

Chapter 8 summarizes the main contributions of the thesis, and presents the perspectives of this work.

Appendix A presents the details of the numerical discretization to implement the complex multi-compartment model presented in Chapter 3.

Appendix B presents the details of the implementation of the Lattice Boltzmann Method as well as some results on the precision of the algorithm.

Glioblastoma: Imaging and Therapy

Contents

2.1 Biological Context	5
2.1.1 Gliomas	5
2.1.2 GBM Growth	7
2.2 Treatment	9
2.3 Glioblastoma Imaging	12
2.4 Radiotherapy Planning	15

2.1 Biological Context

A tumor growth mathematical model is a phenomenological approximation of extremely complex biological mechanisms. Therefore, to understand the pros and cons of the various mathematical approaches, we first provide a biological description of the tumor growth process. The focus of this work is on modeling glioblastomas, the most common type of brain tumors. For more detailed explanations, one can refer to [Ray, 2009, Coons, 1999].

2.1.1 Gliomas

Contrary to metastatic tumors, which develop from one organ and spread to another, primary brain tumors directly originate from brain cells. Over a hundred types of primary brain tumors can be identified depending on the type of cells they come from, their degree of malignancy, and the area of the brain they are invading [CancerResearchUK, 2014].

Gliomas account for 30% of primary brain and central nervous system (CNS) tumors (see Figure 2.1). The exact mechanisms at the origin of the glioma formation are not well understood. Currently, two main theories are dominant: the mutational theory and the cancer stem cell theory [Carrabba et al., 2010]. According to the **mutational theory**, a cascade of mutations from glial cells leads to the uncontrolled development of gliomas. Recently, the **cancer stem cell theory** has provided a new perspective on the tumor development. Briefly, the mutation of a single stem

cell may be responsible for the tumor. It leads to a population of cancer stem cells (self-renewable, asymmetrical division, potential for differentiation) and of tumor cells derived from the cancer stem cells (ability to differentiate, but incapacity to initiate the tumor growth).

In this work we will focus on modeling glioblastomas, which is a subtype of astrocytomas. Astrocytomas represent the most common type of gliomas [DeAngelis, 2001]. They can either be low grade or high grade, and very well localized or extremely diffused. These tumors can be described following the World Health Organization (WHO) grade [Louis et al., 2007]:

Grade I: Pilocytic astrocytomas are well circumscribed and non-infiltrative. They can be cured with complete surgical resection.

Grade II: Diffuse astrocytomas are relatively slow growing, usually considered benign. These tumors are infiltrative and make surgery difficult, with high probability of recurrences.

Grade III: Anaplastic astrocytomas are undifferentiated and carry poor clinical prognosis.

Grade IV: Glioblastomas multiforms (GBM) are the most common glioma - at least 50% of the recorded cases (see Figure 2.2) and an incidence of 3.19 per 100,000 [Dolecek et al., 2012]. They grow extremely rapidly and extend to other parts of the brain. This is the most malignant primary brain tumor.

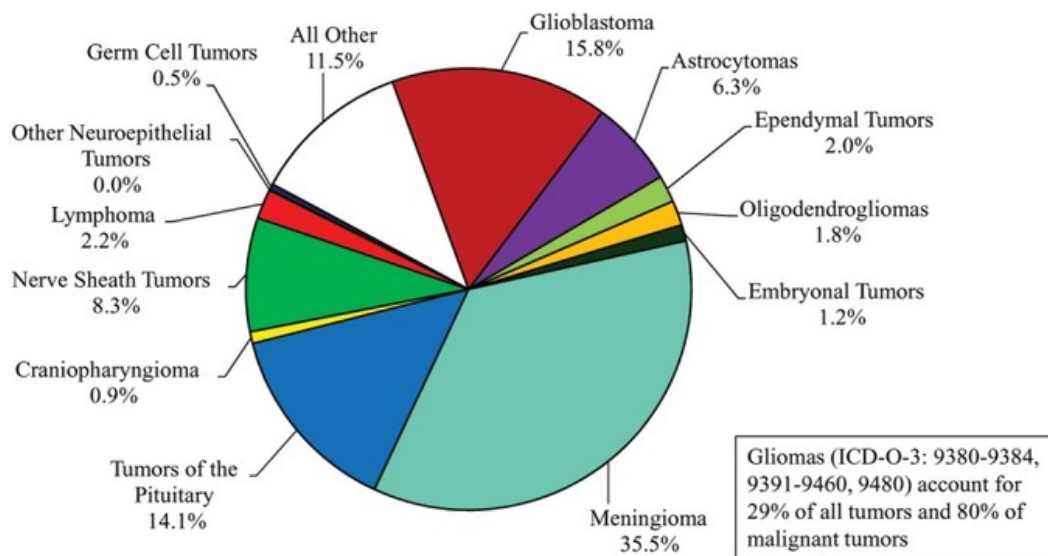


Figure 2.1: Distribution of primary brain and central nervous system tumors by histology (N = 311,202). Gliomas include astrocytoma, glioblastoma, oligodendroglioma, ependymoma, mixed glioma, malignant glioma, and other more rare histologies. Picture taken from [Dolecek et al., 2012].

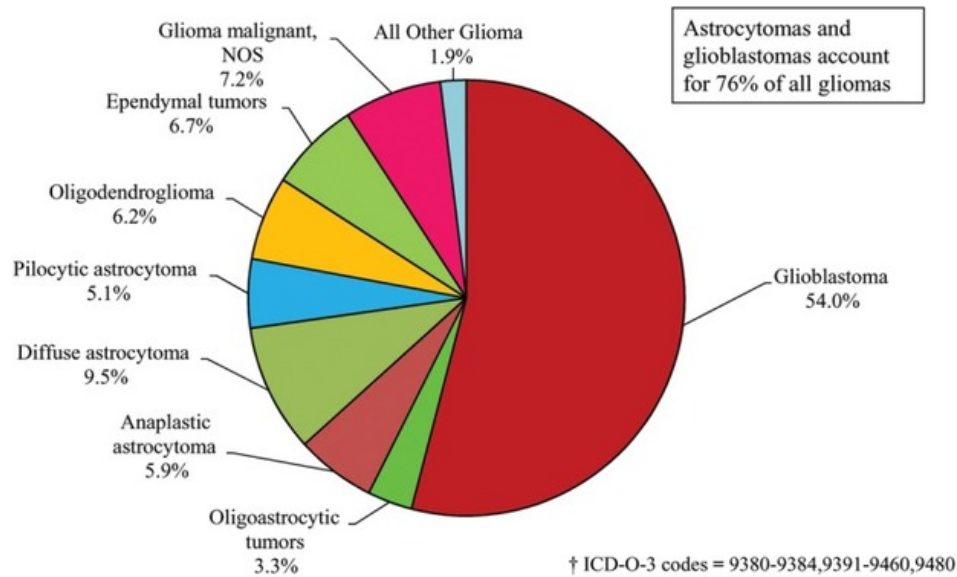


Figure 2.2: Distribution of primary brain and central nervous system gliomas by histology subtypes (N = 90,828). Picture taken from [Dolecek et al., 2012].

The first two grades are referred to as low grade while grade III and IV are high grades. The median survival time for low grade astrocytomas is 7.5 years. Patients with grade III astrocytoma have a median survival time of 18 months with treatments. Individuals with GBM have a median survival time of 17 weeks without treatment, 30 weeks with radiation, and 37 weeks with surgical removal followed by radiation [MDguidelines, 2014].

2.1.2 GBM Growth

Glioblastomas are characterized by a high heterogeneity of tumor cell population which makes them "multiforme" (Figure 2.3). Tumor cell necrosis can be found in the center of the tumor (Figure 2.4a) [Ray-Chaudhury, 2010]. The proliferative cancerous cells are at the periphery of the necrotic core, along with microvasculature proliferation, called **angiogenesis** (Figure 2.4b). In every occurrence, tumor cells can be found infiltrating the white matter tracts in the periphery of the tumor, in regions of the brain parenchyma which appear normal on MRIs. Indeed, GBM is a highly diffusive malignancy, which makes the complete surgical resection impossible.

Angiogenesis is a phenomenon specific to grade IV gliomas (Figure 2.5). This sprouting of new blood vessels is required for the growth, progression and development of the tumor [Choudhury et al., 2010]. Angiogenesis is extremely complex. It involves various molecular signaling pathways triggered by the over-expression of angiogenic factors or by hypoxia, the lack of oxygen. The involved events are the degradation of the basement membrane, the proliferation and migration of endothelial cells, and the reorganization into a functional but chaotic vascular network [Jansen et al., 2004]. Briefly, a chemical signal is sent by the tumor cells to

the surrounding blood vessels. This signal consists of proteins - mainly the vascular endothelial growth factor, VEGF - which stimulates the growth of blood vessels toward the tumor. This new vascular network is chaotic and responsible for the disruption of the blood brain barrier.

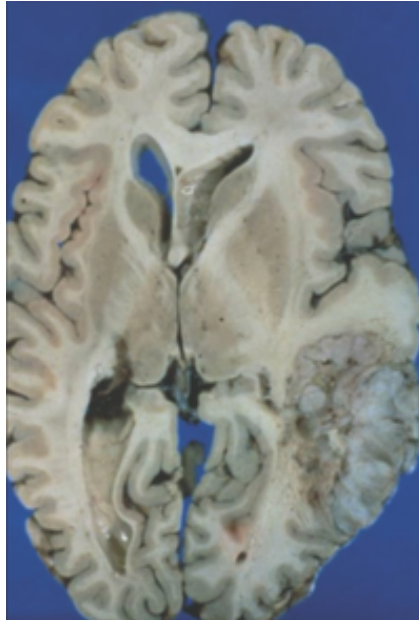


Figure 2.3: Glioblastoma occupying a large portion of the right hemisphere. Foci of necrosis and hemorrhage contributing to the "multiforme" appearance. Picture from [Ray-Chaudhury, 2010]

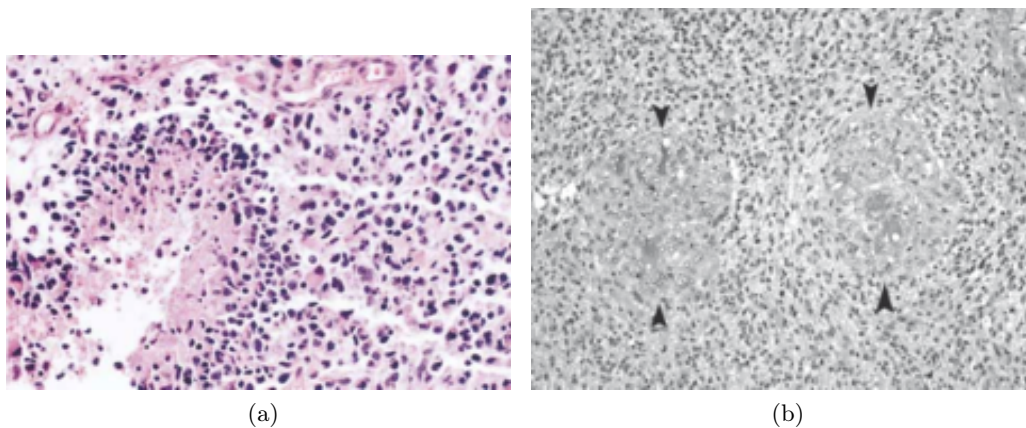


Figure 2.4: a) GBM is characterized by necrosis with cells arranged around the edge of the necrotic tissue. Hematoxylin and eosin staining. Vascular proliferation is apparent at the top of the image. Picture from [DeAngelis, 2001]. b) Complex small vasculature (arrowheads) with numerous lumens and many nuclei within the walls. Hematoxylin and eosin staining, $\times 20$. Picture from [Welsh, 2010].

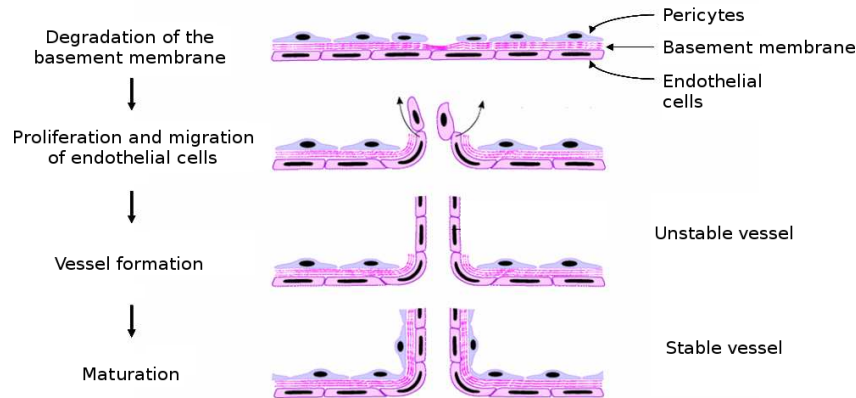


Figure 2.5: Overview of the angiogenesis process. Endothelial cells degrade the basement membrane, proliferate and migrate following the VEGF gradient to form a new chaotic vasculature. Picture from [Billy, 2009].

2.2 Treatment

Despite tremendous research efforts in the last decades, prognosis remains severely dismal for GBM patients, with a median survival of 37 weeks under therapy. We expose the main strategies for GBM management.

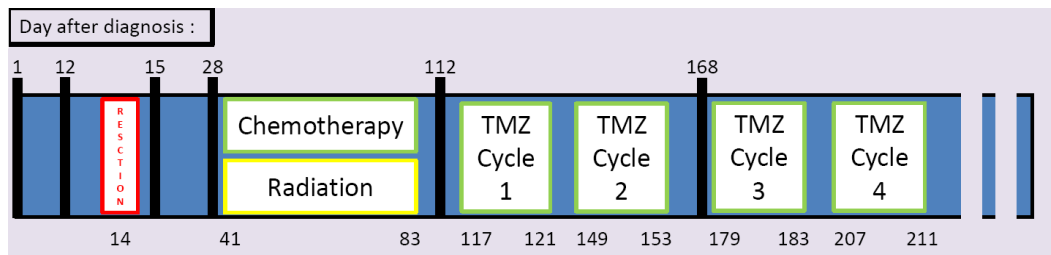


Figure 2.6: Typical therapy schedule with resection and concurrent radiation and chemotherapy. Days after diagnosis are indicated as well as MRI acquisition visits (thick vertical bars). The radiotherapy plan is set to 60 Gy on the clinical target volume fractionated into 6 weeks of treatment, 2 Gy delivered per week day. The chemotherapy is a Temozolomide cycle of around 200 mg/m²/d during a week.

Surgery: Surgery is at the core of diagnosis (biopsy) and tumor management (sub- or gross total resection). Although biopsies are always performed to confirm diagnosis, resection can be discarded. When the tumor has invaded eloquent brain areas, one may advise against a craniotomy. It has been shown that gross total resection leads to an increase in progression-free survival on a restrained number of 416 GBM patients [Lacroix et al., 2001]. A craniotomy helps decrease the tumor burden, the mass effect, and the requirement for steroids [Ray, 2009] (see Figure 2.7).

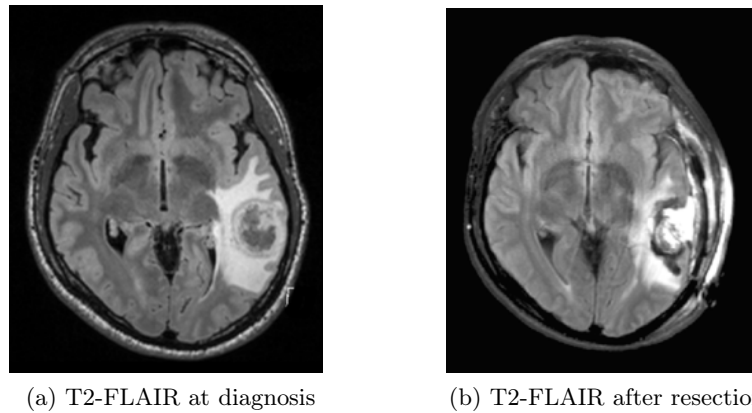


Figure 2.7: T2-FLAIR images showing the resection of the tumor between the diagnostic (Figure 2.7a) and the follow-up image (Figure 2.7b) after 15 days

Radiotherapy: This is usually the second step of treatment. Photons or charged particles (e.g. protons, electrons, ions,...) are delivered to the tumor to kill the malignant cells left after surgery. In the case of glioblastoma, the clinical standard is photon external beam radiotherapy (see the operating room on Figure 2.8). The dose is delivered using an external source of radiation, a linear accelerator (LINAC) in the case of photon therapy. A clinical target volume is defined based on the gross tumor volume observable on the different magnetic resonance image modalities. 60 Gy (joule per kilogram) are delivered to the clinical target volume in fractions of 2 Gy per week day over 6 weeks. The benefit of radiotherapy for the management of malignant gliomas is strongly supported by several clinical trials [Walker et al., 1978, Walker et al., 1979, Kristiansen et al., 1981]. Since radiotherapy planning is at the core of this work, more detailed explanations will be provided in Section 2.4.



Figure 2.8: Gantry and patient's couch for photon therapy. Picture from [radiologyinfo, 2016].

Chemotherapy: Chemotherapy agents kill highly mitotic cells, one of the key characteristics of tumor cells. Several studies showed a significant improvement of combined chemotherapy and radiotherapy followed by chemotherapy only when compared to radiotherapy alone [Stupp et al., 2002, Mirimanoff et al., 2006]. The most widely used chemotherapy agent is Temozolomide (TMZ). TMZ is first administered during radiotherapy (75 mg/m²/d 7 days per week during 6 weeks) followed by a TMZ monotherapy (200 mg/m²/d 5 days per week every 28 days).

Anti-angiogenic therapy: Bevacizumab is a molecular therapy targeting the angiogenesis process. It blocks the molecular pathways triggered by brain tumor to force the sprouting of new blood vessels. Although the advantage of using Bevacizumab alone is not clear, a clear response from GBM patients has been observed [Cloughesy et al., 2008] (see a representative patient on Figure 2.9). When effective, the therapy normalizes the newly formed blood vessels and leads to a large resolution of the edema.

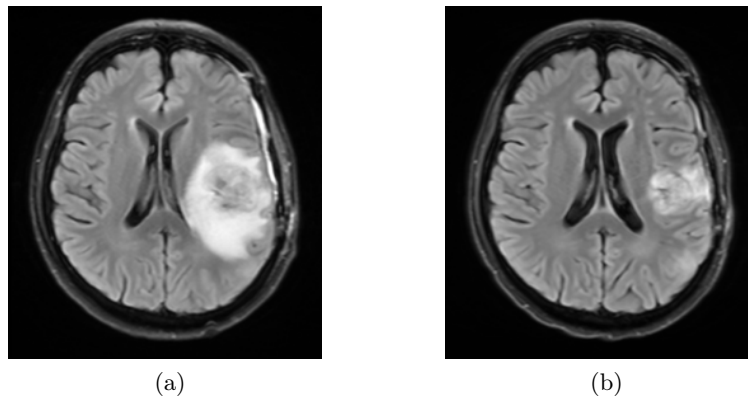


Figure 2.9: T2-FLAIR images before (Figure 2.9a) and after 50 days of anti-angiogenic therapy (Figure 2.9b) .

Those procedures are the mainstream therapeutic acts to control tumor growth. However, none of them are entirely satisfying. It is known that the surgical removal of the tumor never allows for an entire extraction of tumor cells, due to their diffusion ability. Furthermore, some tumor cells are radioresistant and will not be affected by the radiotherapy. Finally, chemotherapy is an extremely severe therapy with numerous side effects (depression of the immune system, fatigue,...). Other types of therapies are being investigated. They mainly focus on finding the correct schedule for the different types of existing therapies, or on blocking the molecular pathways of the brain tumor progression.

2.3 Glioblastoma Imaging

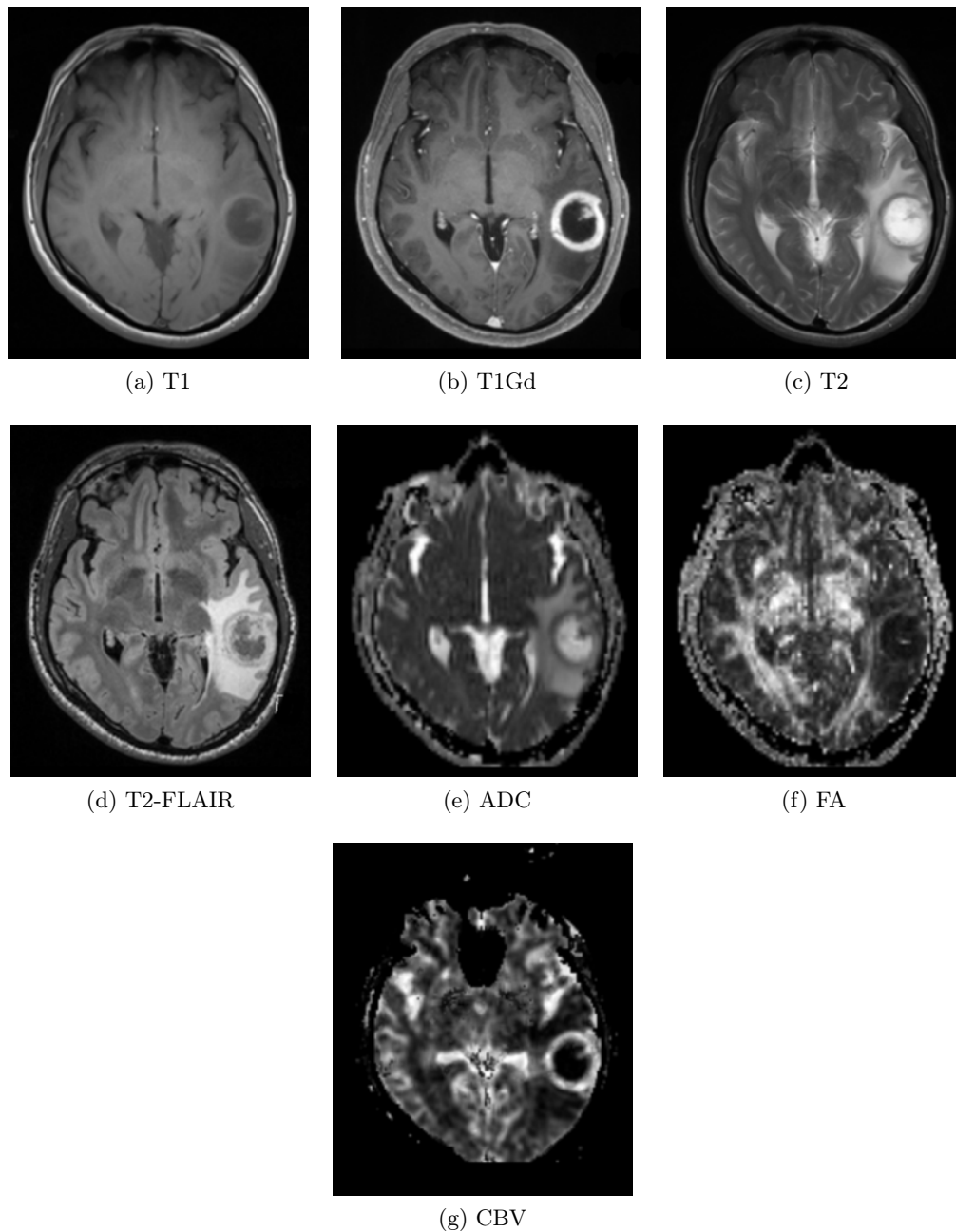


Figure 2.10: MRI sequences used for diagnosis and treatment planning co-registered for one representative GBM patient. 2.10a: T1, 2.10b: T1 with contrast agent (Gadolinium), 2.10c: T2, 2.10d: T2 Fluid Attenuation Inversion Recovery (FLAIR), 2.10e: Average Diffusion Coefficient (ADC), 2.10f: Fractional Anisotropy (FA), 2.10g: Cerebral Blood Volume (CBV),

Although biopsy is the most reliable diagnosis tool, magnetic resonance images (MRI) play a great role in the understanding of brain tumors. Macroscopic features visible on the different sequences of MRI allow the grading, as well as the scheduling of therapy. The main imaging sequences which are routinely acquired will be presented. For further details on the physics behind the MRI, one can refer to [Tofts, 2003].

The most common MRI sequences are T1 (Figure 2.10c) and T2 (Figure 2.10a) weighted images. The GBM abnormality appears hypo-intense on T1 weighted images, and hyper-intense on T2 weighted images (Figure 2.11). Gadolinium contrast agent can be administered to the patient in order to acquire T1 with contrast agent weighted images (T1Gd on Figure 2.10b). This sequence reveals the hyper-intense vasculature of the tumor while the rest of the tumor is hypo-intense. T2 weighted FLAIR images (T2-FLAIR on Figure 2.10d) stands for Fluid Attenuation Inversion Recovery T2 images. It is similar to T2 images but with a better contrast due to the attenuation of the signal coming from the cerebro-spinal fluid (CSF) which then appears hypo-intense.

For diagnosis and therapy planning, the usual delineated structures of the tumor are the necrotic core, the proliferative rim and the edema. The necrotic core and the proliferative rim are visible on the T1Gd MRI (Figure 2.12a). On the T2 FLAIR (Figure 2.12b), one can delineate the edema of the tumor. The Computational Tomography (CT) image is also usually acquired (Figure 2.14e middle). It is particularly useful since the Hounsfield unit of the CT are related to the electron density which is used for radiotherapy dose calculations.

	T1	T1Gd	T2	T2 FLAIR
Cerebrospinal Fluid	Black	Black	White	Black
White Matter	Light Grey	Light Grey	Dark Grey	Dark Grey
Grey Matter	Dark Grey	Dark Grey	Light Grey	Light Grey
Necrotic Core	Black	Black	White	White
Proliferative Rim	Dark Grey	White	White	White
Edema	Dark Grey	Dark Grey	White	White

Figure 2.11: Table of contrast for the healthy (cerebrospinal fluid, white matter, gray matter) and cancerous (necrotic core, proliferative rim, edema) tissue. This schematic view shows the specificity of the four main MRI sequences with 4 contrast levels from hypo-intense (black) to hyper-intense (white).

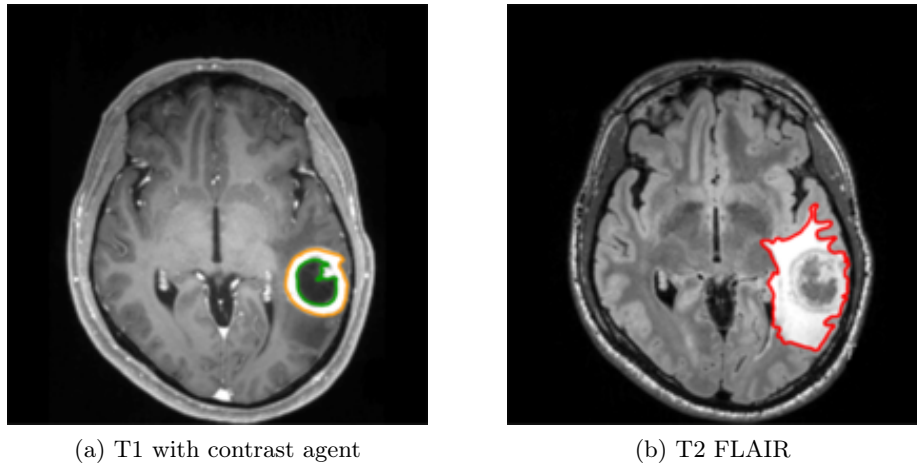


Figure 2.12: For therapy and diagnosis, the structures of the tumors are delineated. 2.12a: The necrotic core (green) and the proliferative rim (orange) are most visible on the T1Gd. 2.12b: The edema red is most visible on the T2 FLAIR.

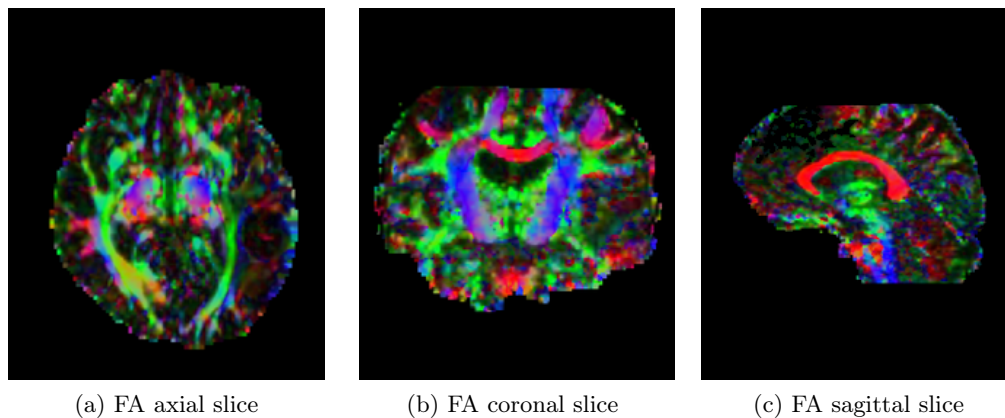


Figure 2.13: FA maps on the three classic orientation. The color code corresponds to the direction of the principal component of the diffusion tensor: green in the x direction, red in the y direction and blue in the z direction.

Other sequences are routinely used. We can notably mention scalar maps coming from diffusion tensor images. The average diffusion coefficient (ADC on Figure 2.10e) shows the areas of high diffusion as hyper-intense. It is considered as a surrogate for cellular density: high ADC values (hyper-intense) correspond to low cellular density. The fractional anisotropy (FA on Figure 2.10f) reveals area of high anisotropy as hyper-intense. It is often anti-correlated to the ADC: high ADC values result in low FA values. The DTI information also gives information about the direction of the white matter fiber tracts. On Figure 2.13, one can see the FA maps on the three different orientation color coded with the orientation of the

principal component of the diffusion tensor.

Finally, advanced imaging techniques can also be used such as perfusion images which reveal cerebral blood volume maps (CBV on Figure 2.10g), Positron Emission Tomography (PET) images which shows metabolic information about the tumor, or MR spectroscopy which reveals the coarse density of different metabolites.

2.4 Radiotherapy Planning

Radiotherapy is a milestone of glioblastoma management. It was shown that concurrent radiation and chemotherapy significantly improved median survival [Mirimanoff et al., 2006]. As mentioned in Section 2.2, the usual standard of care for glioblastoma is photon external beam radiotherapy. We describe in more detail how MR images are used to plan the dose distribution that is delivered to the patient. Even though the practice vary among centers, we base our presentation on [Mason et al., 2007] which is a consensus of the guidelines provided by the European Organization for Research and Treatment of Cancer (EORTC) and the Radiation Therapy Oncology Group (RTOG). We can note that, among other things, how the visible T2-FLAIR abnormality should be taken into account, or how the infiltration margins should be designed, is left at the discretion of the clinician.

The radiotherapy plan is based on the gross tumor volume (GTV) and the clinical target volume (CTV). The GTV can be defined as the union of the abnormality seen on the T1Gd MRI (necrotic core plus proliferative rim on Figure 2.14a) and (potentially) the abnormality seen on the T2 FLAIR MRI (edema on Figure 2.14b). The CTV is a 1-3 cm isotropic expansion of the GTV, trimmed by the clinician to take into account the natural boundary of the tumor progression (ventricles, falx cerebri, ...). It is advised to deliver 60 Gy in 2-Gy fractions every week day during 6 weeks. Alternative plans can define the GTV based on the T1Gd abnormality only, or target a boost volume based on the T1Gd with 60 Gy, while the T2 FLAIR abnormality plus a margin will be targeted with 46 Gy.

The radiotherapy plan is computed on the CT scan (Figure 2.14c) acquired after surgery. Indeed, the Hounsfield unit can be related to the radiation absorption capacity of the tissues. Once the CTV has been defined, the delivered dose is optimized using a certain number of beam angles (often 9) in order to target the tumor while sparing the critical structures of the brain: brainstem, chiasm, eyes, optic nerves (Figure 2.14d). Other organs at risk can be defined depending on the location of the tumor, such as the cochlea. The output of this optimization is the dose delivered at each beam angle (fluence map) as well as the resulting dose distribution that will be delivered to the patient (Figure 2.14e).

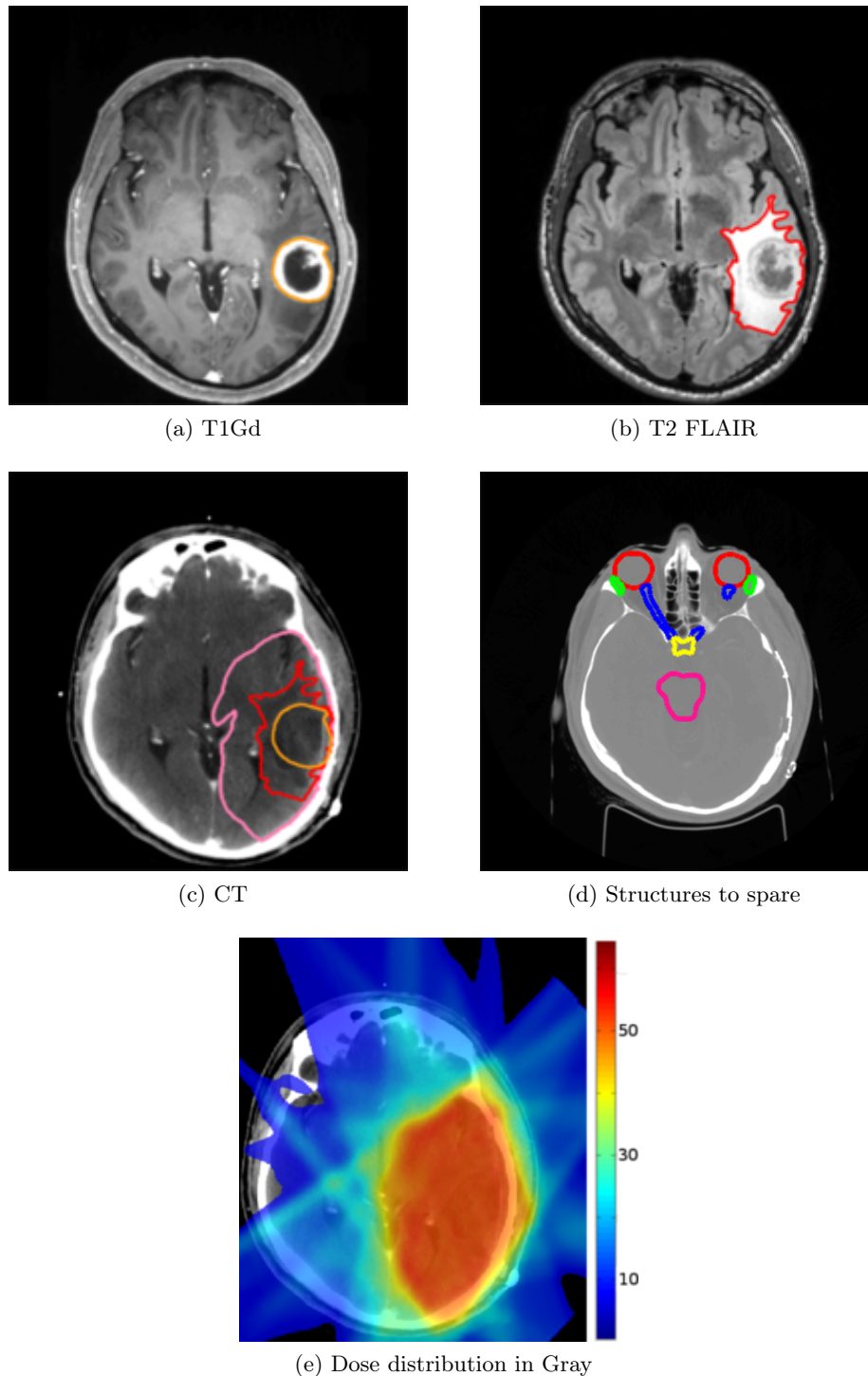


Figure 2.14: The pre-operative T1Gd (2.14a) and T2 FLAIR (2.14b) are used to define the GTV. The CTV (2.14c) and the resulting dose distribution (in Gray) (2.14e) are defined on the CT image. (2.14d) Important structures that the radiation should spare outlined on a CT slice: eyes (red), optic nerves (blue), lacrimal glands (green), chiasm (yellow) and brainstem (pink).

Glioblastoma: Modeling and Personalization

Contents

3.1 Tumor Growth Models - State-of-the-Art	17
3.1.1 Reaction-Diffusion Models	18
3.1.2 Effect of Therapy	19
3.1.3 Reaction-Diffusion Equation	19
3.1.4 Multi-Compartment Models	22
3.2 Personalization - State-of-the-Art	26
3.2.1 Anatomical Personalization	26
3.2.2 Inverse Problem	27

3.1 Tumor Growth Models - State-of-the-Art

Clinical studies, petri dish experiments, describing complex phenomena with equations, implementing mathematical models... The area of research dedicated to the modeling of tumor growth is vast! In this part, we focus on the long lasting work of describing the complex behavior of brain tumors using mathematical formulation: the so-called mathematical modeling of brain tumor growth. The variety of models which have been developed can be classified into three main categories:

- **Microscopic** models describe the evolution of individual cells based on division and invasion rules [Kansal et al., 2000].
- **Homogeneous Macroscopic** models describe the temporal evolution of a scalar associated with the tumor progression using a single or coupled ordinary differential equations. Models usually focus on describing the evolution of the volume or the mass of the tumor [Ribba et al., 2012].
- **Spatial Macroscopic** models describe the spatio-temporal evolution of a tumor cell density in the domain of interest, based on a single or coupled partial differential equations [Swanson et al., 2000].

The variety of tumor growth models have been extensively described in different books [Deisboeck and Stamatakos, 2010, Cristini and Lowengrub, 2010] or review papers [Angelini et al., 2007, Menze et al., 2011a]. The rest of this section will focus on describing the state-of-the-art for macroscopic models based on reaction-diffusion equations. The interesting features of the model will be described, as well as an example of a complex multi-compartment model involving coupled partial differential equations.

3.1.1 Reaction-Diffusion Models

Spatial macroscopic models rely on single or coupled partial differential equation to describe the proliferation and invasion of the tumor cell density in the brain domain. The vast majority of these models are based on the reaction-diffusion equation,

$$\frac{\partial u}{\partial t} = \underbrace{\nabla(D \cdot \nabla u)}_{\text{Diffusion}} + \underbrace{f(u)}_{\text{Reaction}} \quad (3.1)$$

$$D \nabla u \cdot \vec{n}_{\partial\Omega} = 0 \quad (3.2)$$

Equation (3.1) describes the spatio-temporal evolution of the tumor cell density u , which infiltrates neighboring tissues with a diffusion tensor D , and proliferates according to the law defined with $f(\cdot)$. Equation (3.2) enforces Neumann boundary conditions on the brain domain Ω .

In 1989, Murray *et al.* [Murray, 2002] pioneered on the use of mathematics applied to brain tumor growth, using the reaction-diffusion equation with an exponential growth. Assuming an isotropic diffusion in an infinite domain, he relates the velocity v of the tumor growth to the proliferation rate ρ and the diffusion coefficient D , $v = 2\sqrt{\rho D}$. This work has lead the way to numerous other studies [Tracqui et al., 1995, Swanson et al., 2002, Chaplain, 1996].

Improving the computational efficiency of tumor growth models has been the topic of several studies. In 2010, Konukoglu *et al.* [Konukoglu et al., 2010b] introduced an approximation of the asymptotic solution of the reaction-diffusion equation based on an Eikonal equation, which can be solved with a Fast Marching algorithm, resulting in drastically reduced computation times. In 2012, Mosayebi *et al.* [Mosayebi et al., 2012] introduced a similar method to compute the tumor invasion in the brain parenchyma based on a geodesic distance computed from DTI information.

The mass effect applied by the tumor to the surrounding tissues has been modeled in 2005 by Clatz *et al.* [Clatz et al., 2005]. They coupled the reaction-diffusion equation with a mechanical model, to take into account the mass effect, i.e. the displacement of adjacent brain tissue due to the growing tumor. They relate the diffusion tensor D to the Diffusion Tensor Images (DTI), thus forcing the tumor cells to preferably follow the white matter fiber tracts, much like the work of Jbabdi *et al.* [Jbabdi et al., 2005]. In 2008, Hogeia *et al.* [Hogeia et al., 2008] proposed another

approach to include mass effect, using a reaction-diffusion-advection model coupled with a Eulerian mechanical framework.

Finally, research efforts recently targeted the development of more complex models. In 2011, Swanson *et al.* [Swanson *et al.*, 2011] developed a model dividing the tumor cells into sub-categories: the proliferative, the invasive and the hypoxic cells. This type of complex models has been further developed by Saut *et al.* [Saut *et al.*, 2014] in 2014, in which they developed a coupled PDE-based model to simulate the growth of high grade gliomas seeded in real images. Finally, the models were extended to take into account the apparition of edema during the growth [Hawkins-Daarud *et al.*, 2013, Badoual *et al.*, 2014].

3.1.2 Effect of Therapy

Using the reaction-diffusion model, the effect of therapy can be included using an additional term,

$$\frac{\partial u}{\partial t} = \underbrace{\nabla(D \cdot \nabla u)}_{\text{Diffusion}} + \underbrace{f(u)}_{\text{Reaction}} - \underbrace{g(u)}_{\text{Therapy}} \quad (3.3)$$

where $g(u)$ is a death term describing the death of tumor cells due to the therapy.

This type of models have been used by Tracqui *et al.* to model the effect of chemotherapy [Tracqui *et al.*, 1995]. It has also been used to model and optimize the radiation dose delivered to the patient [Rockne *et al.*, 2009, Corwin *et al.*, 2013, Unkelbach *et al.*, 2014b, Unkelbach *et al.*, 2014a]. The effect of resection has been studied using the reaction-diffusion model by removing tumor cells from the resected area [Swanson *et al.*, 2008, Stretton *et al.*, 2012]. The impact of anti-angiogenic therapy has been modeled using complex multi-compartment models [Swanson *et al.*, 2011, Saut *et al.*, 2014, Scribner *et al.*, 2014]. More recently, [Raman *et al.*, 2016] studied the impact of different therapies targeting angiogenesis, tumor replication rates, or motility on so called "computational trials" based on a complex model of brain tumor growth.

3.1.3 Reaction-Diffusion Equation

In this section, we describe in more details the interesting features of the reaction-diffusion equation for the modeling of brain tumor growth. We consider the equation with a logistic growth term with a net proliferation rate ρ , and Neumann boundary conditions on the brain domain Ω ,

$$\frac{\partial u}{\partial t} = \underbrace{\nabla(D \cdot \nabla u)}_{\text{Diffusion}} + \underbrace{\rho u(1 - u)}_{\text{Logistic Proliferation}} \quad (3.4)$$

$$D \nabla u \cdot \vec{n}_{\partial\Omega} = 0 \quad (3.5)$$

Because of the logistic reaction term, equation (3.4) does not have a closed form solution. However, in an infinite domain, with constant proliferation rate and

diffusion coefficient, equation (3.5) admits solutions which asymptotically behave like traveling waves with speed $v = 2\sqrt{\rho D}$ [Konukoglu et al., 2010b]. This solution has the asymptotic form $u(x, t) = u(x - vt) = u(\zeta)$. Plugging it into equation (3.4), we get the ordinary differential equation

$$\mathbf{n}' D \mathbf{n} \frac{d^2 u}{d\zeta^2} + v \frac{du}{d\zeta} + \rho u(1 - u) = 0 \quad (3.6)$$

where \mathbf{n} is the direction of motion in the infinite domain. Moreover, linearizing equation (3.6) for small $u \ll 1$, meaning that $u(1 - u) \sim u$, we get the second order linear equation

$$\mathbf{n}' D \mathbf{n} \frac{d^2 u}{d\zeta^2} + v \frac{du}{d\zeta} + \rho u = 0 \quad (3.7)$$

which admits solutions of the form $u(\zeta) = (A\zeta + B) \exp(-x/\lambda)$ with A, B two constants, and $\lambda = \sqrt{D/\rho}$. This equation shows that the parameter λ is of particular importance: it is related to the spatial decay of the tumor cell density, and it is referred to as the invisibility index [Corwin et al., 2013].

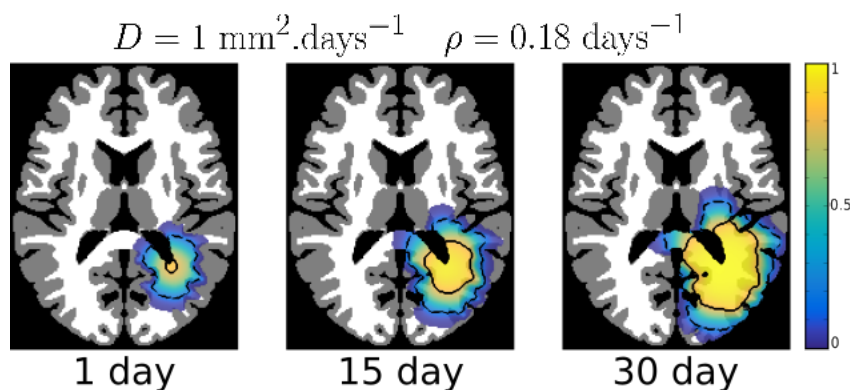


Figure 3.1: 3D simulation of a tumor growth using the reaction-diffusion model with logistic growth in the MNI brain atlas. The tumor cell density is overlaid on the atlas with a segmentation of the white matter (white) and gray matter (gray).

Figure 3.2 presents different solutions of the 1D reaction-diffusion model with different invisibility indexes $\lambda = \sqrt{D/\rho}$ and same speed $v = 2\sqrt{D\rho}$. The slope of the propagating front is correlated with the invisibility index: the greater the invisibility index, the lower the slope, which also models a greater infiltration of the tumor in the neighboring tissues. Figure 3.3 presents different solutions with different speeds and same invisibility index. We show on Figure 3.1 the 3D evolution of a tumor on a brain atlas. The diffusion is lower in the white matter than in the gray matter. We see that this model automatically takes into account the boundaries of the tumor progression (ventricles, falx cerebri), and the privileged pathways of the tumor progression (falx cerebri). Finally, note that the solution of the reaction-diffusion equation provides a tumor cell density over the whole domain. Clinically,

we observe abnormalities on acquired MRIs. A usual assumption is to relate the visible abnormalities to threshold of tumor cell density (Figure 3.4). As such, the T2-FLAIR abnormality which is larger than the T1Gd abnormality is often related to a threshold τ_2 larger than the threshold τ_1 used for the T1Gd abnormality.

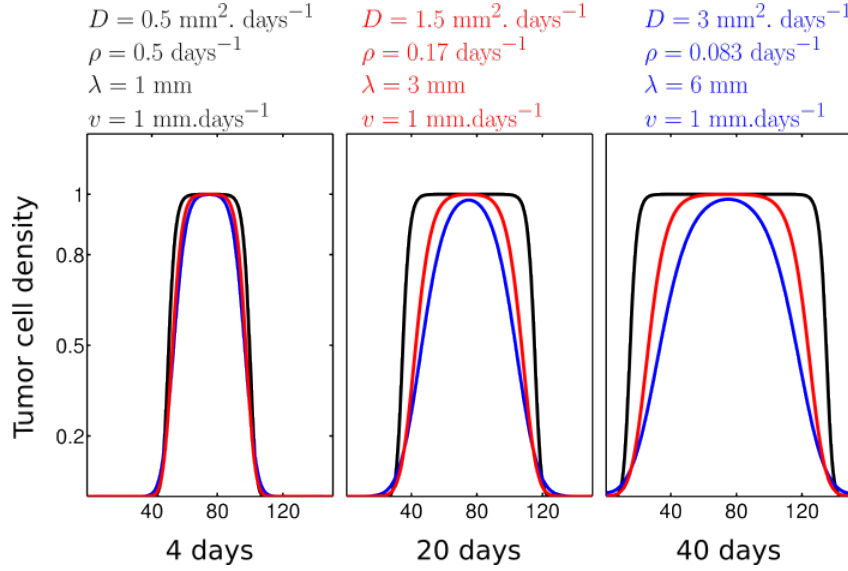


Figure 3.2: 1D simulations of the reaction-diffusion model with a logistic growth. The simulations present different invisibility indexes $\lambda = \sqrt{D/\rho}$ and same speed $v = 2\sqrt{D\rho}$.

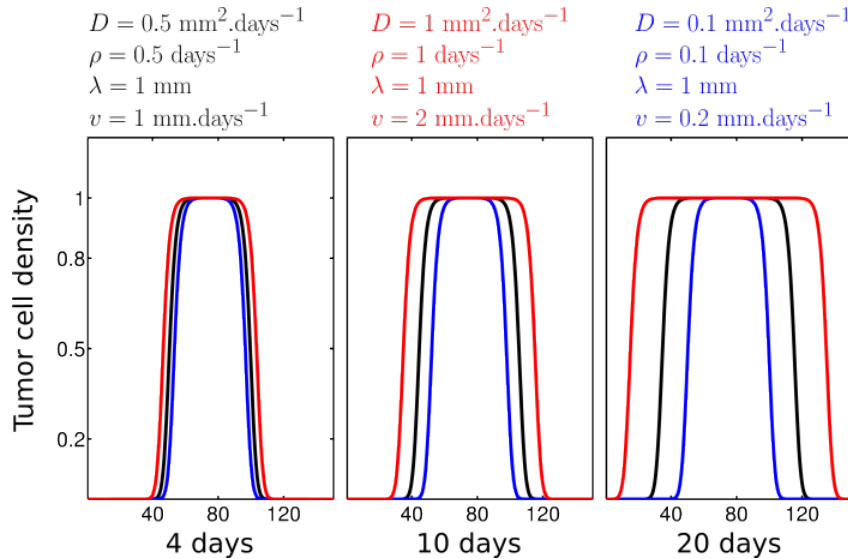


Figure 3.3: 1D simulations of the reaction-diffusion model with a logistic growth. The simulations present different speeds $v = 2\sqrt{D\rho}$ and same invisibility index $\lambda = \sqrt{D/\rho}$.

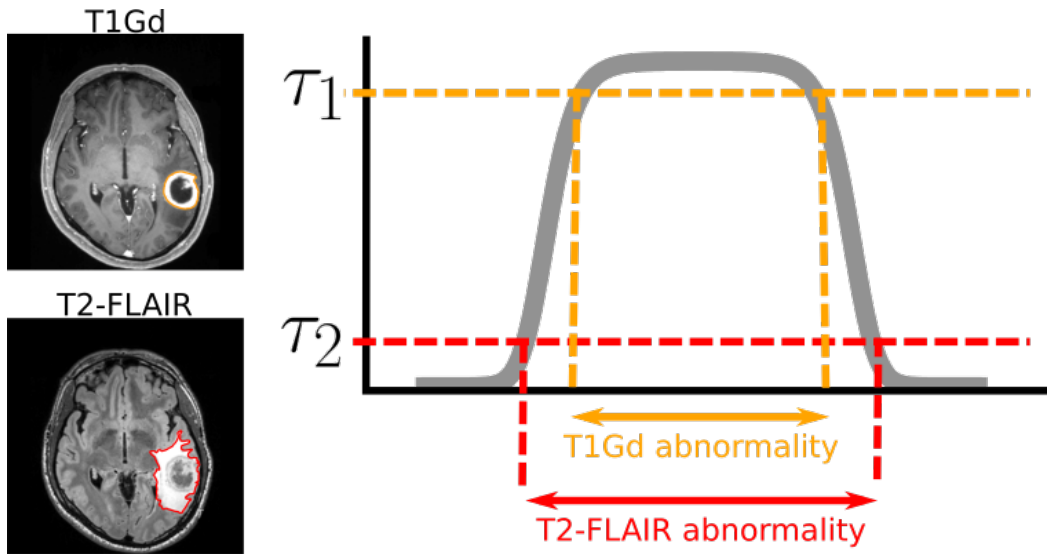


Figure 3.4: Graphic explaining the usual hypothesis which relates a virtual tumor cell density (thick gray line) to the abnormalities observed on the T1Gd and T2-FLAIR abnormalities.

3.1.4 Multi-Compartment Models

We provide in this section an example of a complex multi-compartment tumor growth model based on coupled reaction-diffusion equations. It is loosely based on [Swanson et al., 2011, Saut et al., 2014]. The heterogeneous evolution of glioblastoma growth is modeled using different types of cells:

- **Proliferative cells** abnormally divide in the brain with a proliferation rate ρ , and diffuse very slowly with a diffusion tensor D_P .
- **Quiescent cells** diffuse more rapidly in the brain with a diffusion coefficient D_Q .
- **Necrotic cells** result from the death of proliferative and quiescent cells. They neither diffuse nor proliferate.

This behavior is following the go-or-grow hypothesis: tumor cells either proliferate or diffuse depending on local environmental factors. In this case, the transition between proliferative, quiescent, and necrotic cells is governed by the local vasculature, which is modeled with a nutrient concentration. The appearance of nutrients is triggered by the proliferative cells: this models the creation of new blood vessels by the tumor called the angiogenesis. Nutrients disappear in the necrotic core. The equations of the model are presented on Table 3.1. One can note that the diffusion of the proliferative and quiescent cells is weighted by the complementary of the total amount of cells. This is to avoid diffusion of a specific type of cell in a region of the brain already saturated with another type of cells. The transitions from one type

of cell to the other is governed by a parameter $\lambda_{* \rightarrow *}$ which is proportional to the local nutrient concentration V . To model the lesser infiltration in the gray matter compared to the white matter, the diffusion of tumor cells is set 100 times lower in gray matter. This model was implemented using an implicit Crank-Nicolson scheme described in Appendix A. A simulation using this growth model is shown on Figures 3.5, 3.6, 3.7. The parameters used for this simulation are on Table 3.2. One can note the appearance of a proliferative rim, along with an increase concentration of nutrients which models the neo-vasculature created by the tumor during the angiogenic phase. At the later stage of the growth, a necrotic core appears at the center of the tumor.

Most of the complex models found in the literature are variations of the presented model. Some put more emphasis on the creation of the neo-vasculature by describing the signaling pathways involved in this process [Billy, 2009], some models refine the displacement of tumor cells using advection terms [Saut et al., 2014]. These models present a large number of parameters - 9 in the presented case - which make their study difficult. Moreover, this model requires the initialization of each type of cells and environmental factors, which is complicated and has a direct impact on the simulation. However, there is hope that this type of model can be better suited to take into account the information coming from more recent MRI modalities such as perfusion images, PET images, spectroscopic MRI,...

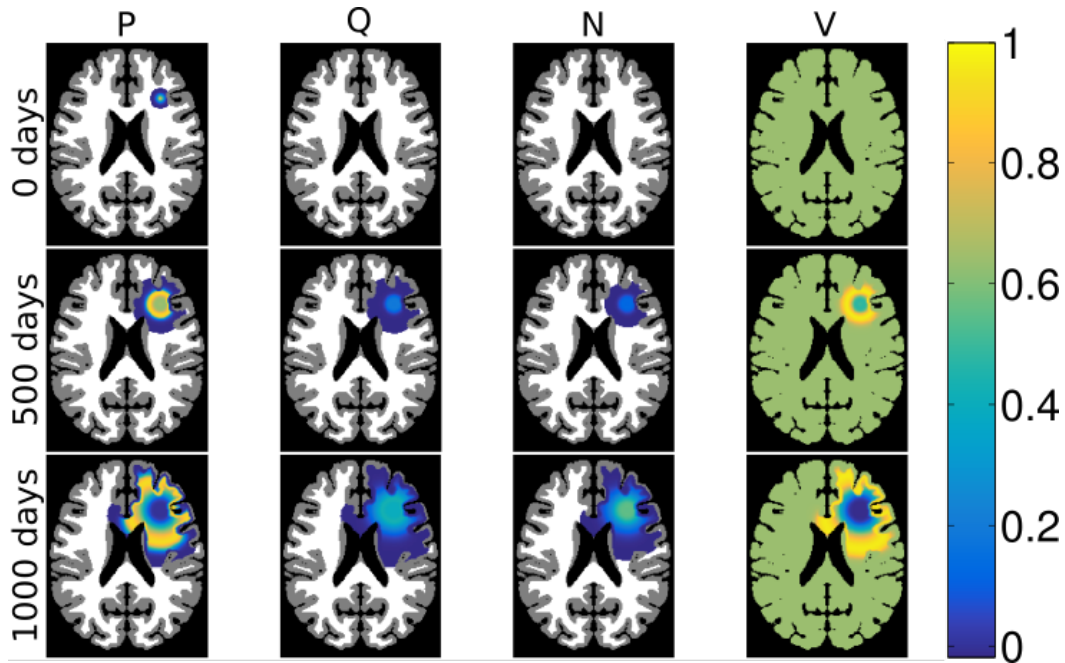


Figure 3.5: Axial slice for the multi-compartment model simulation

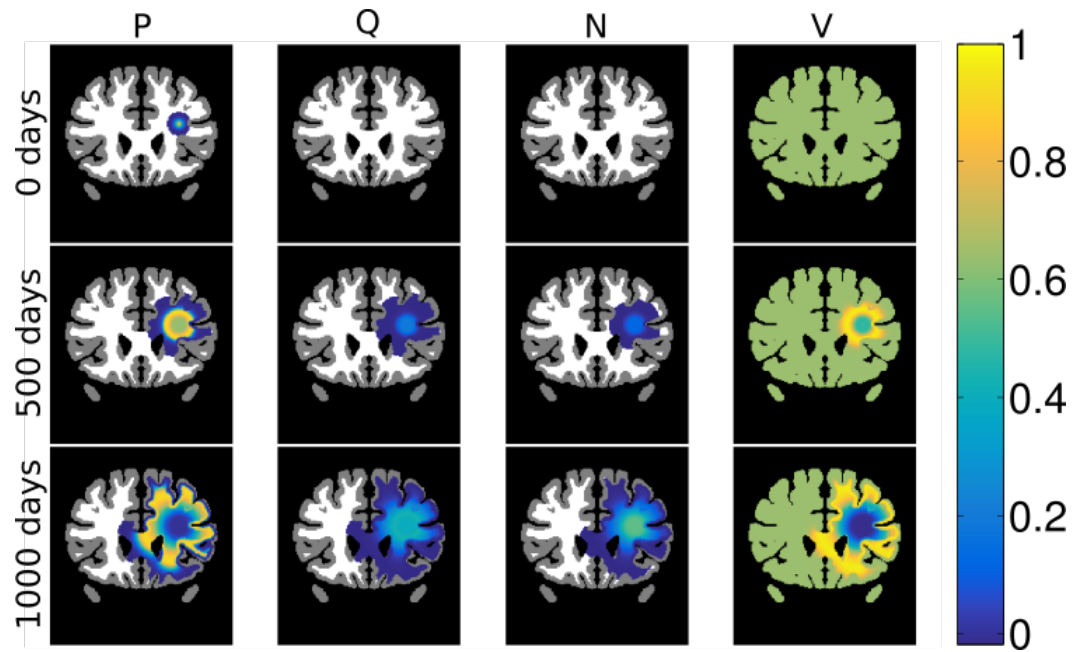


Figure 3.6: Coronal slice for the multi-compartment model simulation

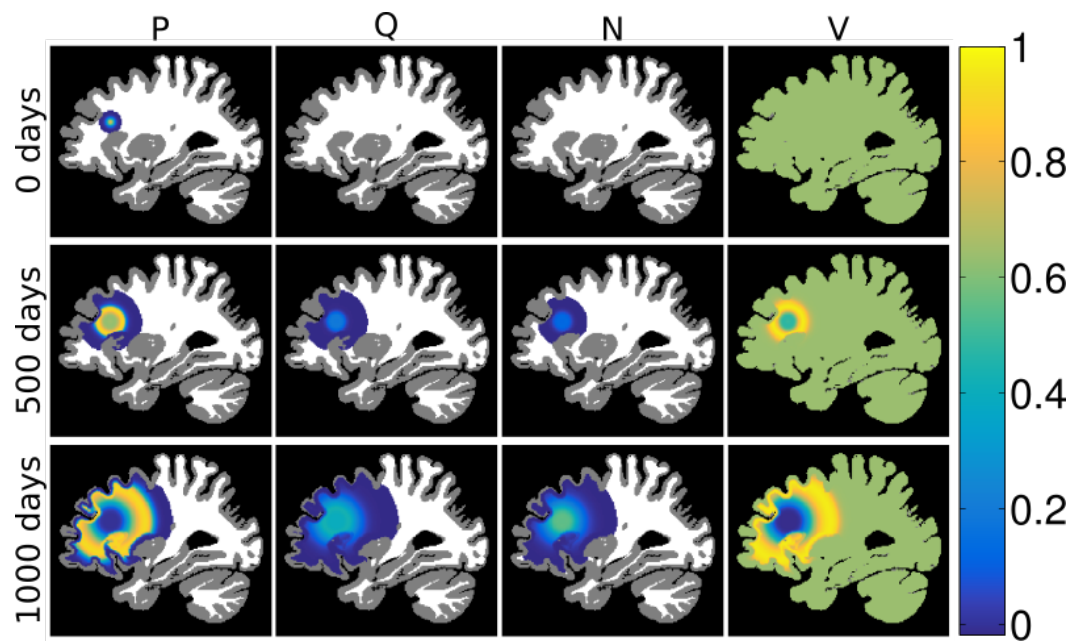


Figure 3.7: Sagittal slice for the multi-compartment model simulation

Cells Equations	
$\frac{\partial P}{\partial t}$	$= \underbrace{\nabla \cdot (D_P (1 - T) \nabla P)}_{\text{Diffusion}} + \underbrace{\rho P (1 - T)}_{\text{Proliferation}}$ $- \underbrace{\lambda_{P \rightarrow Q} P - \lambda_{P \rightarrow N} P + \lambda_{Q \rightarrow P} Q}_{\text{Transitions}}$
$\frac{\partial Q}{\partial t}$	$= \underbrace{\nabla \cdot (D_Q (1 - T) \nabla Q)}_{\text{Diffusion}} - \underbrace{\lambda_{Q \rightarrow P} Q - \lambda_{Q \rightarrow N} Q + \lambda_{P \rightarrow Q} P}_{\text{Transitions}}$
$\frac{\partial N}{\partial t}$	$= \underbrace{\lambda_{P \rightarrow N} P + \lambda_{Q \rightarrow N} Q}_{\text{Transitions}}$
where	$T = P + Q + N$ is the total amount of tumor cells.
Environmental Equations	
$\frac{\partial V}{\partial t}$	$= \underbrace{\alpha P (1 - V)}_{\text{Angiogenesis}} - \underbrace{\beta N V}_{\text{Degradation}}$
Transitions	
$\lambda_{P \rightarrow Q}$	$= \gamma_{P \rightarrow Q} (1 - V)$
$\lambda_{P \rightarrow N}$	$= \gamma_{P \rightarrow N} (1 - V)$
$\lambda_{Q \rightarrow P}$	$= \gamma_{Q \rightarrow P} V$
$\lambda_{Q \rightarrow N}$	$= \gamma_{Q \rightarrow N} (1 - V)$
where	$\gamma_{A \rightarrow B}$ is the transition factor between cells A and cells B.

Table 3.1: Equations of the complex multi-compartment model of brain tumor growth.

ρ (days ⁻¹)	0.03
D_P (mm ² .days ⁻¹)	0.001
D_Q (mm ² .days ⁻¹)	0.1
$\gamma_{P \rightarrow Q}$ (days ⁻¹)	0.005
$\gamma_{P \rightarrow N}$ (days ⁻¹)	0.003
$\gamma_{Q \rightarrow P}$ (days ⁻¹)	0.001
$\gamma_{Q \rightarrow N}$ (days ⁻¹)	0.001
α (days ⁻¹)	2
β (days ⁻¹)	9

Table 3.2: Parameters used for the simulation of the multi-compartment model.

3.2 Personalization - State-of-the-Art

The personalization of a tumor growth model is the problem of fitting a specific model to the data of a specific individual. In computational biology, the personalization can be decomposed into two main parts. The first one is the anatomical personalization: the model should be computed in the unique anatomy of the considered subject. The second one is the inverse problem: the free parameters of the mathematical model should be set so as to reflect the behavior of the observed pathology.

3.2.1 Anatomical Personalization

In MRI based models such as the ones considered in this thesis, the anatomical personalization corresponds mainly to the processing of the images in order to extract the information relevant to the modeling. For brain tumor growth models, we are interested in

- The segmentation of the white and gray matter: the tumor cells diffuse more rapidly in the white matter, and this can be taken into account by setting a larger diffusion coefficient in the white matter than in the gray matter.
- The segmentation of cerebrospinal fluid (CSF): glioma cells do not invade the CSF. This has to be taken into account by the accurate segmentation of the ventricles and the falx cerebri.
- The segmentation of the structures of the tumor such as the necrotic core, the proliferative rim, and the edema. This information is crucial to compare the model with the MRIs.

The literature on segmentation of medical images is extremely vast, and will not be reviewed here. In this thesis, we mainly relied on the state-of-the-art segmentation software FSL [Zhang et al., 2001] which allows to: extract the skull from the images, segment the white matter, gray matter and CSF. The method is based on an

expectation-maximization algorithm with a hidden markov random field to regulate spatial smoothness. For the segmentation of the structures of the tumor, we relied on manual clinician segmentations. Note that there is a growing community interested in automatically segmenting the tumor; see [Menze et al., 2015] for a review of the state-of-the-art. Figure 3.8 shows the segmentation of the structures of interest for a specific patient.

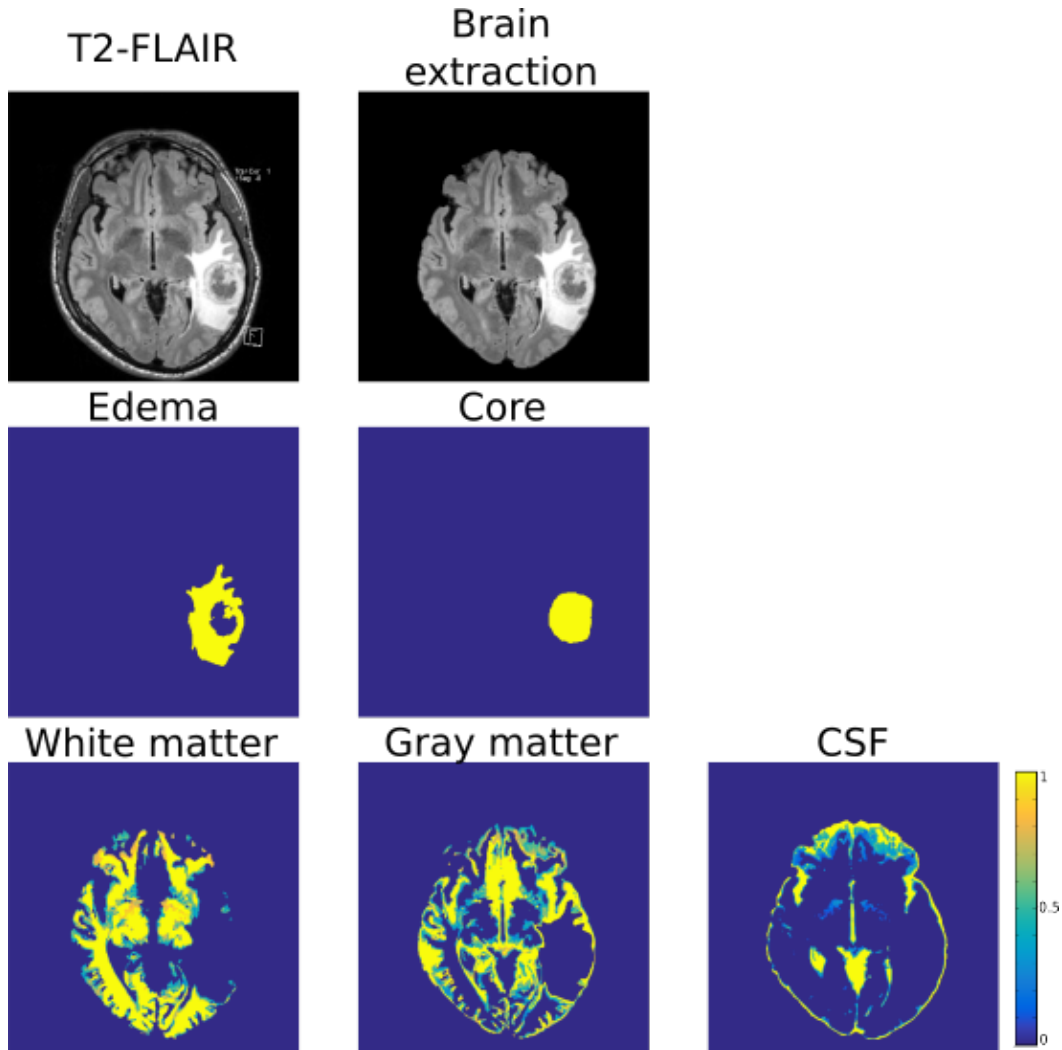


Figure 3.8: From top to bottom and left to right: T2-FLAIR MRI, extraction of the brain, clinician segmentations of the edema and core of the tumor, probabilistic segmentation of the white matter, gray matter and CSF.

3.2.2 Inverse Problem

Finding the best parameters to model the dynamics of a specific tumor is called the inverse problem. In the case of the reaction-diffusion model with logistic proliferation, it corresponds to finding the diffusion parameter D , proliferation parameter

ρ , and initialization, which best fit the data of a given patient. In the specific case of glioma growth, most methods rely on comparing the model output with the abnormalities visible on Magnetic Resonance Images (MRIs) at two different time points.

A common approach to personalize reaction-diffusion equations is based on the observation that they admit wave-like solutions whose parameters can be related to the volume of the abnormalities observed on MRIs. In 2007, Harpold *et al.* [Harpold *et al.*, 2007] described the personalization of a glioma growth model using the reaction-diffusion equation with an exponential growth.

Another popular approach relies on solving the inverse problem using an optimization strategy. Hoge *et al.* [Hoge *et al.*, 2008] formulated a PDE-constrained optimization problem to estimate the parameters of the model based on image registration. Konukoglu *et al.* [Konukoglu *et al.*, 2010b] used the derivative-free optimization algorithm BOBYQA (for bounded optimization by quadratic approximation) [Powell, 2009] to minimize the distance between the tumor segmentations observed on the MRI, and the output of the model.

Finally, probabilistic approaches recently gained interest to solve complex inverse problems. Menze *et al.* [Menze *et al.*, 2011b] was among the first to propose a Bayesian formulation for brain tumor growth personalization, based on the approximation of the posterior using sparse grids. In 2012, Gooya *et al.* [Gooya *et al.*, 2012] proposed a method for the segmentation and registration of MRIs presenting glioblastoma based on the personalization of a reaction-diffusion-advection model using a single time point acquisition. It is interesting to note that Bayesian formulations have been used for a few years in the field of cardiac modeling [Konukoglu *et al.*, 2011, Neumann *et al.*, 2014]. However, the methods usually rely on approximations of the forward model using reduced order model, such as the polynomial chaos, to make the estimation of the posterior using Markov Chain Monte Carlo (MCMC) computationally tractable.

Multimodal Analysis of Vasogenic Edema in Glioblastoma Patients for Radiotherapy Planning

Contents

4.1	Introduction	31
4.2	Material and Methods	32
4.3	Results	36
4.3.1	Comparison between the Three Experiments	36
4.3.2	Application to radiotherapy	38
4.4	Conclusion	39

Based On: the workshop paper [Lê et al., 2014].

Glioblastoma (GBM) is the most common type of primary brain tumor, which is characterized by an infiltrative growth pattern. In current practice, radiotherapy planning is primarily based upon T2 FLAIR MRI despite its known lack of specificity in the detection of tumor infiltration. While hyperintensity on T2 FLAIR is widely considered to represent infiltrative tumor, it may also be caused by the presence of vasogenic edema (VE), caused by a leakage of fluid into the brain parenchyma. Distinguishing VE from infiltrative tumor could have impact on improving radiotherapy planning. In this chapter we study a data set of 17 GBM patients treated with anti-angiogenic therapy for which a fast decrease of T2 FLAIR hypersignal is observed, which indicates the resolution of VE. We investigate if multimodal MRI acquisitions including diffusion tensor imaging can distinguish between VE and tumor infiltration prior to therapy. Using a random forest classifier, we show that, in this study, morphological information based on the contrast enhanced T1 image explains up to 75% of the extent of VE. The information from different imaging modalities did not significantly improve the classification. We then show that delineating the VE prior to therapy can have substantial impact on radiotherapy target delineation, leading to smaller treatment volumes and reducing potentially harmful radiation dose to normal brain tissue.

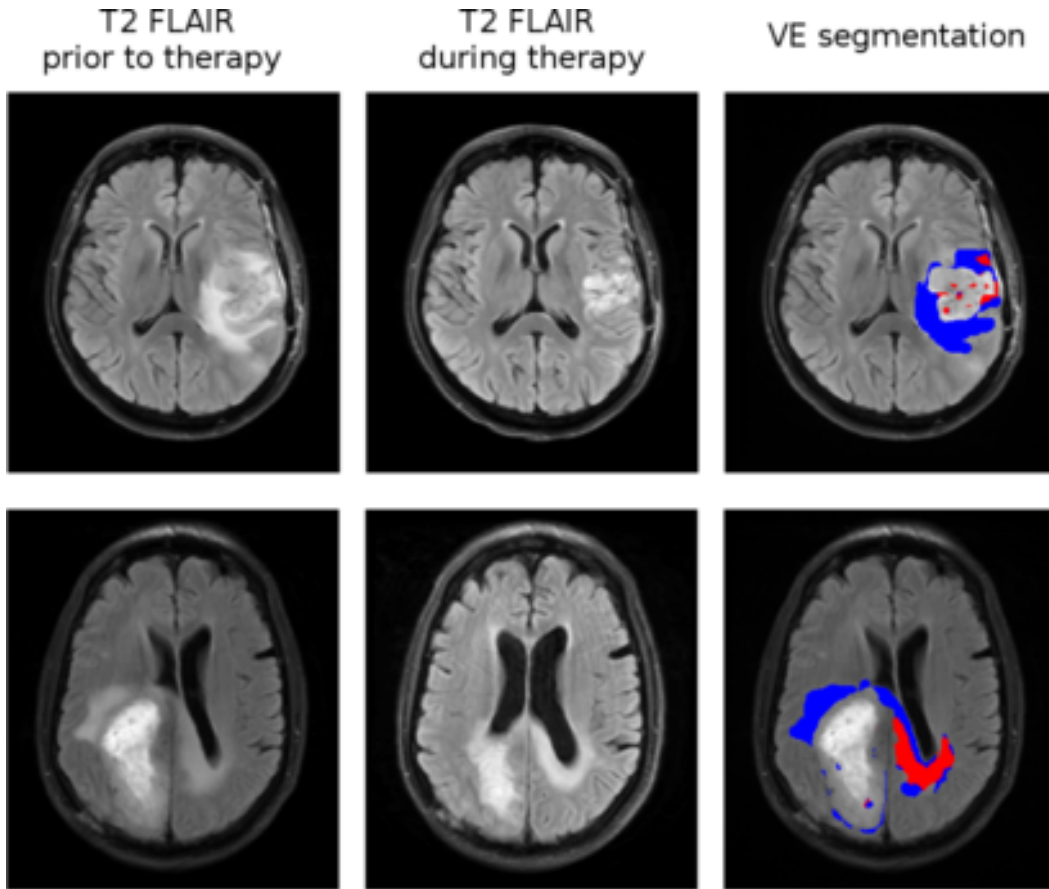


Figure 4.1: Response to anti-angiogenic therapy for two patients. The smallest T2-FLAIR abnormality (middle) can be observed 42 days after the beginning of therapy for the first patient (first row) and 100 days for the second patient (second row). The VE corresponds to the responsive voxels (blue). The non responsive voxels are tumor related (red).

4.1 Introduction

Glioblastoma (GBM) is an infiltrative brain tumor whose cells invade the adjacent brain tissue which is only partially revealed by MRI [Kelly, 1993]. Furthermore, the signal abnormality on T2-FLAIR and contrast enhanced T1 (T1Gd) images is only a surrogate for tumor invaded tissue but not per se indicative of the presence of tumor cells. Indeed, the T2-FLAIR abnormality is a signal resulting from the combination of the bulk of the tumor, tumor cell infiltration, and vasogenic edema (VE) [Coons, 1999]. VE represents an increase in water content in the brain parenchyma, which is a consequence of the disruption of the blood brain barrier. Despite its unspecific nature, for lack of a more accurate tumor infiltration surrogate, clinicians use the T2-FLAIR abnormality to define the treatment volume for radiotherapy. Therefore, discarding VE from the T2-FLAIR abnormality could possibly result in a better

surrogate for GBM cell infiltration and, as such, provide a better guide for radiotherapy planning by eliminating targeting of radiation to neighboring regions of normal uninvolved brain and other healthy tissues.

There has been a body of work on characterizing peritumoral edema through different imaging modalities including MRI and PET. For example, it has been investigated whether measures derived from diffusion tensor imaging (DTI) can distinguish between meningiomas and gliomas. The edema surrounding meningiomas is considered to be purely vasogenic while the edema surrounding gliomas is partly infiltrative tumor. It has been suggested that the relationship between the mean diffusivity (MD) and the fractional anisotropy (FA) can help distinguish between the two [Lu et al., 2004]. Axial and radial diffusivity (AD and RD respectively) were subsequently shown to be alternative markers [Min et al., 2013]. At the same time, PET imaging using FDG or amino acid tracers proved to be quite successful in discriminating between meningiomas and gliomas [Kinoshita et al., 2012]. In such diagnostic applications, the images as a whole are used for tumor classification or staging. However, for radiotherapy planning, the difficulty consists in locally delineating VE from tumor infiltration. To our knowledge, this is the first reported study with this aim.

A fundamental problem in this context is the definition of the VE ground truth. To this end, we use the response of the edema to anti-angiogenic therapy in a dataset containing 17 patients. The treatment is assumed to normalize blood vessels in the tumor, thereby restoring the blood brain barrier. As a consequence, this leads to the resolution of VE within a few weeks of treatment. Residual hyperintensity on T2-FLAIR is assumed to represent infiltrative tumor. The alternative to reliably define the ground truth would be to perform several biopsies, which would be invasive and impractical.

Based on multimodal imaging and the delineation of VE, feature selection and classification are performed to locally distinguish between VE and infiltrative tumor prior to therapy. More precisely, we consider the following features: standard MRI, morphological information (distance from the abnormalities), and DTI based information. We show that, within the approach taken in this work, morphological information is the most important input to define the VE. Surprisingly, DTI based features did not refine the classification. Finally, we show how a segmentation of the VE prior to therapy can change the radiotherapy plan: being able to detect VE prior to therapy leads to smaller treatment volumes and reduce potentially harmful radiation dose to normal brain tissue.

4.2 Material and Methods

Database. 40 patients were treated with the anti-angiogenic drug cediranib. Out of those 40, 17 were considered as responsive patients, i.e. the T2-FLAIR abnormality significantly shrinks during the early course of treatment. The remaining 23 patients were excluded because they appeared to not respond to the therapy. Figure

4.1 shows two responsive patients. The patient in the upper row shows extended edema surrounding the gross tumor which is almost completely resolved within 6 weeks. The patient in the bottom row shows both persistent hyperintensity (in the contralateral hemisphere) and resolved VE anterior to the gross tumor. For each patient, we have access to 5 structural images (T1, T1Gd, T1Gd High Resolution (T1 HR), T2, T2-FLAIR); in addition DTI was available from which we derived 4 images (FA, ADC, axial diffusivity (AD) and radial diffusivity (RD)) (Figure 4.3).

Pre-processing of the data. Each patient went through the following pipeline: bias field correction, rigid registration of the images on the pre-treatment T1Gd MRI, extraction of the brain and segmentation of the white matter, gray matter and cerebrospinal fluid. Structural images were normalized such that each modality has the same manually fixed mean intensity in the white matter tissue across patients.

Definition of the ground truth. For each patient and for each acquisition, the T2-FLAIR and T1Gd abnormalities were manually segmented by clinicians. The imaging time points corresponding to the largest and smallest T2-FLAIR abnormalities were used to define the VE. The T1Gd abnormality was excluded from these volumes. VE was defined as the voxels included in the largest T2-FLAIR abnormality but not in the smallest T2-FLAIR abnormality. Accordingly, the class of non responsive voxels was defined as all voxels that are within the T2-FLAIR abnormality at both time points. (Figure 4.1).

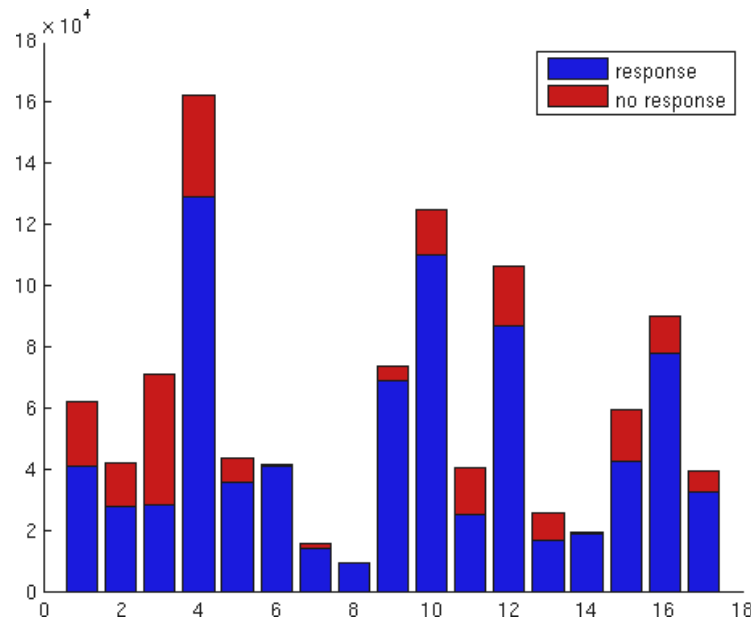


Figure 4.2: The distribution of responsive (blue) and non responsive (red) voxels among the 17 selected patients

Feature Definition. For each voxel, we define 56 features. We use two morphological features which are defined as the logit function of the signed distance from the pre-treatment T2-FLAIR and T1Gd abnormalities (log-odds map) [Pohl et al., 2006]. In addition, we use 5 structural images (T1, T1Gd, T1 HR, T2, T2-FLAIR) and 4 DTI based images (FA, MD, RD, AD). For each of these 9 images, we derive 6 features: the image intensity, two Gaussian convolutions at two different scales as well as the fractional anisotropy, the mean diffusivity and the determinant of the structure tensor of the original image.

Experiments. We want to analyze the performance of a classification algorithm in three different conditions: using all the features, using only morphological information, and using only DTI based information. For these three experiments, a random forest (RF) classifier [Pedregosa et al., 2011] was used for the final classification. The design of the experiments differs in the feature selection prior to training the RF:

Experiment 1. An l_1 -penalized support vector machine (l_1 -SVM) was trained on a small bootstrapped training sample for a repeated number of times using the 56 features. The features that were selected by the l_1 -SVM at every iteration were used for the classification. The regularization term of the l_1 -SVM was set such that 10 features were selected in the end.

Experiment 2. We restricted ourselves to using only the morphological information, i.e. the 2 log-odds based features. In order to compare the results with the first experiment (i.e. consider a set of 10 features for the subsequent random forest classifier), 8 among the 54 remaining features were randomly selected. Those features were then randomized: for each feature, we randomly permuted the value of this feature among the different samples. This means that those features do not contain any information anymore: the predictive power of the subsequent random forest will be due to the morphological information.

Experiment 3. The 24 different DTI based features were used.

The training data set is imbalanced as 80% of voxels belong to the VE class, while 20% are non responsive (Figure 4.2). We drew an equal number of samples from each class to re-balance the data set for the l_1 -SVM. For the RF, the minority class (non responsive voxels) was oversampled using bootstrap while keeping the dominant class untouched. This ensures that the classification error do not lean toward the minority class [Zhang and Tsai, 2007]. For each experiment, a leave-one-out approach was used by running the experiments 17 times, each time leaving one patient out of the training set.

Radiotherapy planning. We compare the radiotherapy plan based on the initial T2-FLAIR image with the plan that discards VE from the tumor delineation. 9 equally spaced coplanar photon beams were used to compute the plans for intensity modulated radiotherapy (IMRT). Dose calculation was performed with CERR

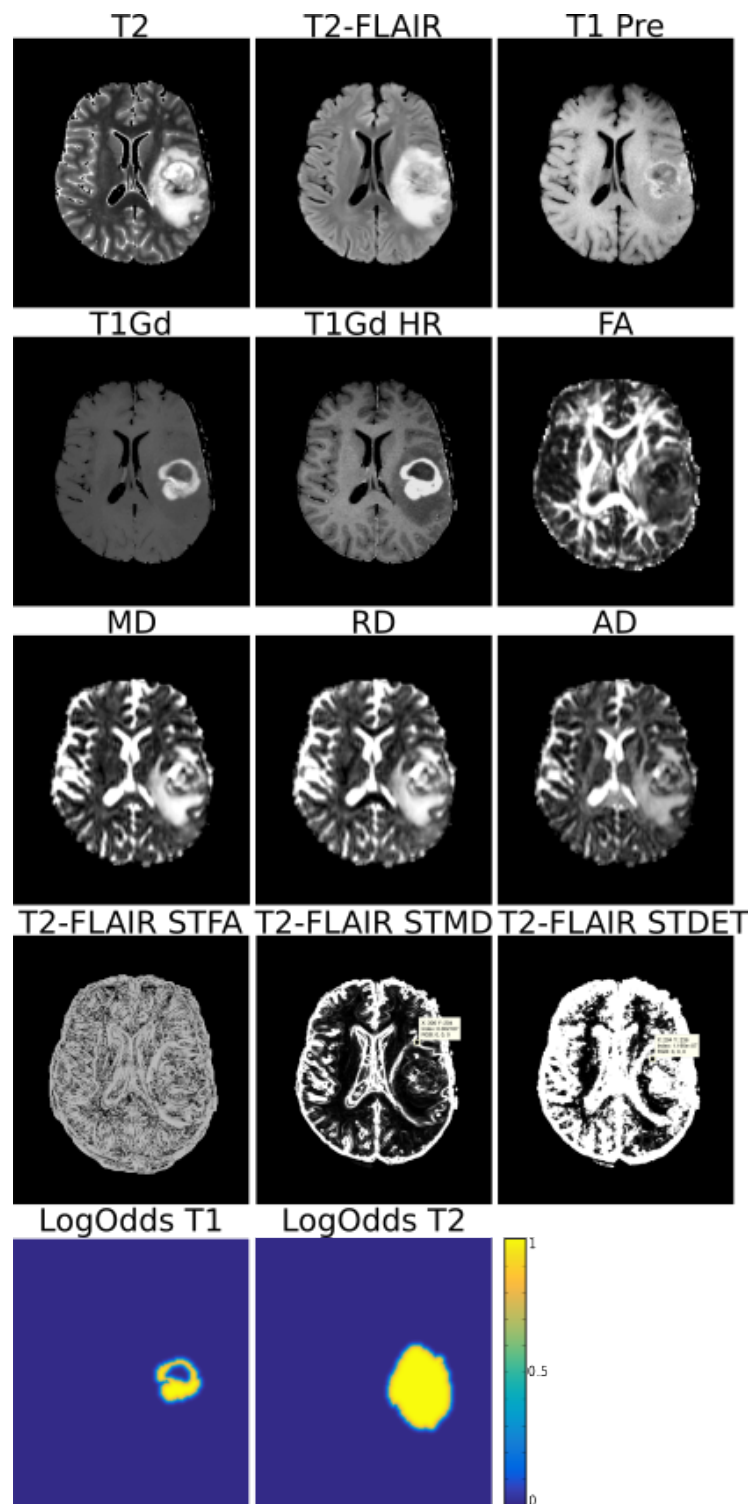


Figure 4.3: Example of some of the features used. From left to right, top to bottom: T2 MRI, T2-FLAIR MRI, T1 MRI, T1 with gadolinium contrast agent MRI, high resolution T1 with gadolinium contrast agent, Fractional Anisotropy, Mean Diffusivity, Radial Diffusivity, Axial Diffusivity, Fractional Anisotropy of the structure tensor of the T2-FLAIR MRI, Mean Diffusivity of the structure tensor of the T2-FLAIR MRI, Determinant of the structure tensor of the T2-FLAIR MRI, LogOdds of the T1Gd abnormality, LogOdds of the T2-FLAIR abnormality.

[Deasy et al., 2003], and an L-BFGS quasi-newton method was used to optimized the IMRT treatment plans [Unkelbach et al., 2014b].

4.3 Results

4.3.1 Comparison between the Three Experiments

ROC curves were computed by changing the voting threshold of the prediction output of the RF. The areas under the curve were then averaged over all the iterations of the leave-one-out process (Figure 4.4). The training set corresponds to 16 patients while the testing set is the left out patient. When considering the training set, the first experiment yields the best results since it involves all features. However, on the testing set, experiment 2 yields comparable results with an AUC of 0.75, compared to an AUC of 0.77 for experiment 1. The third experiment involving only DTI based features yields the worst results with an AUC of 0.68 and 0.54 for the training and testing sets, respectively.

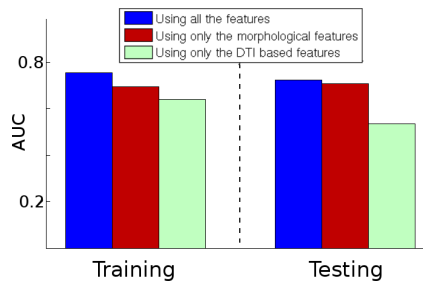


Figure 4.4: Area under the ROC curve for the three different experiments for the training and testing sets.

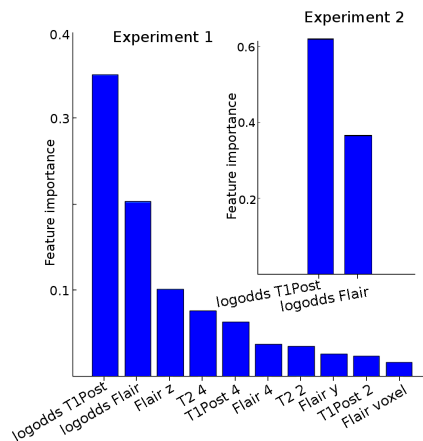


Figure 4.5: Feature importance measured as the mean decrease impurity of the RF for all the features (left) and only the morphological features (right).

The morphological information based on the log-odds features gives results com-

parable to using all 56 features defined via multimodal MRI images. This is supported through Figure 4.5 which shows the feature importance for the RF training as the mean decrease impurity [Breiman et al., 1984] at each node for experiment 1 and 2. It appears that, regardless of using all the features, the log-odds are largely dominant. More specifically, the distance from the T1Gd abnormality seems to be the single best feature to segment the VE.

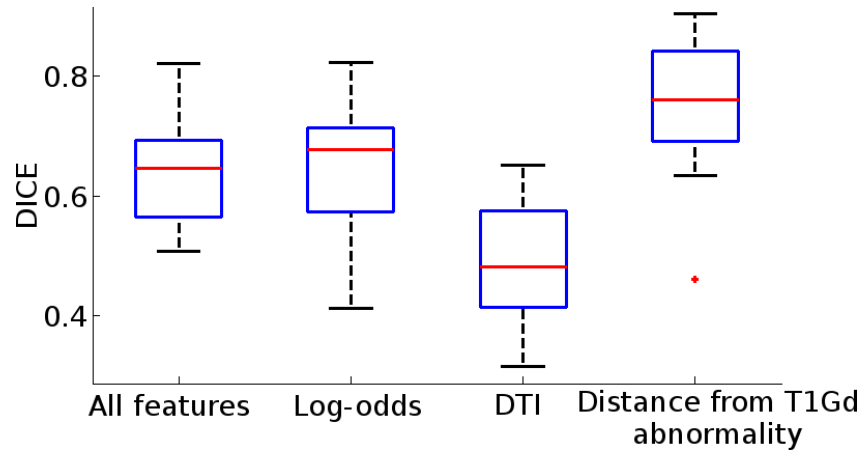


Figure 4.6: Distribution of the DICE coefficient for the four final VE segmentations.

To obtain a final segmentation, the threshold for the RF is selected by imposing a cost of 2 for predicting tumor infiltration as VE and a cost of 1 for predicting VE as tumor infiltration was set. This reflects the idea that the radiotherapy target should be conservative and enclose all the tumor infiltration. DICE coefficient between RF segmentations and ground truth were calculated (Figure 4.6). This confirms the previous findings that DTI alone yields poor results with a mean DICE of 0.48. Using the RF with all features gives similar results to using solely the morphological features (mean DICE of 0.63 and 0.64).

For comparison, we analyzed how well the distance from the T1Gd abnormality alone could be used to delineate the VE. To that end, we computed the median distance that encloses 90% of the persistent T2-FLAIR abnormality, which yields 4.8 mm for this subset of patients. VE was then defined as the voxels in the T2-FLAIR abnormality that are further than 4.8 mm away from the T1Gd abnormality. The mean DICE coefficient for this segmentation is 0.75, i.e. it outperforms the RF (Figure 4.6). Figure 4.7 shows the segmentation of the RF using all the features, and the segmentation based on the distance from the T1Gd abnormality for one of the patients. Using the distance from the T1Gd abnormality gives overall good results. The RF output yields irregular contours and fails to improve on the distance based segmentation. It should be noted that, while the distance from the T1Gd abnormality yields comparatively good results on average, it fails to identify persistent hyperintensity in some patients. For the patient shown in the bottom row of Figure 4.1, the hyperintensity in the contralateral hemisphere is classified as VE by this method.

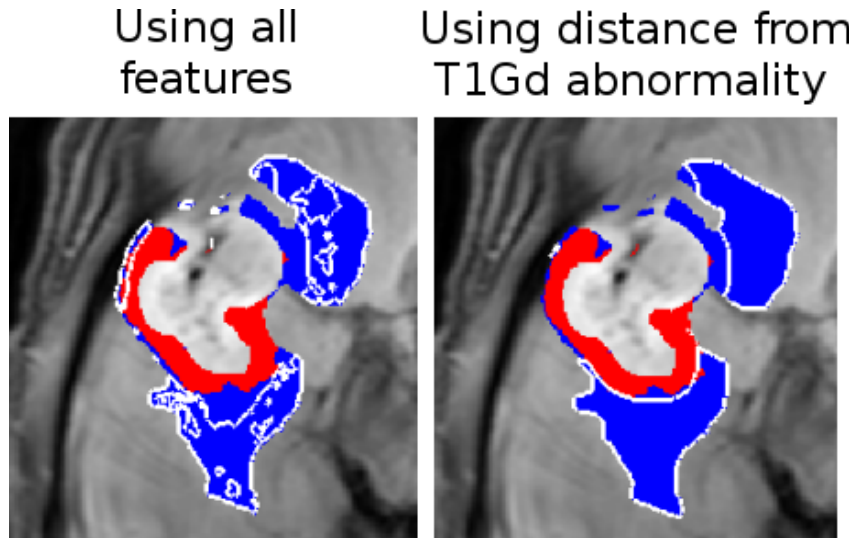


Figure 4.7: Segmentation of VE using the RF with all features (left) and the distance based criteria (right). The ground truth for tumor infiltration is shown in red, VE in blue. The prediction is outlined in white.

One limitation of our work is the inability to decipher whether persistent T2-FLAIR hyperintensity represents persistent disease, or VE without disease that was unresponsive to anti-angiogenic therapy. In our study, these patients were excluded, which introduced a patient selection bias.

4.3.2 Application to radiotherapy

In current clinical practice, the clinical target volume (CTV1) for radiotherapy is often defined as a 2-2.5 cm isotropic expansion of the T2-FLAIR abnormality. Using the above result, we defined an alternative CTV2 based on a 2.48 cm isotropic expansion of the T1Gd abnormality. Such a target would enclose the tumor infiltration with the 4.8 mm margin, to which we add a 2 cm expansion. The CTV2 is then solely based on the delineation of the T1Gd abnormality. IMRT plans based on the two targets have been calculated for the patient in figure 4.8.

The patient shows extensive edema, which extends posteriorly more than anteriorly (4.8, left). This leads to a large CTV1 and a high dose delivered to most of the left parietal lobe (4.8, middle). The residual T2-FLAIR abnormality after resolution of the VE is located more symmetrically around the initial T1Gd abnormality. This leads to a CTV2 that extends less far posteriorly, which translates into a lower dose delivered to posterior region of the parietal lobe. The dose difference plot (4.8, right) shows a dose reduction of more than 30 Gy in this region. In total, the plan based on CTV2 delivers 24% less dose to the brain. Considering the reduction of the T2-FLAIR abnormality after the resolution of VE, the inclusion of almost the entire left parietal lobe in CTV1 does not seem warranted.

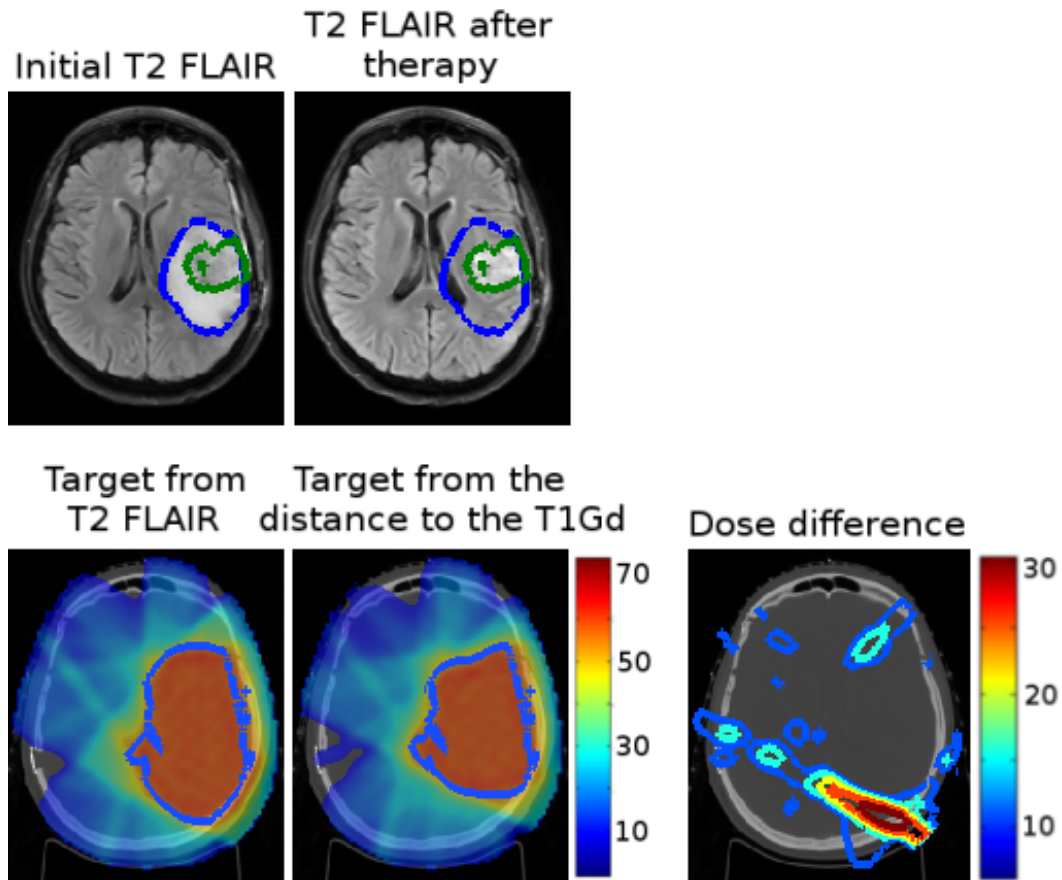


Figure 4.8: Radiotherapy plans for one patient. The initial (blue) and residual (green) T2-FLAIR abnormalities are outlined on the initial T2-FLAIR (first image) and the T2-FLAIR after radiotherapy (second image). The dose distributions (in Gy) based on CTV1 and CTV2 are overlaid on the CT image (third and fourth images). The target is outlined in blue. The dose difference between the two plans is shown on the right.

4.4 Conclusion

Many GBM patients present extensive T2-FLAIR hyperintensity on brain imaging that is known in part to represent peritumoral edema and to less well understood extent, represent infiltrative tumor cells. Excluding VE that does not harbor tumor cells from the radiotherapy target delineation would enable reduction in target volumes and with the potential of exposing less radiation to surrounding normal brain tissue. This could lead to less toxicity and may leave more opportunity for a possible re-irradiation after recurrence. Our dataset of patient treated with anti-angiogenic therapy shows that a substantial part of the T2-FLAIR hyperintensity disappears during the initial weeks of treatment, providing support for the idea of excluding parts of the T2-FLAIR abnormality from the delineation of gross disease.

We investigated if multimodal MR imaging can identify VE prior to radiotherapy. In our approach, the distance from the contrast enhancing tumor is the single best feature to segment the VE, reflecting the observation that for most patients, infiltrative tumor is adjacent to the T1Gd abnormality. Improving on this distance based segmentation is a difficult task. DTI measures and image intensity features did not yield an improvement in conformal tumor target definition. Future improvements may be possible by including MR spectroscopy data and more contextual as well as texture features.

Sampling Image Segmentations for Uncertainty Quantification

Contents

5.1	Introduction	43
5.2	Existing Generative Models of Segmentations	44
5.3	GPSSI	45
5.3.1	Definition	45
5.3.2	Geodesic Distance Map	46
5.3.3	GPSSI	47
5.3.4	Efficient Sampling	48
5.4	Parameter Settings	49
5.5	Segmentation Sampling	51
5.6	GPSSI Extensions	51
5.6.1	Several Neighboring Structures	51
5.6.2	Accounting for Under and Over Segmentation	52
5.6.3	Inclusion or Exclusion of Structures	53
5.6.4	General Covariance Matrix Using Supervoxels	54
5.6.5	Plausibility of the Samples: Evaluation on multiple segmentations	56
5.7	Tumor Delineation Uncertainty in Radiotherapy	58
5.8	Conclusion	60

Based On: the conference paper [Lê et al., 2014] and the journal extension [Lê et al., 2016].

In this chapter, we introduce a method to automatically produce plausible image segmentation samples from a single expert segmentation. A probability distribution of image segmentation boundaries is defined as a Gaussian process, which leads to segmentations which are spatially coherent and consistent with the presence of salient borders in the image. The proposed approach is computationally efficient, and generates samples which are visually plausible. The sample variability is mainly governed by a parameter which may be correlated with a simple Dice's coefficient, or easily set by the user from the definition of probable regions of interest. The method is extended to the case of several neighboring structures, but also to account for under or over segmentation, and the presence of excluded regions. We also detail a method to sample segmentations with more general non-stationary covariance functions which relies on super-voxels. Furthermore, we compare the generated segmentation samples with several manual clinical segmentations of a brain tumor. Finally, we show how this approach can have useful applications in the field of uncertainty quantification, and an illustration is provided in radiotherapy planning, where segmentation sampling is applied to both the clinical target volume and the organs at risk.

5.1 Introduction

Medical image segmentation is a key technology for many medical applications, ranging from computer aided diagnosis to therapy planning and guidance. Due to its ill-posed nature, the quantification of segmentation uncertainty is crucial to assess the overall performance of other applications. In radiotherapy planning for instance, it is important to estimate the impact of uncertainty in the delineation of the gross tumor volume and the organs at risk on the dose delivered to the patient.

A straightforward way to assess this impact is to perform *Image Segmentation Sampling* (ISS), which consists of gathering several plausible segmentations of the same structure, and estimate the variability of the output variables due to the variability of the segmentations. In this chapter, a segmentation is said plausible if it is spatially coherent and consistent with the presence of salient borders in the image. For computer generated segmentations, ISS could simply be obtained by varying the parameters or initial values of the algorithm producing the segmentations. However, in many cases, parameters of the algorithms cannot be modified, and segmentations are partially edited by a user. For manual or semi-manual segmentations, it is possible to estimate the inter-expert variability on a few cases but it usually cannot be applied on large databases due to the amount of resources required.

This is why it is important to automate the generation of plausible segmentations, which are "similar to" a given segmentation of a region of interest (ROI). This is the objective of this chapter which, to the best of our knowledge, has not been tackled before. It is naturally connected to several prior work in the field of image segmentation. Indeed, A large amount of generative models have been developed to compute segmentations based on a single image. For instance, deformable models [McInerney and Terzopoulos, 1996] or Markov Random Fields (MRF) [Wang et al., 2013] have been extensively studied in order to combine a data term and a smoothness prior term to compute realistic segmentations. These models are usually used to infer the maximum a posteriori segmentation, and rarely to sample from the model which can be computationally expensive [Niethammer et al., 2015].

[Chang and Fisher III, 2011, Fan et al., 2007] have proposed segmentation approaches based on Markov Chain Monte Carlo where parameter sampling leads to an estimation of the posterior probability of obtaining a segmentation given an image. In those approaches however, the algorithm defines the likelihood and prior functions and then estimates the most probable (or the expected) segmentation whereas in ISS the objective is to sample directly from the posterior distribution, knowing only its mean or mode.

Other methods [De Bruijne and Nielsen, 2004, Petersen et al., 2010] rely on sampling in order to find the most probable segmentation. It is particularly useful when the object of interest is not clearly visible or partially occluded. In this case, segmentation methods using segmentation samples have been developed in order to introduce prior knowledge on the shape of the expected segmentation. This prior knowledge can for instance result from a point distribution model defined using a database of previously segmented shapes. This is not directly applicable in our

case since we do not assume such a database is available. Moreover, it may not necessarily be useful in the case of brain tumors for instance, which do not have a typical shape.

Other related approaches [Pohl et al., 2007, Sabuncu et al., 2010, Warfield et al., 2004] aim at producing a consensus segmentation given several expert segmentations, or several atlas segmentations. They define probabilities of having a given segmentation based on a reference one, and their generative nature makes them suitable for ISS. Typical examples are the STAPLE algorithm [Warfield et al., 2004], the log-odds maps [Pohl et al., 2007] and their refinement [Sabuncu et al., 2010]. However, as shown in section 5.2, the segmentations generated from a single expert segmentation lack plausibility, and the spatial regularity of the contours cannot be finely controlled.

In this chapter, a novel framework is introduced to sample segmentations automatically leading to visually plausible delineations. More precisely, the proposed approach incorporates knowledge about image saliency of the ROI such that the sampled contours' variability may be greater at poorly contrasted regions, and smaller near sharp image gradients. Furthermore, the proposed approach is mathematically well grounded, and enforces the spatial smoothness of the contours, because it relies on Gaussian processes defined on implicit contours. Finally, segmentation sampling can be performed efficiently even on large medical images thanks to an algorithm using the structure of the image and the covariance matrix. Variability in the samples is easily controlled by a single scalar. We also exhibit an application of the method to radiotherapy dose planning.

5.2 Existing Generative Models of Segmentations

This section reviews relevant generative models of segmentations proposed in the literature. Results are illustrated on a synthetic image (Figure 5.1) for which the structure border is surrounded by regions of low and high contrast.

The probabilistic atlases [Pohl et al., 2007] derived from log-odds of signed distance functions assume that voxels are independently distributed with a Bernoulli probability density function of parameter b whose value depends on the distance to the structure border. The STAPLE algorithm [Warfield et al., 2004] is a region formulation for producing consensus segmentations. Given a binary segmentation T and expert sensitivity p and specificity q , the algorithm is associated with a generative model for which a segmentation D can be sampled knowing T as a Markov Random Field with the likelihood term

$$P(D_i = 1) = pP(T_i = 1) + (1 - q)P(T_i = 0) \quad (5.1)$$

and a prior accounting for local spatial coherence. Segmentations are generated by sampling independently the Bernoulli distribution at each voxel followed by a number of Iterated Conditional Modes (ICM) relaxation steps. Various ISS results

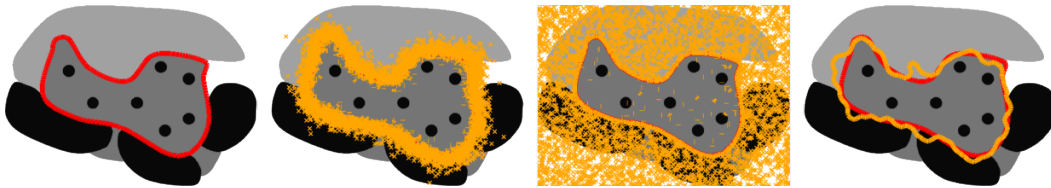


Figure 5.1: From left to right: synthetic image with region of interest outlined in red; segmentation sampling based on log-odds; segmentation sampling based on STAPLE without ICM steps ($p = 97\%$ and $q = 97\%$); ISS based on STAPLE with ICM steps ($p = 97\%$ and $q = 97\%$). The ground truth is outlined in red, the samples are outlined in orange.

are obtained in Figure 5.1 for the log-odds and STAPLE generative models with specified parameters.

In all cases, the produced segmentations are not realistic for two reasons. First, the variability of the segmentation does not account for the intensity in the image such that borders with strong gradients are equally variable as borders with weak gradient. This is counter intuitive as the basic hypothesis of image segmentation is that changes of intensity are correlated with changes of labels. Second, borders of the segmented structures are unrealistic mainly due to their lack of geometric regularity (high frequency wobbling in Figure 5.1 (Right)). While anatomical or pathological structure borders are not necessarily smooth (e.g. highly diffuse tumors), the generated samples show irregular generated contours in the presence of regular visible contours in the image, which is not plausible.

5.3 GPSSI

5.3.1 Definition

We propose a generative model of image segmentation that overcomes the two limitations of the presented previous approaches. First, sampled segmentations do take into account the image intensity by replacing the signed distance functions with signed geodesic distance. Second, spatial consistency of the sampled segmentations is enforced by describing a probabilistic segmentation with a Gaussian process with a squared exponential covariance, which allows to easily control the spatial coherence of the segmentation. The geodesic distance makes voxels far away from the mean segmentation if they are separated from it by high gradient intensity regions. Therefore, a random perturbation on the mean segmentation is unlikely to reach those voxels with high contrast, and more likely to affect voxels with low geodesic distance, i.e. voxels neighboring the mean segmentation with similar intensity values.

A novel probabilistic framework of image segmentation is introduced by defining a level set function via a Gaussian process (GP). We name the method GPSSI for Gaussian Process for Sampling Segmentations of Images. The mean of the GP is

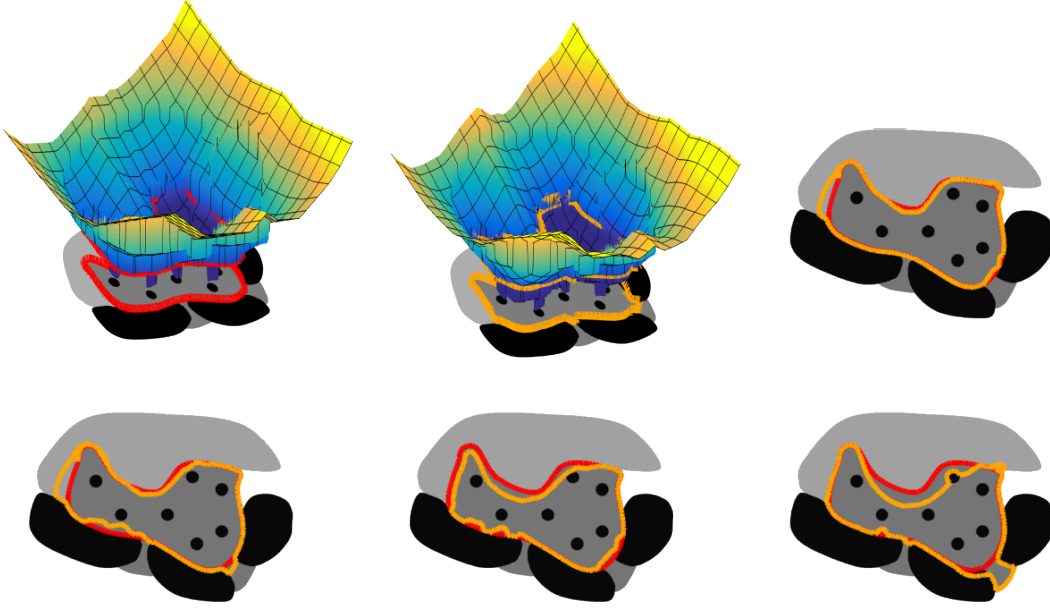


Figure 5.2: (Top Left) Mean of the GP μ ; (Top Middle) Sample of the level set function $\varphi(\mathbf{a})$ drawn from $\mathcal{GP}(\mu, \Sigma)$; (Others) GPSSSI samples. The ground truth is outlined in red, the GPSSSI samples are outlined in orange.

given by a signed geodesic distance, and its covariance is defined with a squared exponential driven by the Euclidean distance between voxels. Gaussian process implicit surfaces have been introduced previously by [Williams and Fitzgibbon, 2007] as a generalization of thin plate splines and used recently by [Gerardo-Castro et al., 2013] for surface reconstruction. However, our approach combining geodesic and Euclidean distance functions for the mean and covariance is original, and specifically suited to represent probabilistic image segmentations.

5.3.2 Geodesic Distance Map

Signed geodesic distance maps are computed as

$$\mathcal{G}(\mathbf{a}) = \min_{\Gamma \in \mathcal{P}_{\text{seg}, \mathbf{a}}} \int_0^1 \sqrt{\|\mathbf{\Gamma}'(s)\|^2 + \gamma^2 \left(\nabla \mathcal{I}(\mathbf{\Gamma}(s)) \cdot \frac{\mathbf{\Gamma}'(s)}{\|\mathbf{\Gamma}'(s)\|} \right)^2} ds \quad (5.2)$$

where \mathcal{I} is the input image, $\mathcal{P}_{\text{seg}, \mathbf{a}}$ is the set of all paths between the voxel \mathbf{a} and the segmentation, and $\mathbf{\Gamma}$ one such path, parametrized by $s \in [0, 1]$, with spatial derivative $\mathbf{\Gamma}'(s) = \partial \mathbf{\Gamma}(s) / \partial s$. The parameter γ sets the trade-off between Euclidean distance ($\gamma = 0$) and gradient information. Its implementation is based on a fast grid sweeping method as proposed by [Toivanen, 1996] and used in [Criminisi et al., 2008]. The gradient is computed with a Gaussian kernel convolution controlled by parameter h . The signed geodesic distance is set negative inside the segmentation, and positive outside.

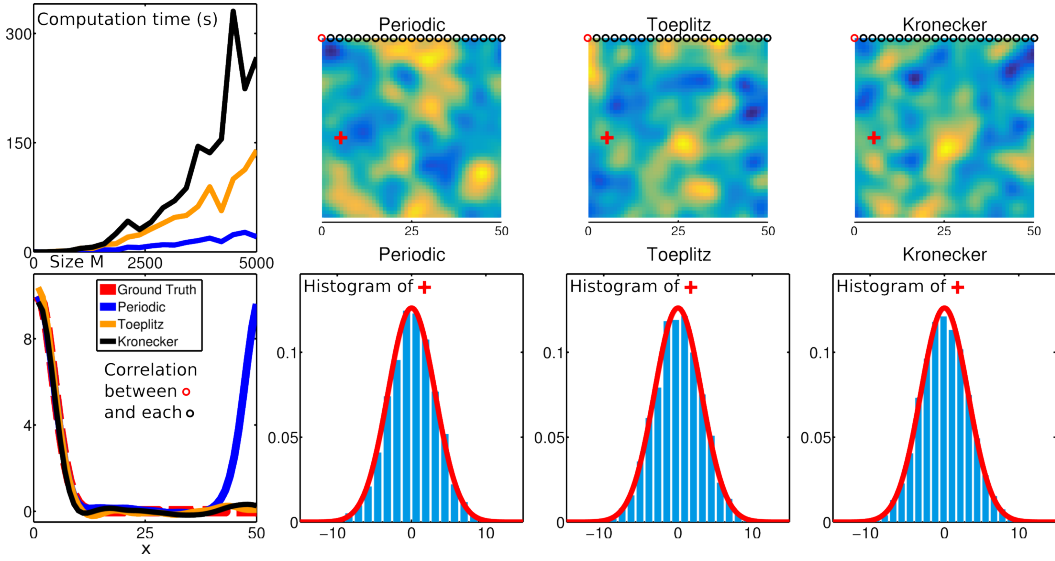


Figure 5.3: (Top row, from left to right) Computation time (seconds) for the sampling of $3 M \times M$ Gaussian processes with $\omega_0 = 10$ and $\omega_1 = 5$, function of the size M . Example of a 50×50 sample using periodic boundary conditions on the image, circulant embedding of the Toeplitz matrix, and the Kronecker decomposition. (Bottom row, from left to right) Sample correlation between the point at the top left corner (red circle) and the points of the first row (black circle) for 5000 Gaussian process samples of size 50×50 . The red line is the expected correlation $f_1(a) = \omega_0 \exp(-a^2/\omega_1^2)$. Histogram of 5000 realizations of a point (red cross) of a 50×50 Gaussian process using periodic boundary conditions on the image, circulant embedding of the Toeplitz matrix, and the Kronecker decomposition. The red line represents the expected density $f_2(x) = 1/\sqrt{2\pi\omega_0} \exp(-x^2/(2\omega_0))$.

5.3.3 GPSSI

Gaussian processes (GP) are a generalization of multivariate Gaussian distributions, and provide a framework to define probability distributions over functions. GP are widely used in machine learning for solving inference problems [Williams and Rasmussen, 2006] over spatially correlated datasets. In this chapter, it is the generative nature of GP that is of interest, since they naturally produce spatially smooth samples.

In GPSSI, a segmentation over a set Ω is defined via a level set function $\varphi(\mathbf{a})$, $\mathbf{a} \in \Omega$ such that its zero level set corresponds to the boundary of the ROI. Smoothness in the level set function φ translates into the smoothness of the boundary $\mathcal{B}_\varphi = \{\mathbf{a} \in \Omega \mid \varphi(\mathbf{a}) = 0\}$. A GP is fully defined by its mean and covariance functions: its mean value is set to the signed geodesic distance $\mu(\mathbf{a}) = \mathcal{G}(\mathbf{a})$ while its covariance is chosen as the squared exponential function,

$$\forall \mathbf{a}, \mathbf{b} \in \Omega, \quad \Sigma(\mathbf{a}, \mathbf{b}) = \omega_0 \exp\left(-\frac{\|\mathbf{a} - \mathbf{b}\|^2}{\omega_1^2}\right) \quad (5.3)$$

This choice of covariance enforces the smoothness of the segmentation, with parameter ω_1 characterizing the typical correlation length between two voxels while ω_0 controls the amount of variability of the level set function.

5.3.4 Efficient Sampling

Sampling of a GP is simply performed through the factorization of the covariance matrix at sample points. More precisely, let $\Omega_M = \{\mathbf{a}_i\}$, $i = 1 \dots M$ be the set of M discrete points \mathbf{a}_i where the level set function φ is defined. Typically, Ω_M may be the set of all voxel centers in the image. The covariance matrix $\Sigma_{ij}^{MM} = \omega_0 \exp(-\|\mathbf{a}_i - \mathbf{a}_j\|^2 / \omega_1^2)$ at sampled points is of size $M \times M$. To sample from a GP $\mathcal{GP}(\mu, \Sigma)$, a factorization of the covariance matrix $\Sigma^{MM} = LL^\top$ is required, such that given normally distributed variables $u \sim \mathcal{N}(0, \mathbb{I})$, GPSSI are simply computed as the zero crossing of $\mu + L(\omega_0, \omega_1)u \sim \mathcal{GP}(\mu, \Sigma)$.

A classical issue with GP sampling is that the factorization of Σ^{MM} becomes computationally expensive and ill-conditioned for large values of M . Since in practice $M \approx 10^7$, a regular matrix factorization - usually a Cholesky decomposition - in $\mathcal{O}(M^3)$ is computationally prohibitive. However, several methods exist to efficiently sample high dimensional GPs when the sample points form a regular grid and the covariance matrix is stationary (i.e. invariant by translation):

1. **Periodic boundary conditions** [Dietrich and Newsam, 1997, Kozintsev, 1999, Kozintsev and Kedem, 2000]. Assuming periodic boundary conditions on the image, Σ^{MM} is a Block Circulant with Circulant Blocks (BCCB) matrix such that each row of Σ^{MM} is a periodic shift of the first row of Σ^{MM} , $C \in \mathbb{R}^M$. C can be seen as an image of M voxels, whose voxel value is the evaluation of the square exponential covariance for every shift present in the image. Theoretical results on the BCCB matrix spectral decomposition give us

$$\Sigma^{MM} = F^{-1} \text{diag}(FC)F \tag{5.4}$$

where the complex matrix F is the $M \times M$ discrete Fourier transform matrix [Kozintsev, 1999]. Hence, the eigenvalues of Σ^{MM} are the discrete Fourier transform of C . As such, if $u_1, u_2 \sim \mathcal{N}(0, \mathbb{I})$ i.i.d, then the real and imaginary part of

$$F \sqrt{\text{diag}(FC)}(u_1 + iu_2) \tag{5.5}$$

are two independent samples from the GP [Kozintsev, 1999]. This can be efficiently computed using the Fast Fourier Transform without storing F . Samples can then be generated in $\mathcal{O}(M \log(M))$ (Figure 5.3 Top Left).

2. **Circulant embedding of the Toeplitz matrix** [Dietrich and Newsam, 1997, Kozintsev, 1999, Kozintsev and Kedem, 2000]. If periodic boundary conditions are not applied, Σ^{MM} is a block Toeplitz with Toeplitz blocks matrix.

This matrix can be embedded in a larger Σ^{2M2M} BCCB matrix. Hence, as previously, samples can be drawn in $\mathcal{O}(M \log(M))$ (Figure 5.3 Top Left).

3. **Kronecker product** [Gilboa et al., 2015, Lorenzi et al., 2015, Saatçi, 2012]. Another approach is to note that the chosen covariance function is separable. In the 3-dimensional case,

$$\begin{aligned} \forall \mathbf{a}, \mathbf{b} \in \Omega, \\ \Sigma^{MM}(\mathbf{a}, \mathbf{b}) = \omega_0 \exp\left(-\frac{(\mathbf{a}_x - \mathbf{b}_x)^2}{\omega_1^2}\right) \exp\left(-\frac{(\mathbf{a}_y - \mathbf{b}_y)^2}{\omega_1^2}\right) \exp\left(-\frac{(\mathbf{a}_z - \mathbf{b}_z)^2}{\omega_1^2}\right) \end{aligned} \quad (5.6)$$

Then,

$$\Sigma^{MM} = \Sigma^{M_x M_x} \otimes \Sigma^{M_y M_y} \otimes \Sigma^{M_z M_z} \quad (5.7)$$

where $\Sigma^{M_x M_x} \in \mathbb{R}^{M_x \times M_x}$, $\Sigma^{M_y M_y} \in \mathbb{R}^{M_y \times M_y}$, and $\Sigma^{M_z M_z} \in \mathbb{R}^{M_z \times M_z}$ are the covariance matrices along the 3 dimensions, and \otimes denotes the Kronecker product. This way, a Cholesky decomposition of Σ^{MM} can be obtained through the individual factorization of $\Sigma^{M_x M_x}$, $\Sigma^{M_y M_y}$, and $\Sigma^{M_z M_z}$. Samples can then be drawn in $\mathcal{O}(M_x \log(M_x))$, assuming $M_x > M_y$, and $M_x > M_z$ (Figure 5.3 Top Left). Moreover, leveraging matrix/vector products and properties of the Kronecker product, the full factorization of Σ^{MM} needs not be stored [Gilboa et al., 2015].

We first check the computation time (Figure 5.3 top left). We can see that using the Kronecker product takes more time than the Circulant embedding of the Toeplitz matrix, which in turn is more time consuming than assuming periodic boundary condition on the image. However, we noticed that the Kronecker product is more stable for large ω_1 . As such, we chose this method in the rest of the chapter since the size of the images used was not computationally prohibitive. Examples of samples using the three methods can be seen on Figure 5.3 (top). We further check the samples against the ground truth. We compute the sample correlation between the pixel on the top left and the pixels of the first row using 5000 samples. The computed correlation is close to the theoretical correlation $f_1(a) = \omega_0 \exp(-a^2/\omega_1^2)$. We also plot the histogram of the 5000 samples of the pixel on the top left and retrieve the density $f_2(x) = 1/\sqrt{2\pi\omega_0} \exp(-x^2/(2\omega_0))$.

5.4 Parameter Settings

In the proposed approach, segmentation sampling depends on the scale h of the gradient operator, the parameter γ of the geodesic map, and the parameters ω_0 and ω_1 of the covariance function. The parameter h depends on the level of noise in the

image (typically chosen as 1 voxel size) whereas γ controls the importance of the geodesic term. In our experiments, we set $\gamma = 100/\mathbb{E}(\mathcal{I})$, where $\mathbb{E}(\mathcal{I})$ is the mean of 5th to the 95th percentiles of the image intensity.

The parameter ω_1 controls the smoothness scale of the structure, and is chosen as the radius of the equivalent sphere. In 3D, given the volume V of the ROI, we set $\omega_1 = (3/(4\pi)V)^{\frac{1}{3}}$.

The parameter ω_0 controls the variability around the mean shape: the greater ω_0 , the greater the variability. Such variability may be practically quantified for instance in terms of mean inter-sample Dice's coefficient between any pair of expert segmentations. In such case, it is easy to find ω_0 corresponding to a given inter-sample Dice's coefficient (see Figure 5.4 middle right). This approach offers an intuitive way to semi-automatically set the parameter ω_0 . Another way of setting the parameter ω_0 is to relate it to the mean Dice's coefficient between the samples and the input segmentation (see Figure 5.4 middle left). Instead of Dice's coefficient, one could also use quantiles of histograms of symmetric distances between contours.

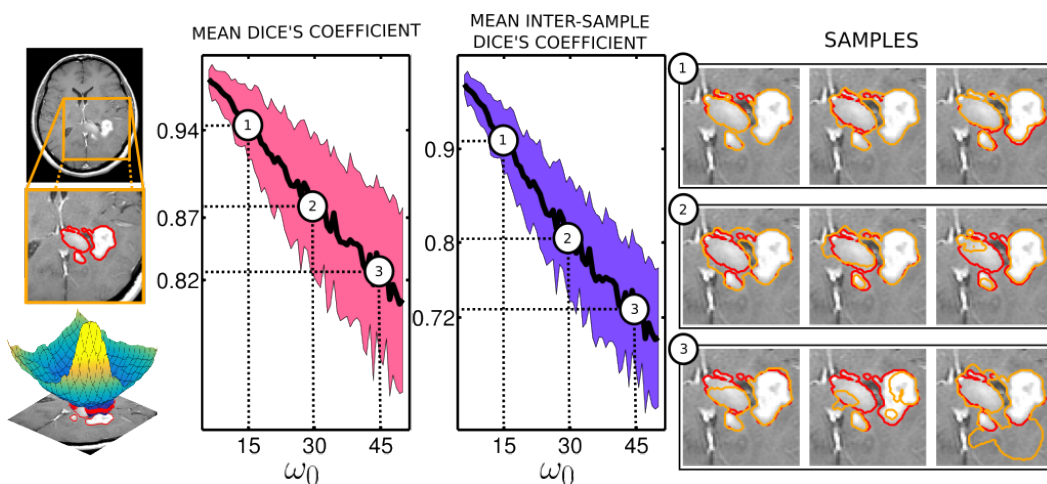


Figure 5.4: (Left) Segmentation of brain tumor active rim from T1 MR image with Gadolinium contrast agent; (Middle Left) Relationship between the parameter ω_0 and the mean Dice's coefficient between 40 samples and the clinical segmentation; (Middle Right) Relationship between the parameter ω_0 and the mean inter-sample Dice's coefficient using 40 samples; (Right) Samples for different ω_0 . The clinician segmentation is outlined in red, the GPSSI samples are outlined in orange.

Another approach is to let a user define a confidence region where the segmentations should lie. Let the user choose the two tightest isocontours $\pm D$ of the geodesic distance which enclose this confidence region. Note that for a voxel \mathbf{a} on the defined isocontours, we have $\varphi(\mathbf{a}) \sim \mathcal{N}(\mu(\mathbf{a}) = \pm D, \sigma = \sqrt{\omega_0})$. We can then define ω_0 based on the 95% confidence interval for the normal distribution that the sample will not be negative (i.e. included in the segmentation),

$$D = 2\sigma = \sqrt{\omega_0} \implies \omega_0 = \left(\frac{D}{2}\right)^2 \quad (5.8)$$

Figure 5.5 shows an example where we set ω_0 such that the samples most probably lie in a region delineated by the isocontours $\mu(\mathbf{a}) = \pm 45$.

5.5 Segmentation Sampling

Samples of the 2D synthetic segmentation case can be seen on Figure 5.2 with $\omega_0 = 506$ corresponding to a mean inter-sample Dice's coefficient of 80%. Samples are coherent with the visible image boundary since most samples do not include highly contrasted (black) regions of the image but instead invade low contrast regions of the image.

Segmentation sampling was also performed on a 3D T1 post contrast MRI (T1Gd MRI) where the proliferative part (active rim) of a grade IV glioma was segmented by an expert (Figure 5.4 left). The strong correlation between the covariance parameter ω_0 and the mean inter-sample Dice's coefficient as well as the mean Dice's coefficient against the clinician segmentation was computed after generating 40 samples for each value of ω_0 (Figure 5.4 right). Thus the user may easily choose ω_0 as a function of the desired Dice's coefficient.

Note that the likelihood of samples generated from $\mathcal{GP}(\mu, \Sigma)$ is not very informative as it is computed over the whole image and not just the generated contour.

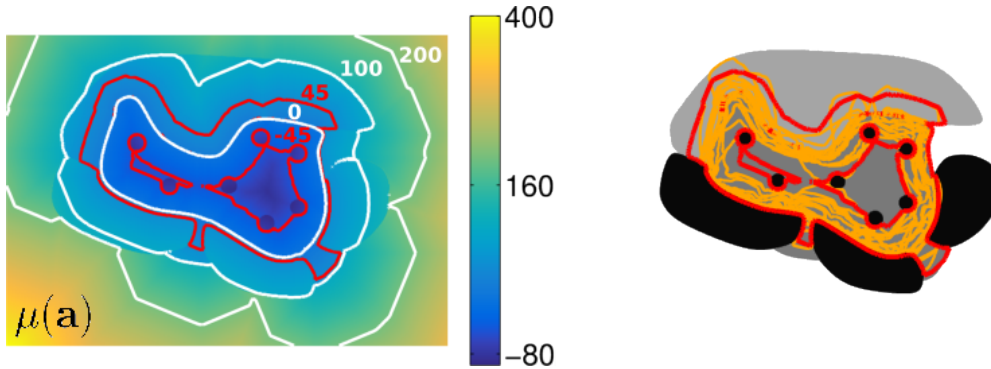


Figure 5.5: (Left) Signed geodesic distance $\mu(\mathbf{a})$ of the ROI with isocontours -45, 0, 45, 100, 200. (Right) One can check that the samples most probably lie in the region delineated by the isocontours $\mu(\mathbf{a}) = \pm 45$ (in red). The sampled contours are in orange.

5.6 GPSSI Extensions

5.6.1 Several Neighboring Structures

The presented method can directly be used to sample several ROIs. However, when the structures are close to each other, the sampled structures may overlap. In such

case, it is important to sample them jointly to define no-overlapping segmentations. Based on [Zhao et al., 1996], the different ROIs can be defined using different level sets. For two structures, one can define two Gaussian processes $\varphi_1 \sim \mathcal{GP}(\mu_1, \Sigma_1)$ and $\varphi_2 \sim \mathcal{GP}(\mu_2, \Sigma_2)$, where μ_1 and μ_2 are the signed geodesic distances from the two considered ROIs, and Σ_1 and Σ_2 are the corresponding covariance matrices. As such, non-overlapping samples of the two ROIs \mathcal{S}_1 and \mathcal{S}_2 can be defined as the ensembles (Figure 5.6):

$$\mathcal{S}_1 = \{\mathbf{a} \mid \varphi_1(\mathbf{a}) \leq 0 \text{ and } \varphi_1(\mathbf{a}) \leq \varphi_2(\mathbf{a})\} \quad (5.9)$$

$$\mathcal{S}_2 = \{\mathbf{a} \mid \varphi_2(\mathbf{a}) \leq 0 \text{ and } \varphi_2(\mathbf{a}) < \varphi_1(\mathbf{a})\} \quad (5.10)$$

Figure 5.11 shows examples of 2 structure samples: non-overlapping samples of a glioma and brainstem segmented by a clinician on a T1Gd MRI were computed using the parameters as defined in the previous section, and a manually set ω_0 for a mean inter-sample Dice’s coefficient of 83% for the glioma and 85% for the brainstem. Unlike [Vese and Chan, 2002], one needs as many level sets as the number of neighboring ROIs for the sampling, because a specific set of parameters ω_0 and ω_1 is associated with each structure. The assignment of labels in the overlapping region is then assigned to the minimum level set function.

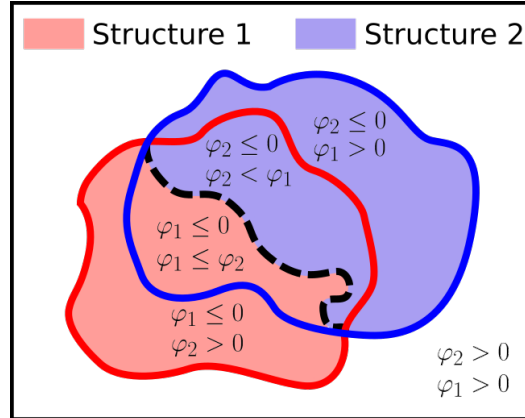


Figure 5.6: Sampling two non-overlapping structures can be achieved using 2 different level-sets $\varphi_1 \sim \mathcal{GP}(\mu_1, \Sigma_1)$ and $\varphi_2 \sim \mathcal{GP}(\mu_2, \Sigma_2)$.

5.6.2 Accounting for Under and Over Segmentation

Over or under segmentation can be one of the major differences between the performance of two experts. This effect can be easily incorporated in this framework by adding a variable ε such that the level set function $\varphi \sim \mathcal{GP}(\mu + \varepsilon, \Sigma(\omega_0, \omega_1))$. If $\varepsilon > 0$, the samples will on average result in under segmentation, if $\varepsilon < 0$ the samples will on average result in over segmentation. Examples of under and over segmentation can be seen on Figure 5.7 (Middle) where under segmentation is achieved with $\varepsilon = +20$ and over segmentation with $\varepsilon = -20$. This parameter can be randomly

sampled around 0 when sampling segmentations in order to take under and over segmentation into account.

5.6.3 Inclusion or Exclusion of Structures

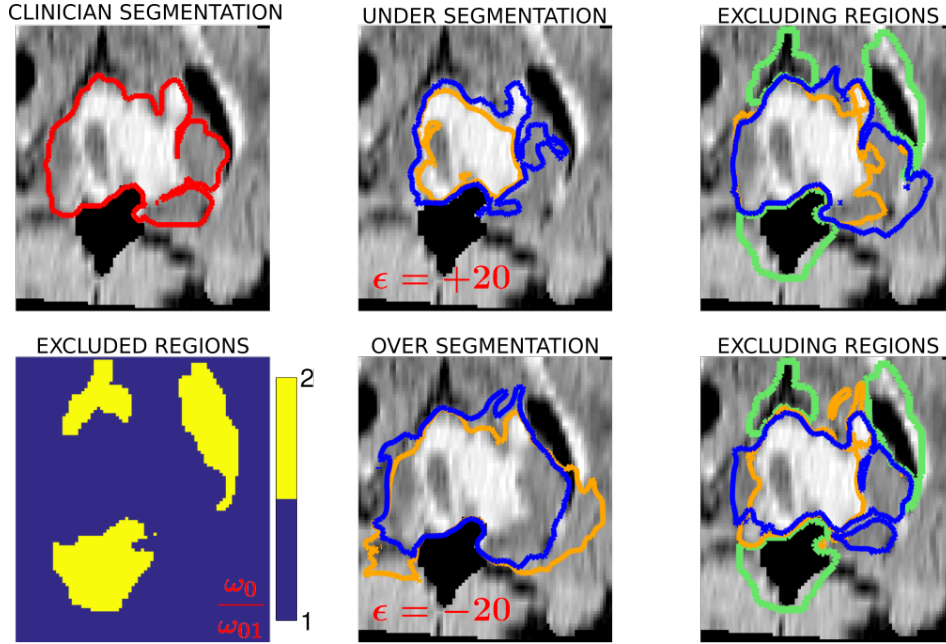


Figure 5.7: From top to bottom, left to right: clinician segmentation of a glioma on a T2-FLAIR MRI; factor ω_0/ω_{01} used to normalize the signed geodesic distance μ to exclude the region in yellow; under segmentation samples (in orange and blue) using $\varepsilon = +20$; over segmentation samples (in orange and blue) using $\varepsilon = -20$; samples (in orange and blue) where regions around the brainstem and ventricle (in green) were forced to be excluded by multiplying the signed geodesic distance μ by the spatially varying factor ω_0/ω_{01} .

To provide anatomically consistent segmentation, it can be interesting to force specific regions of the image to stay excluded or included from the segmentation samples. For instance, it is expected that cerebrospinal fluid or skull regions would not be included in any glioma segmentations. In the GPSSI approach, this could be handled by making the ω_0 parameter spatially varying. However, such a covariance function would not necessarily be stationary nor positive definite. As such, using the fast sampling methods exposed in Section 5.3.4 would not be possible. Instead we propose to achieve a similar effect by keeping a stationary covariance function, but modifying the mean of the Gaussian process μ . Indeed, we know that we have $\varphi(\mathbf{a}) \sim \mathcal{N}(\mu(\mathbf{a}), \omega_0)$ for each voxel \mathbf{a} by marginalizing over the rest of the voxels. We want to force the voxel to stay outside or inside of the samples. This can be done by forcing the variance to a lower value such that $\varphi_1(\mathbf{a}) \sim \mathcal{N}(\mu(\mathbf{a}), \omega_{01}(\mathbf{a}))$ where $\omega_{01}(\mathbf{a}) < \omega_0$. In other words, we are more confident about the labeling of \mathbf{a} .

One can note that the probability of \mathbf{a} to be inside the segmentation is

$$P(\varphi_1(\mathbf{a}) \leq 0) = P\left(\varphi(\mathbf{a}) + \mu(\mathbf{a}) \left(\frac{\omega_0}{\omega_{01}(\mathbf{a})} - 1\right) \leq 0\right) \quad (5.11)$$

where

$$\varphi(\mathbf{a}) + \mu(\mathbf{a}) \left(\frac{\omega_0}{\omega_{01}(\mathbf{a})} - 1\right) \sim \mathcal{N}\left(\mu(\mathbf{a}) \frac{\omega_0}{\omega_{01}(\mathbf{a})}, \omega_0\right) \quad (5.12)$$

One can then "mimic" this spatially varying confidence that a voxel should be included or excluded from the segmentation by simply normalizing the signed geodesic distance μ with a spatially varying factor. In other words, a Gaussian process with a normalized mean μ has the same voxel-wise marginalized distribution as a Gaussian process with spatially varying ω_0 . Segmentation samples of a glioma on a T2-FLAIR MRI are shown on Figure 5.7 (Right) where a region around the brainstem and ventricles is forced outside of the samples by setting $\omega_0/\omega_{01} = 2$.

5.6.4 General Covariance Matrix Using Supervoxels

In so far, we have detailed a method to efficiently compute segmentation samples using the squared exponential covariance function. A stationary covariance function was necessary in order to factorize the covariance matrix. However, one could be interested in using more general covariance functions. In this section, we describe how the use of supervoxels can help to sample Gaussian processes with more general covariance functions.

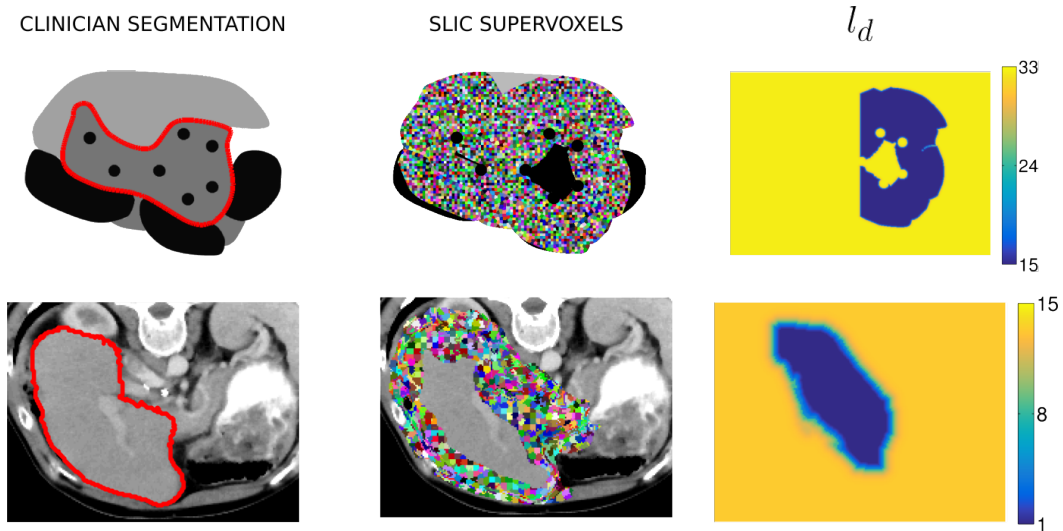


Figure 5.8: From left to right: clinician segmentation of a liver on a CT image, SLIC supervoxels used for the sampling, correlation length $l_1 = l_2 = l_3 = l_d$ for two different slices. For the liver, the correlation length is set to a lower value away from the rib cage to account for the noisier aspect of the contour.

For instance, it can be of interest to sample segmentations whose smoothness is spatially inhomogeneous, when a structure presents both a regularly shaped outline and more irregular parts. To model this, the covariance function introduced by [Gibbs, 1998] and detailed in [Williams and Rasmussen, 2006] is of particular interest,

$$\forall \mathbf{a}, \mathbf{b} \in \Omega, \\ \Sigma(\mathbf{a}, \mathbf{b}) = \omega_0 \prod_{d=1}^D \left(\frac{2l_d(\mathbf{a})l_d(\mathbf{b})}{l_d^2(\mathbf{a}) + l_d^2(\mathbf{b})} \right)^{\frac{1}{2}} \exp \left(- \sum_{d=1}^D \frac{(\mathbf{a}_d - \mathbf{b}_d)^2}{l_d^2(\mathbf{a}) + l_d^2(\mathbf{b})} \right) \quad (5.13)$$

where D is the dimension of the input ($D = 2$ for an image and $D = 3$ for a volume), and l_d is any positive function defining a spatially varying correlation length. Note that if $l_d = p$ is a constant, we retrieve the squared exponential covariance function, $\Sigma(\mathbf{a}, \mathbf{b}) = \omega_0 \exp(-(\|\mathbf{a} - \mathbf{b}\|^2)/(2p^2))$.

However, for spatially varying l_d , the covariance function is neither stationary nor separable. To make the computations tractable, we propose to use supervoxels. The method is as follow:

- Compute the signed geodesic distance as before.
- Decompose the image into supervoxels having roughly homogeneous intensity. We use the SLIC algorithm developed by [Achanta et al., 2012] as it provides realistic supervoxels in linear time. We extended the algorithm such that the supervoxels respect the input ROI boundary. This is done by limiting the nearest neighbor search to voxels belonging to similar ROIs (ROI and background).
- Compute the covariance matrix defined on the set \mathcal{B} of barycenters of the supervoxels.
- Sample the Gaussian process defined over the set of supervoxels with covariance matrix Σ by computing the Cholesky decomposition of Σ , and interpolate it using a triangulation-based linear interpolation.

Figure 5.8 shows the clinician segmentation, the computed supervoxels, and the correlation length l_d for a 2D synthetic case, and one slice of a 3D liver CT scan. To speed up the computation, only the supervoxels around the boundary are considered, for a total of 4, 279 supervoxels for the synthetic image, and 14, 528 for the liver. The spatially varying correlation length l_d is set equal for every $d = 1, 2, 3$. A smaller correlation length has been set on a region of the liver which is expected to be less regular (away from the rib cage). Two examples of the resulting samples are presented on Figure 5.9. To emphasize the spatial difference in regularity, we also present the level set function variation around the mean $\varphi - \mu$ for the sample $\varphi \sim \mathcal{GP}(\mu, \Sigma)$.

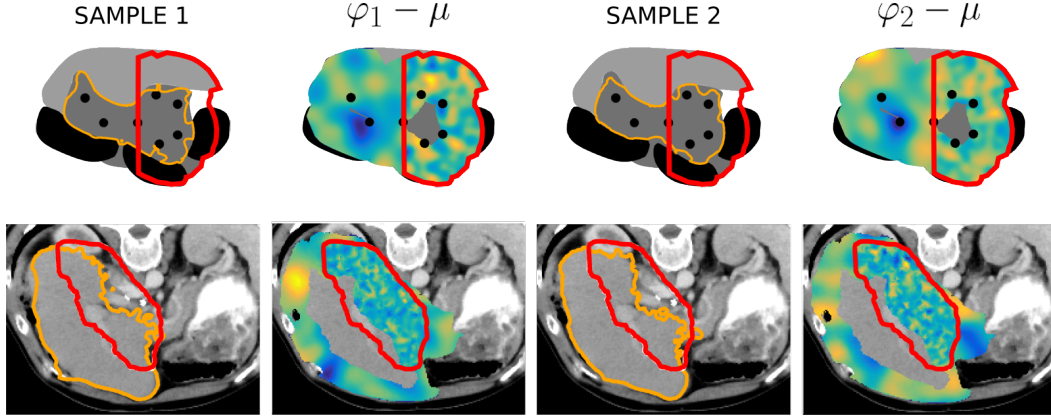


Figure 5.9: (Top) Synthetic case; (Bottom) 3D liver segmentation. From left to right: sample of a segmentation, corresponding level set variation $\varphi_1 - \mu$ with $\varphi_1 \sim \mathcal{GP}(\mu, \Sigma)$, additional sample, corresponding level set variation $\varphi_2 - \mu$ with $\varphi_2 \sim \mathcal{GP}(\mu, \Sigma)$. For clarity, the region of low correlation length is outlined in red. Note how the orange contours are more irregular inside the region outlined in red.

5.6.5 Plausibility of the Samples: Evaluation on multiple segmentations

In this section, we present an assessment of the visual plausibility of the samples, using tumor segmentations from the BraTS challenge [Menze et al., 2015]. In other words, we test if the manual segmentations of the same structure could have been generated by GPSSI if one of the segmentations was considered as the true one.

Algorithm 1 Sampling segmentations close to the target

Data: Source segmentation \mathcal{S}_0 ; target segmentation \mathcal{S} ; proposal distributions Q_1 , Q_2 , and Q_3 ; number of iterations K

Result: Samples close to the target segmentation

```

initialize  $\omega_0$ ,  $\omega_1$ , and  $\varepsilon$  while  $r \leq K$  do
     $\hat{\omega}_0 = Q_1(\omega_0)$   $\hat{\omega}_1 = Q_2(\omega_1)$   $\hat{\varepsilon} = Q_3(\varepsilon)$  Sample  $\mathcal{S}^r \sim \mathcal{GP}(\mu(\mathcal{S}_0) + \hat{\varepsilon}, \Sigma(\hat{\omega}_0, \hat{\omega}_1))$ 
    Compute the likelihood  $L^r = P(\mathcal{S}^r | \hat{\varepsilon}, \hat{\omega}_0, \hat{\omega}_1)$  Compute the acceptance ratio
     $\mathcal{A} = \min(1, L^r / L^{r-1})$  Sample  $u$  uniform between 0 and 1 if  $u < \mathcal{A}$  then
    |  $\omega_0 = \hat{\omega}_0$   $\omega_1 = \hat{\omega}_1$   $\varepsilon = \hat{\varepsilon}$ 
    end
     $r+ = 1$ 
end
    
```

Consider a tumor which has been manually segmented by $k + 1$ experts (Figure 5.10). Noting \mathcal{S}_i the segmentation from expert i , for $i = 0, \dots, k$, the goal is to generate segmentations close to $\{\mathcal{S}_i\}_{i=1, \dots, k}$ from the input \mathcal{S}_0 , assumed to be the reference segmentation. More precisely, we assume that

$$\text{for } i = 1, \dots, k \quad \mathcal{S}_i \sim \mathcal{GP}(\mu(\mathcal{S}_0) + \varepsilon^i, \Sigma(\omega_0^i, \omega_1^i)) \quad (5.14)$$

where ω_0^i and ω_1^i are the parameters of the squared exponential covariance function, ε^i is the parameter taking into account over or under segmentation, and $\mu(\mathcal{S}_0)$ is the signed geodesic distance from \mathcal{S}_0 . For clarity of the notations, we drop the i index for the parameters in the rest of the chapter. Since ω_0 , ω_1 , and ε are unknown, we resort to Markov Chain Monte Carlo (MCMC) sampling to produce samples close to the target segmentation \mathcal{S} . Following Bayes rule, and assuming independence of the parameters, we have

$$P(\varepsilon, \omega_0, \omega_1 | \mathcal{S}) \propto P(\mathcal{S} | \varepsilon, \omega_0, \omega_1) P(\varepsilon) P(\omega_0) P(\omega_1) \quad (5.15)$$

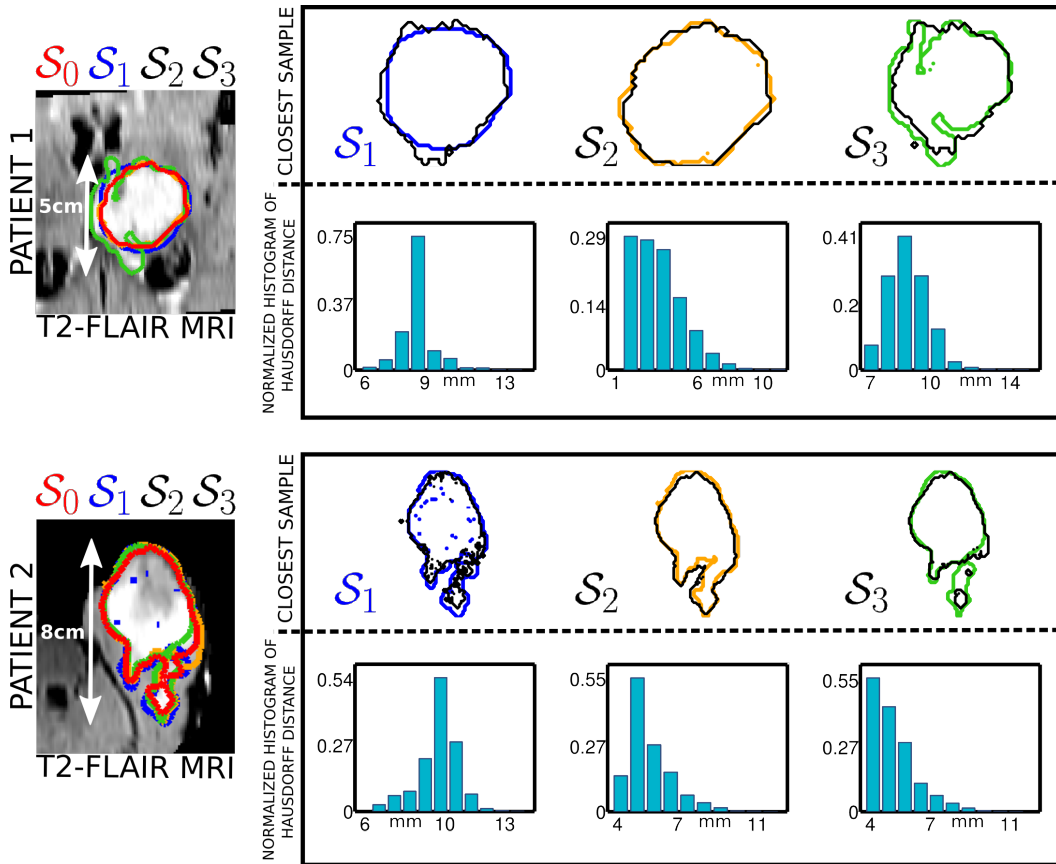


Figure 5.10: Patient 1 on top, Patient 2 on the bottom. From left to right: 4 clinician segmentations of a glioma on a T2-FLAIR MRI, the source segmentation \mathcal{S}_0 is the red one; closest sample in terms of Hausdorff distance in black with the corresponding target segmentation \mathcal{S}_i , $i = 1, 2, 3$, and normalized histogram of the Hausdorff distance between the target segmentation and the 20,000 samples.

We use uniform priors on $[-50, 50]$ for ε , $[1, 10000]$ for ω_0 , and $[1, 500]$ for ω_1 . We use normal proposal distributions Q_1 , Q_2 , and Q_3 for ε , ω_0 , and ω_1 respectively with a standard deviation of 2 for the three proposal distributions, set to reach an acceptance rate of approximately 50%. We define the likelihood,

$$P(\mathcal{S}_i|\varepsilon, \omega_0, \omega_1) = \exp\left(-\frac{H(\varepsilon, \omega_0, \omega_1)^2}{\sigma^2}\right) \quad (5.16)$$

where $H(\varepsilon, \omega_0, \omega_1)$ is the 99th percentile of the symmetric Hausdorff distance between the boundary of \mathcal{S}_i and the boundary of a random sample from $\mathcal{GP}(\mu(\mathcal{S}_0) + \varepsilon^i, \Sigma(\omega_0^i, \omega_1^i))$, and σ is a noise level set to 4 mm. Note that this likelihood is handcrafted because we observe contours of the clinician segmentations, and not level set functions. The algorithm is described in details in Algorithm 1.

Results are shown on Figure 5.10 for two glioma patients which were segmented by $k + 1 = 4$ clinicians using 20000 samples. We randomly choose one of the four segmentations as the source segmentation, and consider the three other as targets. Figure 5.10 shows the samples which result in the lowest Hausdorff distance (i.e. highest likelihood) among the sampled ones. The samples are close to the clinician segmentations: but the fit between the best sample and segmentation \mathcal{S}_i depends on how far \mathcal{S}_i is from \mathcal{S}_0 . Based on the normalized histogram of Hausdorff distance, one can see for instance, that for patient 1 \mathcal{S}_3 is clearly further from \mathcal{S}_0 , whereas for patient 2 it is \mathcal{S}_1 . Note also that the parameter ω_1 (contour smoothness) is not well captured probably due to the nature of the Hausdorff distance. Although increasing the number of samples could further improve the match between the best sample and observed contours, this experiment show that GPSSI can release samples already close to real observed ones.

5.7 Tumor Delineation Uncertainty in Radiotherapy

The proposed method is applied to the uncertainty quantification of radiotherapy planning. The standard of care for grade IV gliomas (Figure 5.4) is the delivery of 60 Gray (Gy) to the Clinical Target Volume (CTV) which is defined as a 2-3cm extension of the Gross Tumor Volume (GTV) visible on a T1Gd MRI [Mason et al., 2007].

The following algorithm is applied to the patient shown in Figure 5.11:

- Sample a GTV and a brainstem segmentation sample from the clinician segmentations visible on Figure 5.11 (top left).
- Compute the CTV from the GTV. In order to take into account the natural boundaries of the tumor progression and its privileged paths of progression, we compute the CTV using the tumor tail extrapolation algorithm developed by [Konukoglu et al., 2010a], which models the infiltration of glioma cells in the brain parenchyma on a single time point. It takes into account the fact that glioma cells invade preferably white matter over gray matter, and that the cerebrospinal fluid and falx cerebri are boundaries for the tumor progression. More precisely, we compute the tumor cell density infiltration as the tail extrapolation from the sampled GTV. It is based on a segmentation of the brain into white matter, gray matter and cerebrospinal fluid. The CTV

is then defined as the largest volume enclosed by an isovalue of the tumor cell density, which is fully included in the 2cm isotropic extension of the GTV. Finally, the sampled brainstem is excluded from the CTV.

- Compute the prescribed dose for the CTV as 60 Gy targeted inside the CTV and 0 Gy elsewhere.

These steps were applied for 50 samples. Figure 5.11 shows the mean target dose and its standard deviation. Several strategies could be applied to take into account the uncertainty in the GTV delineation. Generally, radiotherapy planning has to find a compromise between delivering radiation to the tumor, and avoiding dose to radiosensitive tissues. Visualization of dose uncertainty may guide the physician in this process. For example, the radiation dose could be reduced in regions of high uncertainty if this allows for dose reductions in radiosensitive organs, and thereby reduces the risk of side effects substantially. Technically, the standard deviation of the target dose could be used in the optimization of the radiation beams to weight differently voxels at the border of the CTV where the dose target is less certain. Moreover, it is important to visualize areas that represent tumor with near certainty and should be treated with the prescribed dose. In the long term, tumor segmentation samples could be used for radiotherapy planning based on models of tumor control probability (TCP).

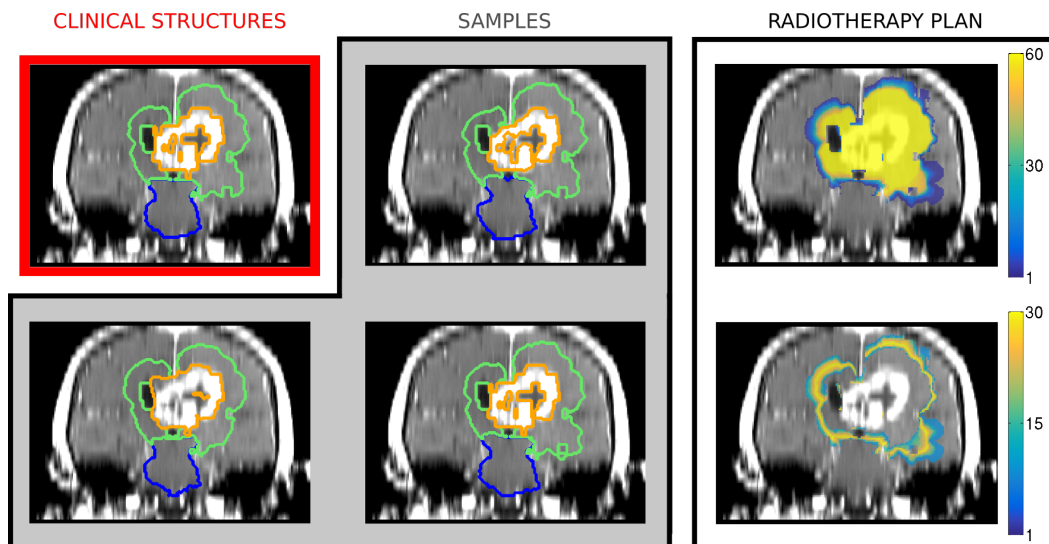


Figure 5.11: In the red box: the gross tumor volume (GTV) and the brainstem segmented by the clinician are in orange and blue respectively, the clinical target volume (CTV) is shown in green. In the gray box: samples of the GTV and brainstem in orange and blue respectively, corresponding CTV in green. In the white box, the average dose over 50 sampled GTV (top) and the dose standard deviation (bottom).

5.8 Conclusion

In this chapter, an original image segmentation sampling framework has been proposed to generate plausible segmentations close to an input one. The approach leads to spatially smooth contours that take into account the presence of salient features of the ROI in the image. Samples are efficiently generated, with a variability around a reference segmentation easily controlled by a single scalar. Several extensions have been proposed such as the sampling of several neighboring structures, taking into account under and over segmentation with a simple scalar parameter, and forcing the inclusion or the exclusion of certain part of the image from the samples. We provide a method to apply this sampling method to more general non-stationary covariance functions using supervoxels. The plausibility of the sampled contours originates from the inclusion of various constraints such as the intensity gradient, the presence of anatomical regions to be included or excluded, or the varying level of smoothness. To further improve the credibility, of the samples, one could further restrict the choice of covariance functions based on observed multiple segmentations of the same structure as hinted in section 5.6.5. Furthermore, this work could leverage the vast literature on Gaussian processes, imposing for instance convexity constraints on the samples [Da Veiga and Marrel, 2012].

Future work will also explore the incorporation of uncertainty in the radiotherapy dose planning. The proposed method could have several additional applications for instance to produce consensus segmentations from several expert ones. It could also be used to assess the confidence of the performance of segmentation algorithms in the context of segmentation challenges, by providing several likely segmentations around the ground truth segmentations. Finally, this method could be included in model personalization pipeline [Lê et al., 2015a] where segmentation is a crucial input. This would allow one to plan therapy based on personalized models which take into account the uncertainty in the data.

MRI Based Bayesian Personalization of a Brain Tumor Growth Model

Contents

6.1	Introduction	63
6.1.1	Motivations	63
6.1.2	Clinical Background	64
6.1.3	Modeling: Previous Work	64
6.1.4	Personalization: Previous Work	65
6.1.5	Contributions of the Chapter	66
6.2	Model	66
6.2.1	The Reaction-Diffusion Model	66
6.2.2	Model and MRIs	67
6.3	Simulation	68
6.3.1	Preprocessing of the data	68
6.3.2	Lattice Boltzmann Method	69
6.3.3	Initialization	69
6.4	Personalization	70
6.4.1	Spherical Asymptotic Analysis	71
6.4.2	BOBYQA Optimization	72
6.4.3	Bayesian Personalization	72
6.5	Results	74
6.5.1	Synthetic Case	74
6.5.2	Glioblastoma Patients	75
6.6	Discussion	78
6.7	Perspectives	80

Based On: the conference paper [Lê et al., 2015a] and the journal extension [Lê et al., 2016].

The mathematical modeling of brain tumor growth has been the topic of numerous research studies. Most of this work focuses on the reaction-diffusion equation model, which suggests that the diffusion coefficient and the proliferation rate can be related to clinically relevant information. However, estimating the parameters of the reaction-diffusion model is difficult because of the lack of identifiability of the parameters, the uncertainty in the tumor segmentations, and the model approximation, which cannot perfectly capture the complex dynamics of the tumor evolution. Our approach aims at analyzing the uncertainty in the patient specific parameters of a tumor growth model, by sampling from the posterior probability of the parameters knowing the magnetic resonance images of a given patient. The estimation of the posterior probability is based on: i) a highly parallelized implementation of the reaction-diffusion equation using the Lattice Boltzmann Method (LBM), and ii) a high acceptance rate Monte Carlo technique called Gaussian Process Hamiltonian Monte Carlo (GPHMC). We compare this personalization approach with two commonly used approaches based on the spherical asymptotic analysis of the reaction-diffusion model, and on a derivative-free optimization algorithm. We demonstrate the performance of the method on synthetic data, and on seven patients with a glioblastoma, the most aggressive primary brain tumor. This Bayesian personalization produces more informative results. In particular, it provides samples from the regions of interest and highlights the presence of several modes for some patients. In contrast, previous approaches based on optimization strategies fail to reveal the presence of different modes, and correlation between parameters.

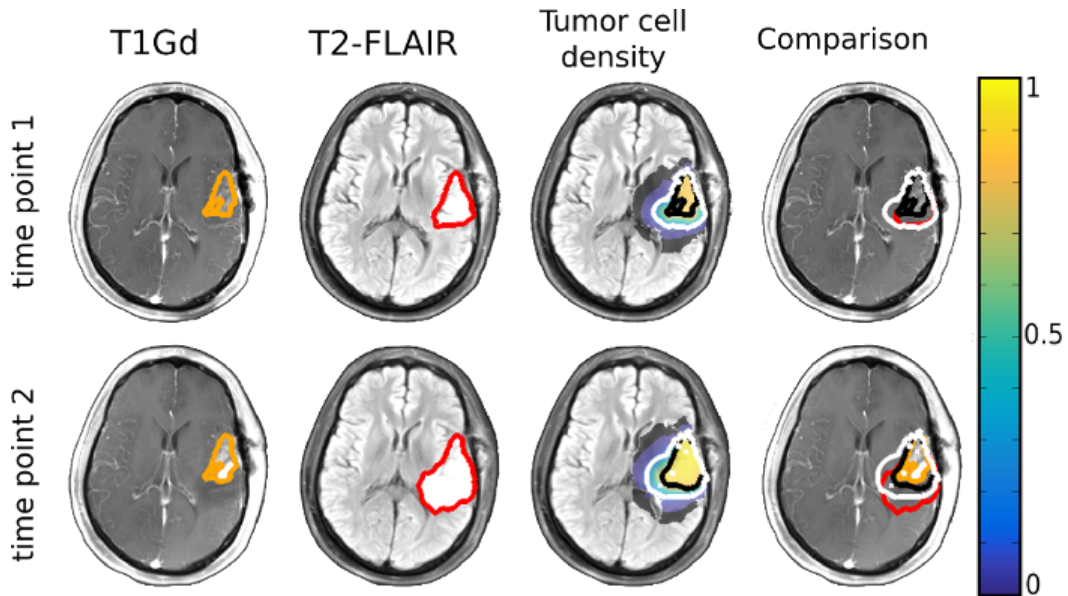


Figure 6.1: (Left) The proliferative rim is outlined in orange on the T1Gd MRI at two different time points; (Middle Left) The edema is outlined in red on the T2-FLAIR MRI at two different time points. The edema encloses the proliferative rim; (Middle Right) Tumor cell density computed with the reaction-diffusion model. The black (resp. white) line is the threshold values τ_1 (resp. τ_2) corresponding to the T1Gd (resp. T2-FLAIR) abnormality; (Right) Comparison between the clinician segmentation and the contours from the model.

6.1 Introduction

6.1.1 Motivations

The objectives of the mathematical modeling of brain tumor growth are four fold. First, it could help to better understand the mechanisms behind the disease progression. Second, the personalization of such models to specific patients could allow one to quantify the aggressiveness of the tumor, which has been shown to be correlated with clinically relevant information [Neal et al., 2013, Wang et al., 2009]. Third, personalized models could help predicting the future evolution of a given tumor. Fourth, personalized models could lead the way toward objective and more efficient personalized therapy. For instance, it has already been used in order to personalized radiotherapy plans [Corwin et al., 2013].

In this chapter, we present a method to estimate the posterior probability of the tumor growth model's parameters in order to estimate the correlation between the parameters of the model. Moreover, it gives valuable information on the confidence one has in the parameters, and the ability of the model to explain the data. The method is based on the Bayesian personalization of a tumor growth model. We specifically apply it to the personalization of glioblastoma growth using a reaction-diffusion model. We detail the results on one synthetic - but realistic - case, and 7

patients.

6.1.2 Clinical Background

Gliomas account for 30% of primary brain and central nervous system tumors. They are characterized by their infiltrative nature: malignant cells invade the tissue by progressing along the white matter fiber tracts. They can either be low grade or high grade, and very well localized or extremely diffused. We focus on grade IV gliomas called glioblastomas multiformes (GBM). They are the most common glioma - at least 50% of the recorded cases, and an incidence of 3.19 per 100,000 [Dolecek et al., 2012]. They grow extremely rapidly, extend to other parts of the brain, and are the most malignant primary brain tumor.

6.1.3 Modeling: Previous Work

The modeling of the tumor evolution can be done at different scales [Angelini et al., 2007]. On the microscopic scale, the model describes the evolution of individual cells based on division and invasion rules. On the macroscopic scale, the model describes the spatio-temporal evolution of the tumor cell density in the considered domain, based on partial differential equations. Over the last 20 years, particular attention has been given to the reaction-diffusion equation,

$$\frac{\partial u}{\partial t} = \underbrace{\nabla(D \cdot \nabla u)}_{\text{Diffusion}} + \underbrace{\rho u(1 - u)}_{\text{Logistic Proliferation}} \quad (6.1)$$

$$D \nabla u \cdot \vec{n}_{\partial \Omega} = 0 \quad (6.2)$$

$$\boldsymbol{\theta} = (D, \rho) \quad (6.3)$$

Equation (6.1) describes the spatio-temporal evolution of the tumor cell density u , which infiltrates neighboring tissues with a diffusion tensor D , and proliferates with a net proliferation rate ρ . Equation (6.2) enforces Neumann boundary conditions on the brain domain Ω , and $\boldsymbol{\theta}$ denotes the parameters of interest of the model.

In 1989, Murray *et al.* [Murray, 2002] pioneered on the use of mathematics applied to brain tumor growth, using the reaction-diffusion equation with an exponential growth. Assuming an isotropic diffusion in an infinite domain, he relates the velocity v of the tumor growth to the proliferation rate ρ and the diffusion coefficient D , $v = 2\sqrt{\rho D}$. This work has led the way to numerous other studies [Tracqui et al., 1995, Swanson et al., 2002, Chaplain, 1996].

Improving the computational efficiency of tumor growth models has been the topic of several studies. In 2010, Konukoglu *et al.* [Konukoglu et al., 2010b] introduced an approximation of the asymptotic solution of the reaction-diffusion equation based on an Eikonal equation, which can be solved with a Fast Marching algorithm, resulting in drastically reduced computation times. In 2012, Mosayebi *et*

al. [Mosayebi *et al.*, 2012] introduced a similar method to compute the tumor invasion in the brain parenchyma based on a geodesic distance computed from DTI information.

The mass effect applied by the tumor to the surrounding tissues has been modeled in 2005 by Clatz *et al.* [Clatz *et al.*, 2005]. They coupled the reaction-diffusion equation with a mechanical model, to take into account the mass effect, i.e. the displacement of adjacent brain tissue due to the growing tumor. They relate the diffusion tensor D to the Diffusion Tensor Images (DTI), thus forcing the tumor cells to preferably follow the white matter fiber tracts. In 2008, Hogeia *et al.* [Hogeia *et al.*, 2008] proposed another approach to include mass effect, using a reaction-diffusion-advection model coupled with a Eulerian mechanical framework.

Finally, research efforts recently targeted the development of more complex models. In 2011, Swanson *et al.* [Swanson *et al.*, 2011] developed a model dividing the tumor cells into sub-categories: the proliferative, the invasive and the hypoxic cells. This type of complex models has been further developed by Saut *et al.* [Saut *et al.*, 2014, Scribner *et al.*, 2014] in 2014, in which they developed a coupled PDE-based model to simulate the growth of high grade gliomas seeded in real images, and study the impact of different therapies [Raman *et al.*, 2016]. Finally, the models were extended to take into account the apparition of edema during the growth [Hawkins-Daarud *et al.*, 2013, Badoual *et al.*, 2014].

6.1.4 Personalization: Previous Work

It is of particular interest to solve the inverse problem of estimating the model's parameter $\theta = (D, \rho)$, which can describe a specific dynamic observed for a patient. As such, the modeling effort goes hand in hand with the personalization work. For personalization, most methods rely on comparing the model estimation with the abnormalities visible on Magnetic Resonance Images (MRIs) at two different time points.

A common approach to personalize reaction-diffusion equations is based on the observation that they admit wave-like solutions whose parameters can be related to the volume of the abnormalities observed on MRIs. In 2007, Harpold *et al.* [Harpold *et al.*, 2007] described the personalization of a glioma growth model using the reaction-diffusion equation with an exponential growth.

Another popular approach relies on solving the inverse problem using an optimization strategy. Hogeia *et al.* [Hogeia *et al.*, 2008] formulated a PDE-constrained optimization problem to estimate the parameters of the model based on image registration. Konukoglu *et al.* [Konukoglu *et al.*, 2010b] used the derivative-free optimization algorithm BOBYQA (for bounded optimization by quadratic approximation) [Powell, 2009] to minimize the distance between the tumor segmentations observed on the MRI, and the output of the model.

Finally, probabilistic approaches recently gained interest to solve complex inverse problems. Menze *et al.* [Menze *et al.*, 2011b] was among the first to propose a Bayesian formulation for brain tumor growth personalization, based on the ap-

proximation of the posterior using sparse grids. In 2012, Gooya *et al.* [Gooya *et al.*, 2012] proposed a method for the segmentation and registration of MRIs presenting glioblastoma based on the personalization of a reaction-diffusion-advection model using a single time point acquisition. It is interesting to note that Bayesian formulations have been used for a few years in the field of cardiac modeling [Konukoglu *et al.*, 2011, Neumann *et al.*, 2014]. However, the methods usually rely on approximations of the forward model using reduced order model, such as the polynomial chaos, to make the estimation of the posterior using Markov Chain Monte Carlo (MCMC) computationally tractable.

6.1.5 Contributions of the Chapter

In this chapter, we propose a Bayesian method for the personalization of a tumor growth model based on the reaction-diffusion equation. We propose the use of the Lattice Boltzmann Method (LBM) to implement the tumor growth model which results in reduced computation times. This is combined with a high acceptance rate Monte Carlo technique called the Gaussian Process Hamiltonian Monte Carlo (GPHMC). Contrary to previous approaches, our method does not rely on approximations of the forward model (resp. posterior probability) using reduced order models [Konukoglu *et al.*, 2011, Neumann *et al.*, 2014] (resp. sparse grid methods [Menze *et al.*, 2011b]). We compare our approach to two methods adapted from the literature. The former is based on the spherical asymptotic analysis of the forward model, and is based on the work of Swanson *et al.* [Harpold *et al.*, 2007, Corwin *et al.*, 2013]. The latter is based on the gradient-free optimization method BOBYQA, and is used in the work of Konukoglu *et al.* [Konukoglu *et al.*, 2010b].

6.2 Model

6.2.1 The Reaction-Diffusion Model

Because of the logistic reaction term, equation (6.1) does not have a closed form solution. However, in an infinite domain, with constant proliferation rate and diffusion coefficient, equation (6.1) admits solutions which asymptotically behave like traveling waves with speed $v = 2\sqrt{\rho D}$ [Konukoglu *et al.*, 2010b]. This solution has the asymptotic form $u(x, t) = u(x - vt) = u(\zeta)$. Plugging it into equation (6.1), we get the ordinary differential equation

$$\mathbf{n}' D \mathbf{n} \frac{d^2 u}{d\zeta^2} + v \frac{du}{d\zeta} + \rho u(1 - u) = 0 \quad (6.4)$$

where \mathbf{n} is the direction of motion in the infinite domain. Moreover, linearizing equation (6.4) for small $u \ll 1$, meaning that $u(1 - u) \sim u$, we get the second order linear equation

$$\mathbf{n}' D \mathbf{n} \frac{d^2 u}{d\zeta^2} + v \frac{du}{d\zeta} + \rho u = 0 \quad (6.5)$$

which admits solutions of the form $u(\zeta) = (A\zeta + B) \exp(-x/\lambda)$ with A, B two constants, and $\lambda = \sqrt{D/\rho}$. This equation shows that the parameter λ is of particular importance: it is related to the spatial decay of the tumor cell density, and it is referred to as the **invisibility index** [Corwin et al., 2013].

In the case of GBM growth modeling, it is clinically admitted that tumor cells have higher motility in white matter, compare to gray matter. Some work has been conducted to relate the diffusion tensor D to DTI - see [Stretton et al., 2013, Dittmann et al., 2013] for a detailed discussion. In this work, for simplification, we follow [Harpold et al., 2007], and define the diffusion tensor as $D = d_w \mathbb{I}$ in the white matter, and $D = d_w/10 \mathbb{I}$ in the gray matter, where \mathbb{I} is the 3x3 identity matrix, and d_w a scalar parametrizing the diffusion tensor. We further identify the parameter D with d_w . As such, the diffusion is heterogeneous and locally isotropic. This model reproduces the infiltrative nature of the GBM, takes into account anatomical barriers (ventricles, sulci, falx cerebri), and the tumor's preferential progression along white matter tracts such as the corpus callosum.

6.2.2 Model and MRIs

Data driven GBM growth modeling is based on the acquisition of different MRI modalities routinely acquired: T1 with Gadolinium contrast agent (T1Gd) and T2 Fluid-Attenuated Inversion Recovery (T2-FLAIR). They reveal different parts of the tumor: the active part, or proliferative rim can be observed on the T1Gd, while the T2-FLAIR reveals the disruption of the extracellular matrix, or edema. The T1Gd abnormality is usually included inside the larger T2-FLAIR abnormality (Figure 6.1). The personalization of the growth of the tumor is based on two consecutive time points, resulting in a total of four abnormalities segmented by the clinician.

We can immediately see one of the pitfalls of most models: the tumor cell density is not directly visible on T1Gd and T2-FLAIR MRIs. They rather reveal the impact of the tumor growth on the brain. In order to relate the tumor cell density u - solutions of (6.1) - to the MRIs, the frontier of the visible abnormalities is assumed to correspond to a threshold value of the tumor cell density u . We note τ_1 the value of the tumor cell density u corresponding to the frontier of the T1Gd abnormality, and τ_2 the value corresponding to the frontier of the T2-FLAIR abnormality. We can already note that the invisibility index defined in the previous section is related to the distance between the boundaries of the T1Gd abnormality and the T2-FLAIR abnormality: the larger the distance, the larger the invisibility index is.

6.3 Simulation

6.3.1 Preprocessing of the data

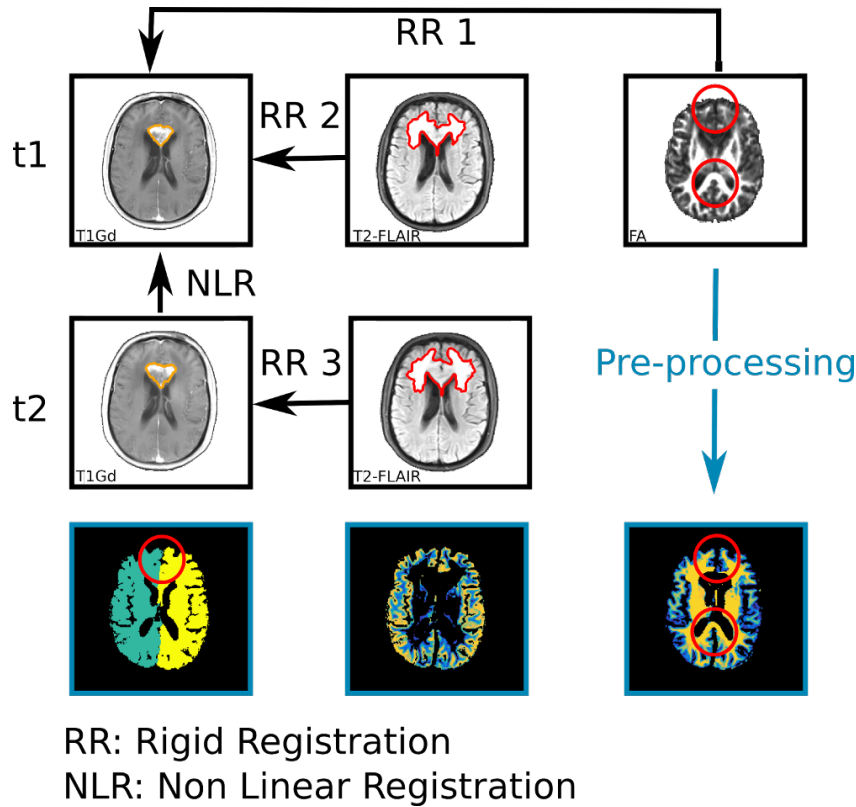


Figure 6.2: First row: Registration pipeline at time t_1 of the T1Gd, T2-FLAIR, and FA. Middle row: Registration pipeline at time t_2 of the T1Gd, and T2-FLAIR. Bottom row, from left to right: segmentation of the left and right hemispheres to ensure the falx cerebri is labeled as CSF; gray matter segmentation; white matter segmentation.

The pre-processing of the MRIs is of particular importance (Figure 6.2). The T1Gd and T2-FLAIR abnormalities were segmented by a clinician, and the fractional anisotropy (FA) MRI was extracted from the DTI. First, the segmentations of the second time point t_2 are mapped on the space of the first time point t_1 as follows. i) For each visit, the T2-FLAIR and FA MRIs are rigidly registered to the T1Gd MRI [Jenkinson et al., 2002]. ii) The T1Gd MRI at t_2 is non-linearly registered to the T1Gd MRI at t_1 using the FNIRT function of the FSL software [Andersson et al., 2007, Jenkinson et al., 2012]. The segmentation of the tumor at t_2 is used to exclude the tumor from the similarity criterion (sum-of-squared difference) during the registration. As such, the intensity values in the tumor are ignored, and the tumor is warped in accordance with the surrounding (non-masked) tissues. iii) The resulting transformations are applied to transport the T2-FLAIR abnormalities at

t_1 and t_2 , and the T1Gd abnormality at t_2 , on the T1Gd MRI at t_1 . Second, white and gray matter, and cerebrospinal fluid (CSF) are extracted from MRIs at t_1 . The pipeline is the following i) Extract the brain from the skull [Iglesias et al., 2011]. ii) Correct for the bias and segment the white matter, gray matter, and CSF [Zhang et al., 2001]. iii) Separate the left and right hemispheres [Zhao et al., 2010], iv) The voxels at the boundary between the two hemispheres are tagged as CSF, in order to prevent the tumor from invading the contra-lateral hemisphere through the falx cerebri. The voxels with high FA value (> 0.45) and which were tagged as white matter are not affected by this process in order to ensure that the corpus callosum stays segmented as white matter. The red circle on Figure 6.2 emphasizes the importance of the hemisphere separation to label the falx cerebri as CSF, and the corpus callosum as white matter.

6.3.2 Lattice Boltzmann Method

A typical approach to implement the reaction-diffusion equation is to discretize the equation using the Crank-Nicolson scheme [Özügürü, 2015]. This requires the inversion of a large sparse matrix $n \times n$ where n is the number of voxels in the image, using a preconditioned gradient method like the biconjugate gradient stabilized method. For 3D MRIs with $n \sim 10^6$, this approach is computationally prohibitive. For our approach, we use the more recent explicit method called the Lattice Boltzmann Method (LBM). LBM has been successfully applied to implement the reaction-diffusion equation in the fields of cardiac electrophysiology modeling [Rapaka et al., 2012, Neumann et al., 2014], and liver tumor radiofrequency-ablation [Audigier et al., 2015]. The idea is to model the reaction-diffusion equation as a set of fictitious particles which collide and stream on the cartesian grid. The details of the implementation can be found in Appendix B.

With a diffusion coefficient constant in time, the LBM does not require costly inversion of matrices. The LBM is easily parallelized such that simulating 30 days of growth, with $\delta t = 0.1$ day, takes approximately 50 seconds on a 2.3 Ghz 50 core machine for a 1 mm isotropic $155 \times 182 \times 157$ grid.

6.3.3 Initialization

The initialization of the tumor cell density $u(t = t_1, x)$ at the time of the first acquisition is of particular importance, as it impacts the rest of the simulation. In this work, the tumor tail extrapolation algorithm described in [Konukoglu et al., 2010a] is used. The tumor cell density is computed outward (and inward) of the T1Gd abnormality borders as a static approximation of the wave-like solution of equation (6.1) with parameter θ . The algorithm is based on the recursive approximation of equation (6.4) for current values of the solution u . It only depends on the invisibility index $\lambda = \sqrt{D/\rho}$. The details of the implementation can be found in [Konukoglu et al., 2010a]. By construction of the initialization, the T1Gd abnormality falls exactly on the threshold τ_1 of the tumor cell density at the first time point (Figure

6.1).

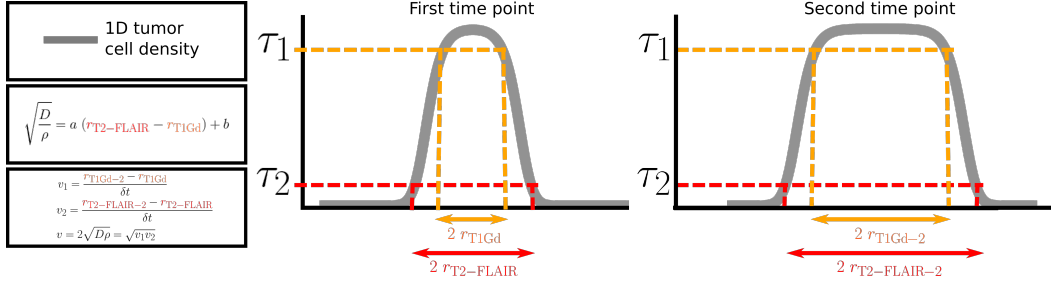


Figure 6.3: 1D graphical explanation detailing how the measured radii are related to the invisibility index and speed of growth of the tumor. (Left) Relationship between the invisibility index and the speed of the tumor, and the parameters D and ρ of the model. (Right) 1D tumor cell density at two different time points detailing how the measured radii are related to the parameters of the model.

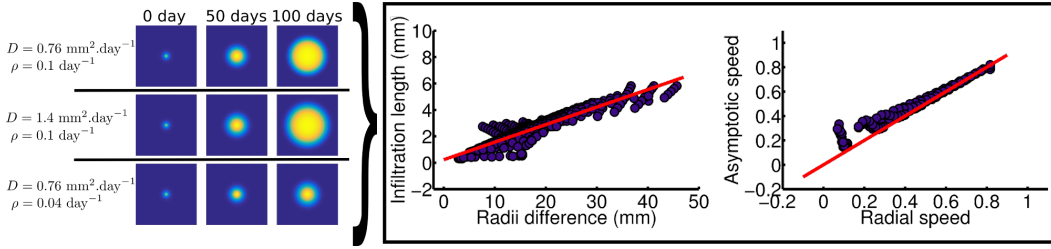


Figure 6.4: (Left) Example of simulations on a large cube with different parameters D and ρ used to infer the relationship between the invisibility index and the measured radii. (Middle) Invisibility index ($\sqrt{D/\rho}$) function of $r_{T2-FLAIR} - r_{T1Gd}$. The blue dots result from the LBM simulations in the square, the red line is the linear fit. (Right) Asymptotic speed ($2\sqrt{D\rho}$) function of the measured radial growth speed. The blue dots result from the LBM simulations, the red line is the first bisector.

6.4 Personalization

We describe in this section the personalization of the parameter $\theta = (D, \rho)$ of the reaction-diffusion equation (6.1). Three different methods with increasing levels of complexity are presented. The first two are adapted from the literature, and are compared to the last one which we propose for the Bayesian personalization.

The first method (Section 6.4.1) is based on Swanson’s approach [Harpold et al., 2007, Corwin et al., 2013]. The spherical asymptotic analysis of the solution in a large domain is used to relate the invisibility index to the measured radii of the T1Gd and T2-FLAIR abnormalities, using multiple runs of the forward model.

The second method (Section 6.4.2) is based on [Konukoglu et al., 2010b] where the derivative-free optimization method BOBYQA is used to infer the parameters D and ρ . We apply it to the case of glioblastoma where two abnormalities are

observable at each time point. We do not optimize for the source point of the tumor since we initialize the model with the contour of the first T1Gd abnormality.

Finally, we propose to estimate the posterior probability of the parameters D and ρ , knowing the clinician segmentations, using a MCMC method, the Gaussian Process Hamiltonian Monte Carlo.

6.4.1 Spherical Asymptotic Analysis

The parameters D and ρ can be related to the asymptotic velocity $v = 2\sqrt{D\rho}$, and the invisibility index $\lambda = \sqrt{D/\rho}$. The knowledge of the velocity and invisibility index uniquely identifies D and ρ since $D = v\lambda/2$ and $\rho = v/(2\lambda)$. As such, given a patient and the segmented T1Gd and T2-FLAIR abnormalities, we want to infer the parameters (v, λ) from the measured radius of the abnormality through their measured volume. We hypothesize that there is a simple relationship between those radii, and the velocity and the invisibility index [Harpold et al., 2007]. We consider the special case of an isotropic and homogeneous domain with a Gaussian initialization. The speed of growth can be measured as the temporal variation of the radial expansion of the abnormalities over time (see Figure 6.3 left). Since the distinct speed of growth of the T1Gd and T2-FLAIR abnormalities can be measured (and can be different), we use the geometric mean between the two, $v = \sqrt{v_1 v_2}$, as an estimate. We propose in this section to find a simple relationship between the invisibility index, and the measured radii of the T1Gd and T2-FLAIR abnormalities (see Figure 6.3).

The tumor growth model was run on a large $201 \times 201 \times 201$ 1 mm isotropic grid, with different parameters D and ρ , for 200 days, and initialized with a symmetric Gaussian. Using 15 equally spaced values of $D \in [0.02 \text{ } 1.5] \text{ mm}^2.\text{day}^{-1}$, and 15 equally spaced values of $\rho \in [0.002 \text{ } 0.2] \text{ day}^{-1}$, 225 simulations were performed, keeping 11 time points per simulations. For each time point, we considered the value of the radii of the T1Gd and T2-FLAIR abnormality (resp. $r_{\text{T2-FLAIR}}$ and r_{T1Gd}), using thresholds of $\tau_1 = 80\%$ and $\tau_2 = 16\%$. We observe a good linear relationship between the invisibility index λ , and the radius difference ($r_{\text{T2-FLAIR}} - r_{\text{T1Gd}}$) (Figure 6.4),

$$\lambda = \sqrt{\frac{D}{\rho}} = a (r_{\text{T2-FLAIR}} - r_{\text{T1Gd}}) + b \quad (6.6)$$

with $a = 0.13$ and $b = 0.23 \text{ mm}$ for D in $\text{mm}^2.\text{day}^{-1}$ and ρ in day^{-1} . We further checked that the measured velocity corresponded to the asymptotic one (Figure 6.4).

In this chapter, we consider the personalization using two time points. Since the invisibility index can be measured on both time points, similarly to the speed, we use the geometric mean between the two as an estimate. This personalization is based on volumetric consideration, and valid in large homogeneous domain, much like Swanson's approach [Harpold et al., 2007, Corwin et al., 2013].

6.4.2 BOBYQA Optimization

The previous method does not take into account the inhomogeneity and anisotropy of the growth, and does not account for anatomical barriers such as CSF. In order to derive a finer estimation, we use an optimization method. We need to define the error corresponding to a simulation with associated parameter θ . The simulation is initialized at t_1 using the first T1Gd abnormality, and simulated with the LBM until the second time point t_2 is reached. We extract the simulated contours corresponding to the thresholds τ_1 and τ_2 , at t_1 and t_2 . The 95th percentile of the symmetric Hausdorff distance between the borders of the clinician segmentation and the extracted contours is computed for: i) the T2-FLAIR abnormality at time t_1 , ii) the T2-FLAIR abnormality at time t_2 , iii) the T1Gd abnormality at time t_2 . The mean of these distances H_{mean} is used as an error measure for the simulation. We use this error measure because the Hausdorff distance is sensitive and independent of the size of the abnormality. As such, the T1Gd and T2-FLAIR will be penalized in a similar fashion. Other error measures could be considered such as the DICE coefficient, which is however sensitive to the size of the abnormalities. We minimize the error using the derivative-free optimization algorithm BOBYQA [Powell, 2009], using the implementation of the library NLOpt¹. The algorithm is run 9 times with 9 different initializations to explore various local minima. We keep the best of the 9 solutions. This personalization is in the spirit of Konukoglu’s work [Konukoglu et al., 2010b], but applied to glioblastomas.

6.4.3 Bayesian Personalization

We denote by S the set of clinician segmentations the model should fit. We are interested in the posterior probability of the model parameter $\theta = (D, \rho)$, knowing the observations S . To cast the problem in a probabilistic framework, we follow Bayes rule: $P(\theta|S) \propto P(S|\theta) P(\theta)$. The likelihood is modeled as $P(S|\theta) \propto \exp(-H_{\text{mean}}^2/\sigma^2)$, where the distance H_{mean} is the mean of the 95th percentile symmetric Hausdorff distance between the border of the segmentations S and the isolines of the simulated tumor cell density u using θ , and the thresholds τ_1 and τ_2 . As such, the negative log-likelihood $H_{\text{mean}}^2/\sigma^2$ is the error term optimized during BOBYQA, normalized with the noise level σ . $P(\theta)$ is the prior on the parameters of the model. We want to estimate the posterior distribution $P(\theta|S)$. To do so, samples are drawn from the posterior probability using the Gaussian Process Hamiltonian Monte Carlo [Rasmussen, 2003].

Hamiltonian Monte Carlo (HMC). HMC is a Markov Chain Monte Carlo algorithm which uses a refined proposal density function based on the Hamiltonian dynamics [Neal et al., 2011]. The idea is to have a high acceptance rate while proposing points relatively far from the current point. The problem is augmented with a momentum variable $\mathbf{p} \sim \mathcal{N}(\mathbf{0}, \mathbb{I})$. By randomly sampling \mathbf{p} , we define a current state (θ, \mathbf{p}) . The energy of the state is $H(\theta, \mathbf{p}) = E_{\text{pot}} + E_{\text{kin}}$, with potential

¹Steven G. Johnson, The NLOpt nonlinear-optimization package, <http://ab-initio.mit.edu/nlopt>

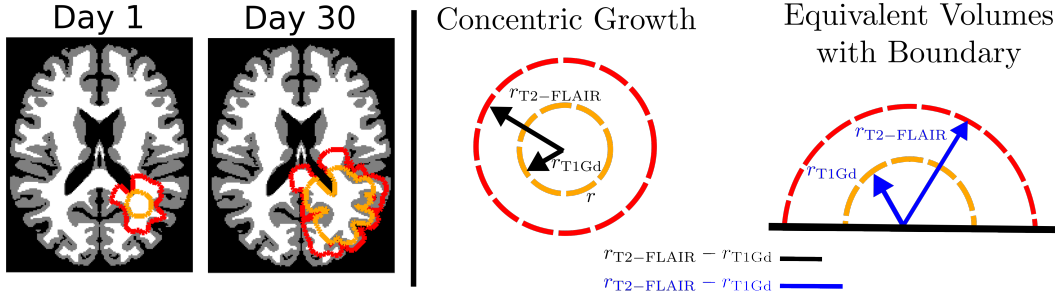


Figure 6.5: (Left) Synthetic growth of a tumor in the MNI atlas during 30 days with $D = 1 \text{ mm}^2 \cdot \text{day}^{-1}$ and $\rho = 0.18 \text{ day}^{-1}$. The T2-FLAIR abnormality (isodensity of $\tau_2 = 16\%$) is outlined in red. The T1Gd abnormality (isodensity of $\tau_1 = 80\%$) is outlined in orange. (Right) Limits of the asymptotic personalization in presence of boundaries. The infiltration length - proportional to $r_{\text{T2-FLAIR}} - r_{\text{T1Gd}}$ - tends to be under-estimated by considering the equivalent spherical volumes.

energy $E_{\text{pot}} = -\log(P(S|\theta)P(\theta))$, and kinetic energy $E_{\text{kin}} = 1/2 \|\mathbf{p}\|_2^2$. Using the Hamiltonian dynamics for a certain period of time Δt_H ,

$$\frac{d\theta_i}{dt} = \frac{\partial H}{\partial \mathbf{p}_i}, \quad \frac{d\mathbf{p}_i}{dt} = -\frac{\partial H}{\partial \theta_i} \quad (6.7)$$

a new state (θ^*, \mathbf{p}^*) is proposed, with energy $H(\theta^*, \mathbf{p}^*)$. Using a Metropolis-Hastings acceptance criterion, the new state (θ^*, \mathbf{p}^*) is accepted with probability $\mathcal{A} = \min[1, \exp(-H(\theta^*, \mathbf{p}^*) + H(\theta, \mathbf{p}))]$. The conservation of the energy during the Hamiltonian dynamics - up to the numerical discretization accuracy of the Leapfrog scheme - insures a high acceptance rate \mathcal{A} , which is the ratio of proposed samples which are accepted. The boundary conditions on the bounded parameter space θ are enforced using a bounce back condition [Betancourt, 2010] during the Leapfrog scheme used for the time integration. More precisely, if during the computations, the parameter θ crosses a boundary, its moment \mathbf{p} is reversed and projected on the normal of the boundary.

Gaussian Process Hamiltonian Monte Carlo (GPHMC). In the HMC, computing the Hamiltonian dynamics - equations (6.7) - requires a significant amount of model evaluations. To circumvent this difficulty, E_{pot} is approximated with a Gaussian process [Rasmussen, 2003]. During the initialization phase, the forward model is evaluated on a coarse grid to initialize the Gaussian process. During the exploration phase, the forward model is evaluated at locations of low E_{pot} and high uncertainty on the Gaussian process interpolation (details can be found in [Rasmussen, 2003]). HMC is then run using the Gaussian process interpolation of E_{pot} to compute the Hamiltonian dynamics. Given that the Gaussian process well captures E_{pot} , the GPHMC benefits from the high acceptance rate of the HMC, with far less model evaluations.

Parameters. The parameter θ is constrained such that $D \in [10^{-4}, 10] \text{ mm}^2/\text{days}$, and $\rho \in [10^{-5}, 10] \text{ days}^{-1}$, which encloses expected values for

glioblastomas [Harpold et al., 2007]. The prior $P(\boldsymbol{\theta})$ is assumed log-uniform within this bounded box. The Hamiltonian dynamics is run for $\Delta t_H = 60$ days. For the likelihood, the noise level σ has been empirically set to 5 mm to provide a reasonable acceptance rate, and a good acceptance rate. The noise level influences how peaked the estimated posterior will be. For the GPHMC, the Gaussian process is defined with a squared exponential covariance matrix $C(\boldsymbol{\theta}_1, \boldsymbol{\theta}_2) = w_0 \exp(-\|\boldsymbol{\theta}_1 - \boldsymbol{\theta}_2\|_2^2/w_1^2)$ [Williams and Rasmussen, 2006], where $\|\cdot\|_2$ is the l_2 norm. These parameters are estimated with maximum likelihood [Williams and Rasmussen, 2006]. During the GPHMC, the initialization is done with 49 forward model evaluations, while 50 evaluations are used for the exploratory phase, then 1000 samples are generated.

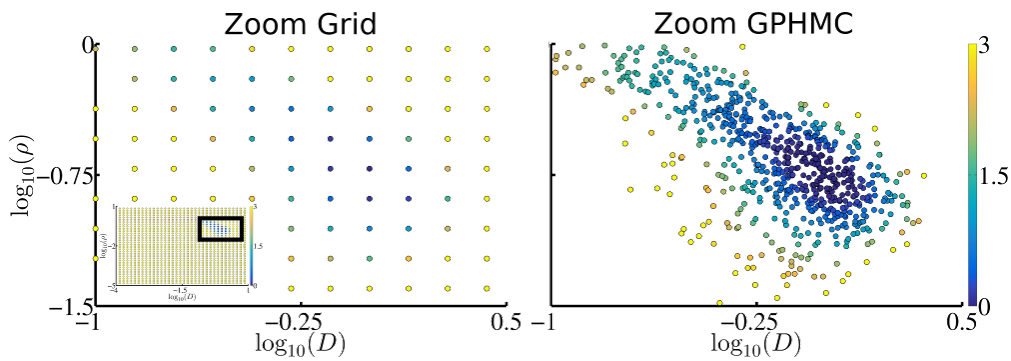


Figure 6.6: Comparison with a simple grid estimation of the posterior using $34 \times 34 = 1156$ model evaluations in the admissible domain for the synthetic case. The zoom to the region of low potential energy (i.e. high probability) proves the value of the presented method. The color scale indicates the negative log-likelihood.

6.5 Results

6.5.1 Synthetic Case

We perform a thorough analysis of a synthetic - but realistic - case. A simulation is run on the MNI atlas [Mazziotta et al., 2001], with parameters $D = 1 \text{ mm}^2 \cdot \text{day}^{-1}$ and $\rho = 0.18 \text{ day}^{-1}$, for 30 days (Figure 6.5). The result of the 3 different personalization methods can be seen on Figure 6.7. The result of the BOBYQA optimization is close to the mode of the computed posterior density. However, the spherical asymptotic analysis personalization is largely under-estimating the diffusion parameter D . The asymptotic personalization method makes the assumption that the T1Gd and T2-FLAIR abnormalities are growing concentrically in an infinite domain. The presence of boundaries in realistic growth leads to the under-estimation of the difference of the radius of the abnormalities, leading to the under-estimation of the infiltration length (Figure 6.5). The acceptance rate during the GPHMC is 83%, reflecting the fact that the Gaussian process is a good interpolation of the potential energy E_{pot} for the sampling.

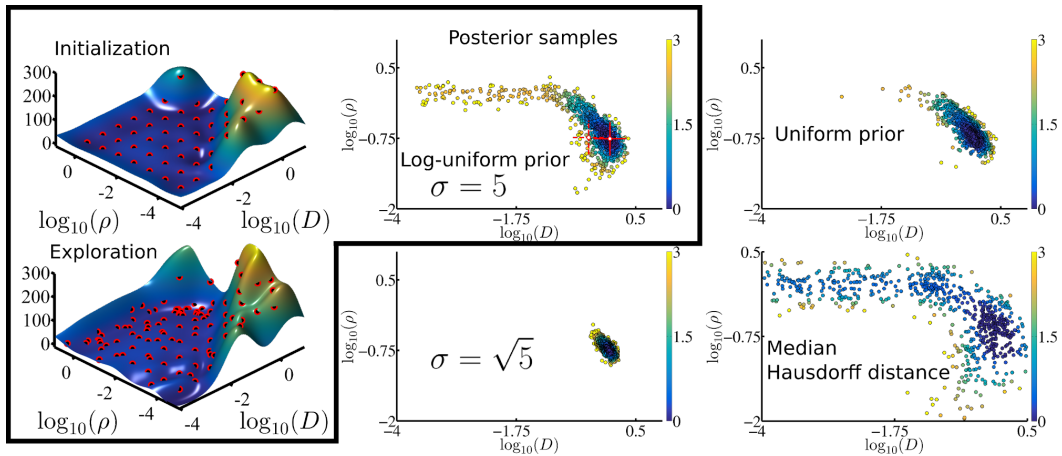


Figure 6.7: In the black box, (Left) i) Initialization of the Gaussian process interpolating the potential energy E_{pot} with a coarse 7×7 grid ii) Refinement of the Gaussian process with points of low potential energy and high uncertainty (see details in [Rasmussen, 2003]) (Right) Personalization of the tumor growth model for the synthetic case. The result of the asymptotic personalization is at the intersection of the dashed red lines, the result of the BOBYQA optimization is at the intersection of the full red lines, and falls on the true parameters values at this scale. The color scale indicates the negative log-likelihood. Outside of the black box, results of the GPHMC personalization for the synthetic case using (from left to right, top to bottom) a uniform prior, a noise level $\sigma = \sqrt{5}$, and the median Hausdorff distance.

The impact of the different parameters is analyzed on the synthetic case (Figure 6.7). We can see that using a uniform prior - like in [Lê et al., 2015a] - results in samples which are more concentrated in the regions of high values of D and ρ . However, it does not change much the shape and the location of the mode. On the other hand, using a noise level $\sigma = \sqrt{5}$ mm instead of 5 mm (with a log-uniform prior) results in a posterior which is much more peaked around the same mode. Finally, using the median Hausdorff distance instead of the 95th percentile (with a log-uniform prior and $\sigma = 5$ mm) results in samples which are more spread because this distance is less discriminative. The effect is very similar to increasing the noise level σ . Finally, the method is compared to a simple grid evaluation of the potential energy for the synthetic case. The GPHMC automatically sample an extremely high density of points in the region of high probability, compared to the simplest grid approach (Figure 6.6).

6.5.2 Glioblastoma Patients

The method is applied to 7 patients. The T1Gd and T2-FLAIR abnormalities were segmented by a clinician. A summary of the results can be found on Table 6.1. The patients come from diverse clinical studies. We selected patients who were not treated with resection, and where two time points with visible growth were available. The patients were under chemotherapy, radiotherapy, and other specific

type of therapies such as anti-angiogenic drug. This is one of the reasons why we focus on personalization, and not on prediction. The complex therapy schedule makes the prediction of the future behavior of the tumor difficult.

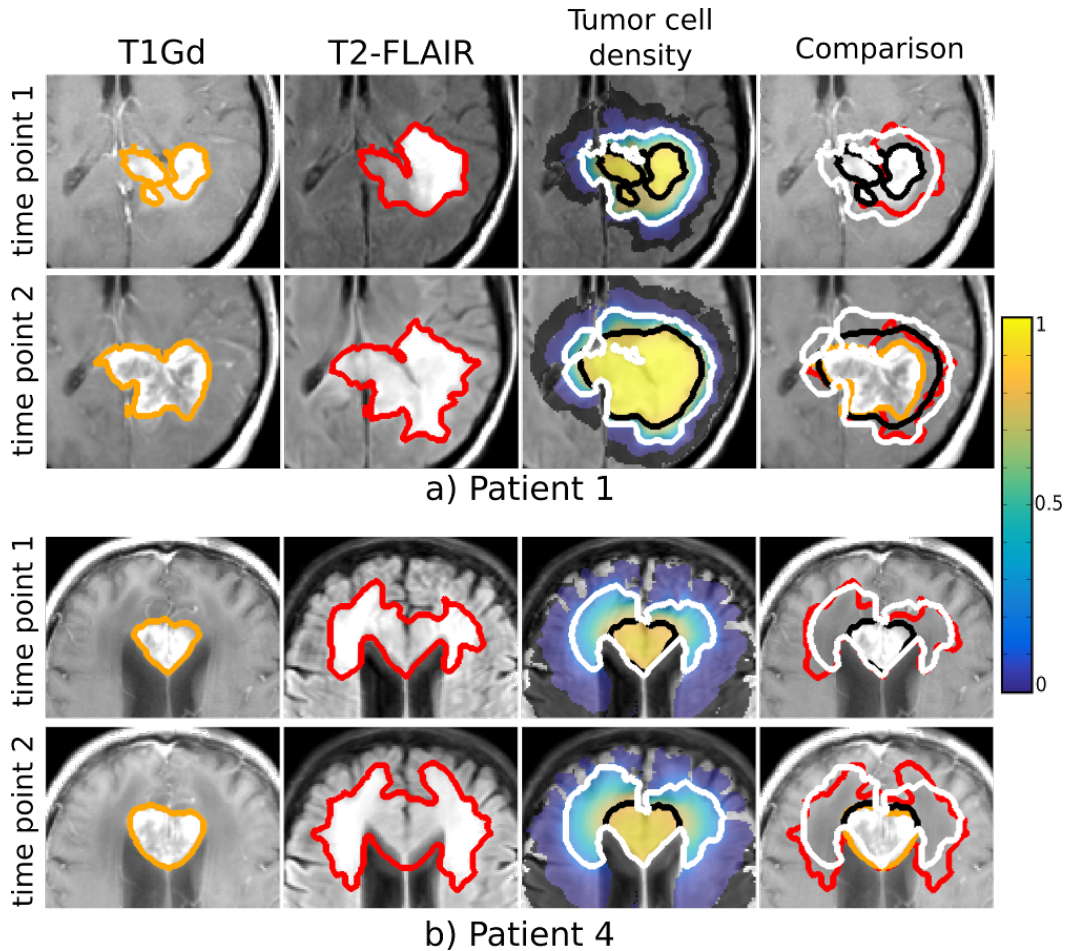


Figure 6.8: Maximum a Posteriori fit for Patient 1 (Top) and Patient 4 (Bottom). For each patient: (Left) The proliferative rim is outlined in orange on the T1Gd MRI at two different time points; (Middle Left) The edema is outlined in red on the T2-FLAIR MRI at two different time points; (Middle Right) Tumor cell density, the black (resp. white) line is the threshold value τ_1 (resp. τ_2) corresponding to the T1Gd (resp. T2-FLAIR) abnormality; (Right) Comparison between the clinician segmentation and the contours from the model.

The result of the estimation can be seen on Figure 6.9. The personalization based on the asymptotic analysis tends to provide low values of D and ρ . We observe the variety of behavior of the posterior for the different patients. Figure 6.9 shows the best BOBYQA solution. The second and third best solutions are only shown if they are distinguishable with the first one at this scale, or if they fall in regions of low potential energy. The best BOBYQA solution always falls close to a mode of

the posterior, but does not reflect the correlation between the parameters D and ρ . Moreover, it is worth mentioning that for every patient, some of the differently initialized BOBYQA solutions lead to very poor results.

Patients 1, 2, and 3 present only one mode. The BOBYQA solution gives good results, while the asymptotic analysis always gives slightly off solutions. Patients 3, 6, and 7 present two modes. The two modes are very close to each other for patients 6 and 7 while they are far apart for patient 3. This reflects the fact that the model cannot explain simultaneously the four available segmentations, and different sets of parameters lead to equivalently plausible solutions. For patient 5, the BOBYQA solution and spherical asymptotic analysis give completely false result. This seem to be due to the fact that the solutions lie near the boundary of the domain, which lead to false convergence of the BOBYQA algorithm. For this patient, the parameters tend to lie at the edge of the admissible domain defined in Section 6.4.3.

The acceptance rate during the GPHMC is on average 72%. This high acceptance rate is an indication that the Gaussian process is a good interpolation of the potential energy. However, for some patients, the interpolation is not as good resulting in acceptance rate of 52% (Patient 3) and 56% (Patient 7). This is mainly due to narrow regions of high probability, where there are relatively few points to interpolate the potential energy. Note that the parameters of the GPHMC were the same for the seven different patients.

For a given patient, we can gather the samples in a matrix $\mathbf{X} \in \mathbb{R}^{n \times 2}$, where n is the number of samples. We can project the samples in the $(\log(\lambda), \log(v))$ space, and compute the empirical covariance C ,

$$C = \text{cov} \left(X \begin{pmatrix} \frac{1}{2} & \frac{1}{2} \\ -\frac{1}{2} & \frac{1}{2} \end{pmatrix} \right) \quad (6.8)$$

We then compute the normalized variances σ_{inv} and σ_{speed} of the posterior samples along the speed and invisibility index axis respectively,

$$\sigma_{\text{inv}} = \frac{C(1,1)}{\text{Tr}[C]}, \quad \sigma_{\text{speed}} = \frac{C(2,2)}{\text{Tr}[C]} \quad (6.9)$$

where $\text{Tr}[\cdot]$ refers to the trace of the matrix. This way, we can quantify which of the invisibility index or speed is better captured by the model. For instance, patient 3 presents an extremely elongated posterior along the line of constant invisibility index ($\sigma_{\text{inv}} = 1\%$, $\sigma_{\text{speed}} = 99\%$), showing that the uncertainty on the fit is due to the speed rather than the invisibility index. For patient 1, the posterior is not as elongated, showing that the uncertainties due to the speed or the invisibility index are more similar ($\sigma_{\text{inv}} = 45\%$, $\sigma_{\text{speed}} = 55\%$). This is probably caused by the fact that the two time points are 105 days apart for patient 1. As such the speed of growth of the tumor is more identifiable resulting in a drop of the variance due to the speed compared to the other patients. Similarly, the synthetic case presents a larger growth which makes the identifiability of the speed easier.

We show the result of the simulation using the parameter θ corresponding to the Maximum a Posteriori (MAP) of the samples (Figure 6.8) for two representa-

	$t_2 - t_1$ (days)	Acceptance rate (%)	σ_{speed} (%)	σ_{inv} (%)
Synthetic	30	83	23	77
Pat. 1	105	84	45	55
Pat. 2	29	87	74	26
Pat. 3	26	52	99	1
Pat. 4	31	72	98	2
Pat. 5	14	77	98	2
Pat. 6	28	74	82	18
Pat. 7	29	56	83	17

Table 6.1: Results on 7 patients: time span between the time points; acceptance rate of the GPHMC; percentage of variance due to the speed; percentage of variance due to the invisibility index.

tive patients. Furthermore, for each sample resulting from the GPHMC, one can compute the corresponding segmentation for the T1Gd at the second time point, and the T2-FLAIR at the first and second time points. We can then compute the probability for each voxel to lie within one of those segmentations. We show on Figure 6.10 the 10% (in blue) and 90% (in green) isolines of this probability mask which allows to visualize the uncertainty in the MAP segmentation.

6.6 Discussion

In this work, we presented an efficient implementation of the reaction-diffusion equation for the brain tumor growth based on the Lattice Boltzmann Method. We further presented estimation methods of the model’s parameters of different levels of complexity. The simplest one is based on the asymptotic properties of the reaction-diffusion equation. It does not require complex computations, but fails when the growth is constrained by the brain boundaries. The second method is the optimization of an error term using a derivative-free algorithm. In our experiments, the method required on average 20 model evaluations per initialization, resulting in 180 model evaluation for a total of 9 different initializations. The third method is based on an efficient Monte Carlo method called the Gaussian Process Hamiltonian Monte Carlo, used to sample from a posterior, derived as the Boltzmann distribution of the previous error term. It requires a total of 1100 model evaluations. As such, the estimation of the posterior probability requires only 6 times more evaluations than the direct optimization, and provides additional valuable informations about the shape of the posterior. This reveals the possible presence of several modes, and the correlation between the parameters due to the lack of identifiability of the speed or the invisibility index.

Moreover, the samples of the posterior density could be used to estimate the density in the whole domain using for instance kernel density estimation [Lê et al., 2015a]. This could be helpful to have access to other useful statistical indices such

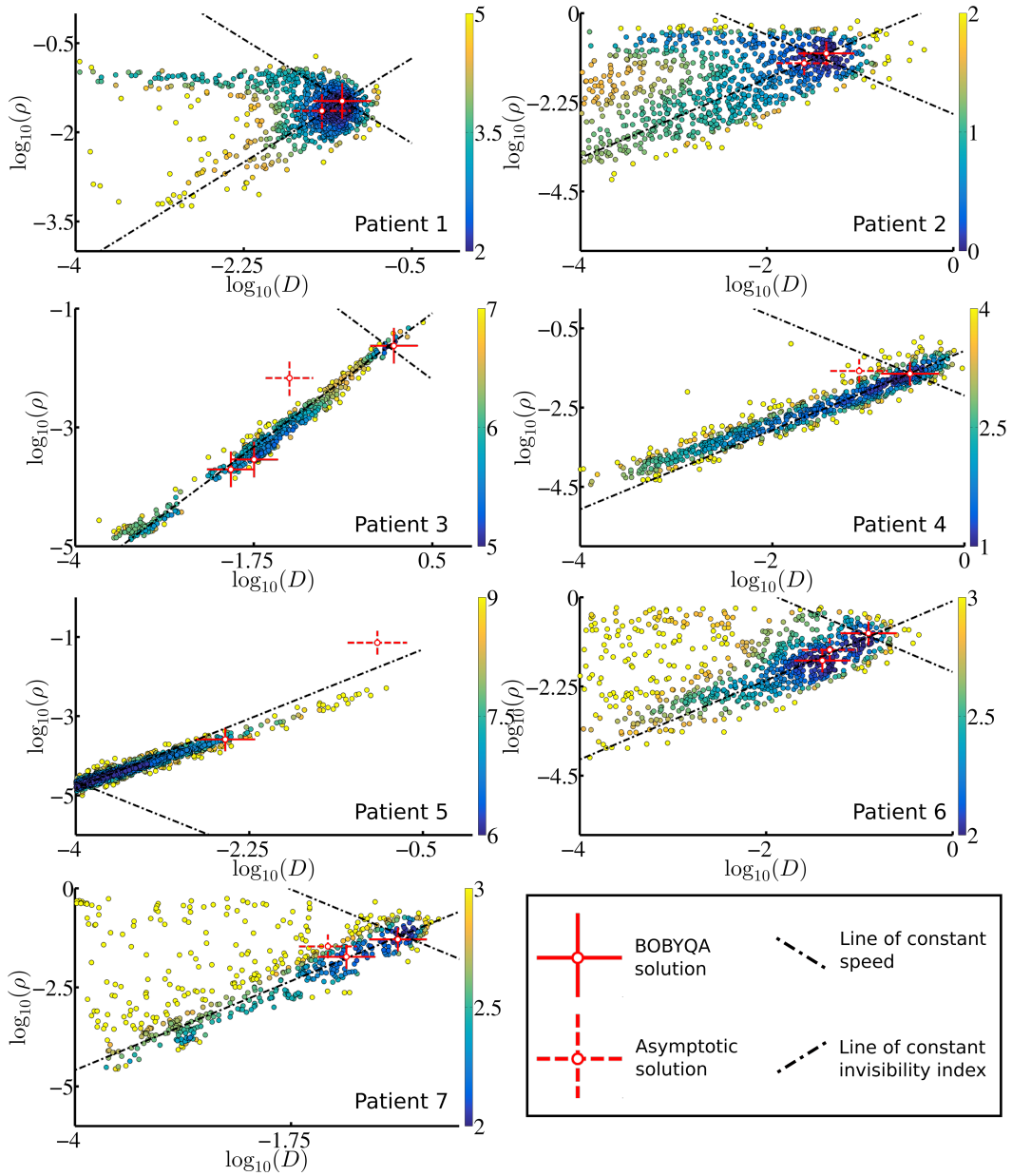


Figure 6.9: Personalization of the tumor growth model for the 7 patients. The result of the asymptotic personalization is at the intersection of the dashed red lines, the result of the BOBYQA optimization is at the intersection of the solid red lines. The presence of several BOBYQA solutions from different initializations is indicated when the best three solutions were noticeably distinct. The color scale indicates the negative log-likelihood of the posterior $P(\theta|S)$, which is equal to the potential energy E_{pot} .

as the evidence of the model, which can help answer questions about model selection [Oden et al., 2013, Lê et al., 2015a].

In the future, we could consider the thresholds τ_1 and τ_2 as parameters of the model to be sampled. This could also be the case for the noise level σ . Moreover, the modeling of the mass effect could be useful in order to avoid the non-linear registration between the second and the first time points.

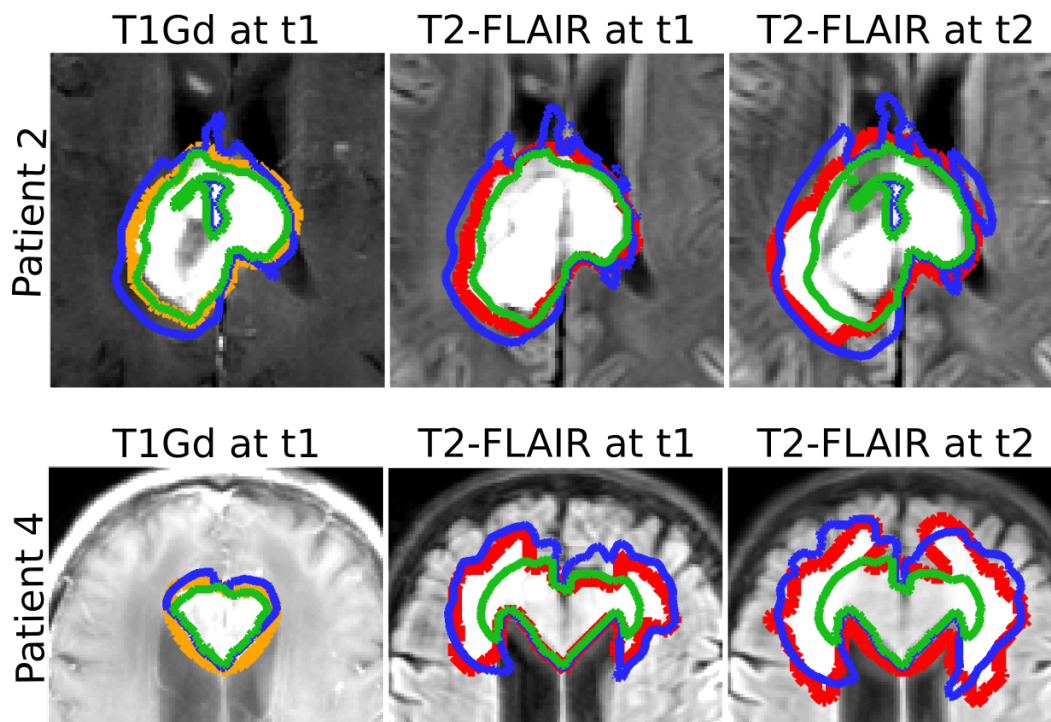


Figure 6.10: (Top) Patient 2 (Bottom) Patient 4. From left to right: T1Gd for the second time point, T2-FLAIR for the first time point, T2-FLAIR for the second time point. The clinician segmentation are in orange for the T1Gd and red for the T2-FLAIR. The blue outline (resp. green) encloses the voxels which were present in at least 10% (resp. 90%) of the segmentations deduced from the samples.

6.7 Perspectives

In the future, we intend to apply the Bayesian personalization in order to explicitly take into account the uncertainty in the expert's segmentation. More specifically, the segmentations used during each model evaluation could be sampled in the space of plausible segmentations [Lê et al., 2015b]. We also believe that this work could be used the objective planning of personalized and more efficient therapy. Some work has already been done on relating tumor growth models to radiation response models to better define radiotherapy plans [Unkelbach et al., 2014b, Unkelbach et al., 2014a, Rockne et al., 2009]. Such a method could provide personalized therapy plans taking into account the uncertainty in the model's parameters.

Personalized Radiotherapy Planning Based on a Computational Tumor Growth Model

Contents

7.1	Introduction	83
7.2	Segmentation Samples	84
7.3	Tumor Growth Model	86
7.4	Personalization	86
7.4.1	Scenario 1: One time point only	87
7.4.2	Scenario 2: Two time points	87
7.4.3	Scenario 3: Two time points and segmentation uncertainty	87
7.5	Radiotherapy Planning	88
7.5.1	Cell survival	88
7.5.2	Prescription Dose Optimization	89
7.5.3	IMRT Planning	90
7.6	Results	92
7.7	Second Patient	102
7.8	Conclusion	109

Based On: a journal paper submitted to IEEE Transactions on Medical Imaging.

In this chapter, we combine a computational model of brain tumor growth with a dose response model to optimize radiotherapy planning. The Bayesian personalization of the growth model to patients' magnetic resonance images (MRIs) takes into account the uncertainty in the model parameters, together with the uncertainty in the segmentations of the tumor on the different MRI modalities. We present and compare three different scenarios. In the first one, we only consider one MRI acquisition before therapy, as it would usually be the case in clinic. In the second one, we use two time points in order to personalize the model and plan radiotherapy. In the third one, we include the uncertainty in the segmentation process. Based on those different scenarios, we proposed three principled approaches to compute the prescription dose based on the probabilistic distribution of the tumor cell density. First, we minimize the surviving fraction of tumor cells after irradiation in the most probable case. Second, we minimize the expected survival fraction tumor cells after irradiation. Third, we present an approach to correct the prescription dose to take into account the presence of adjacent organs at risk. Finally, we present Intensity Modulated Radiation Therapy (IMRT) of the three prescription doses. This method allows to automatically generate prescription doses conformal to the targeted tumor. We present the results of our approach on two patients diagnosed with high grade glioma. We detail the results in terms of dose volume histograms of the target volume and organs at risk.

7.1 Introduction

High grade glioma is one of the most common and aggressive types of primary brain tumors. The treatment of high grade glioma usually involves resection when possible, followed by concurrent chemotherapy and radiotherapy.

The use of computational growth models for gliomas have focused on modeling response to chemotherapy, surgical resection, and radiotherapy. For instance, a sink term can be added to the reaction-diffusion equation in order to model the impact of chemo or radiotherapy [Tracqui et al., 1995, Rockne et al., 2009]. The resection of a brain tumor can also be modeled by suppressing the tumor cells present in the resection region [Swanson et al., 2003], [Stretton et al., 2012]. More advanced therapy schedules using for instance anti-angiogenic drugs can also be studied with more complex models [Saut et al., 2014].

In this chapter, we focus on the use of mathematical models to personalize radiotherapy planning. Radiotherapy has been proven to be the single most effective therapy in the management of high grade gliomas [Kristiansen et al., 1981]. However, its planning is made difficult by the infiltrative nature of the disease, and the uncertainty in the abnormality revealed by the Magnetic Resonance Images (MRI). [Rockne et al., 2010, Rockne et al., 2015] personalized a tumor growth model taking into account the effect of radiotherapy to high grade glioma patients using imaging modalities such as T1 with Gadolinium contrast agent (T1Gd), T2-FLAIR, and Positron Emission Tomography. They showed that the personalization of such a model could help predicting the impact of therapy on the progression of the tumor. [Corwin et al., 2013, Holdsworth et al., 2012] used the previous model to optimize the dose delivery so as to minimize the amount of surviving cells. They use a spherically symmetric implementation of the tumor growth model in order to optimize the dose and fractionation scheme of the planning. They showed that personalizing delivered dose could improve therapy in terms of survival days gained by the patients. [Unkelbach et al., 2014b, Unkelbach et al., 2014a] studied the optimization of the radiotherapy planning based on a tumor growth model in order to automatically define a 3D prescription dose taking into account the natural boundaries and privileged pathways of the tumor progression. They studied the difference between this dose planning and the routinely defined plan, as well as its impact on the Intensity Modulated Radiation Therapy (IMRT) dose.

In this chapter, we build on the previous works to develop a method to propose prescription doses based on a personalized tumor extrapolation model. We utilize a tumor growth model based on a reaction diffusion equation, which models the infiltrative spread of tumor cells in the healthy appearing brain tissue. A Bayesian approach is taken to estimate the posterior distribution over the model parameters based on the MRIs of the patient, either from a single acquisition prior to therapy, or from two time points before therapy. A recently proposed method to sample plausible image segmentations is used to incorporate uncertainty in the segmentation of the tumor in the MR images [Lê et al., 2015b]. The tumor cell density simulated by those models is then combined with an exponential cell survival model

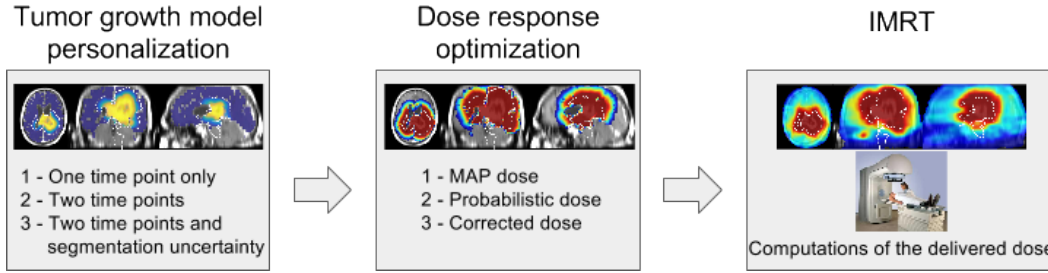


Figure 7.1: Summary of the method: the personalization of a tumor growth model is combined with a dose response model to optimize the prescription dose. The delivered dose is computed as the IMRT planning of the prescription dose. Different scenarios are compared for the personalization of the model and the computation of the prescription doses.

to describe the effect of radiotherapy. The probability distribution over tumor cell densities, together with the cell survival model, is used to define the prescription dose distribution, which is the basis for subsequent IMRT planning. The pipeline is summarized on Figure 7.1.

The chapter is divided as follow: i) the generation of different plausible segmentations based on the clinical ones is presented in Section 7.2, ii) the forward model of tumor growth is presented in Section 7.3, iii) the personalization method is presented in Section 7.4, iv) the personalized dose response model to define the prescription dose and the IMRT is detailed in Section 7.5. To our knowledge, this is the first work using a personalized model of brain tumor growth taking into account the uncertainty in the clinician segmentations in order to optimize radiotherapy planning.

In this chapter, we consider three different scenarios. In the first one, we only consider a single MRI acquisition of the T1Gd and T2-FLAIR MRI before therapy planning. In the second, we consider two time points acquisition for a total of four MRIs: the T1Gd at the first and second time point, the T2-FLAIR at the first and second time point (see Figure 7.2). In the third scenario, we include the uncertainty in the segmentation of the abnormality visible on the different MRIs to the personalization strategy.

7.2 Segmentation Samples

The T1Gd abnormality, which is the active part of the tumor, and the larger T2-FLAIR abnormality, which is usually called the edema, were segmented by a clinician. In order to take into account the uncertainty in the segmentation, we propose to randomly modify the original clinician segmentations. The method is based on [Lê et al., 2015b], where samples of such segmentations are generated from a high dimensional Gaussian process, as the zero crossing of a level function. The samples are efficiently produced on the regular grid using the separability and stationary prop-

erties of the squared exponential covariance function (see Chapter 5). The samples take into account the image intensity information using the signed geodesic distance as the mean of the Gaussian process.

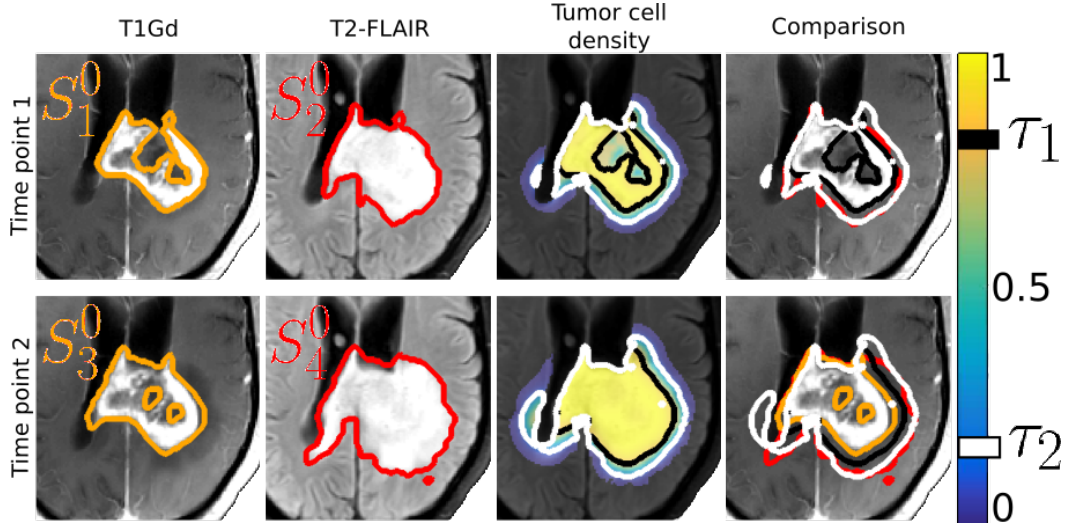


Figure 7.2: (Left) The proliferative rim is outlined in orange on the T1Gd MRI at two different time points; (Middle Left) The edema is outlined in red on the T2-FLAIR MRI at two different time points. The edema encloses the proliferative rim; (Middle Right) Tumor cell density computed with the reaction-diffusion model. The black (resp. white) line is the threshold values τ_1 (resp. τ_2) corresponding to the T1Gd (resp. T2-FLAIR) abnormality; (Right) Comparison between the clinician segmentation and the contours from the model. The indices \mathbf{S}_i for $i = 1, 2, 3, 4$ identifying the clinical segmentations are overlaid on the corresponding figure.

Segmentation samples for the T1Gd and T2-FLAIR abnormalities at the first and second time points are generated. We note S_i^0 for $i = 1, 2, 3, 4$ the clinical segmentations for the T1Gd and T2-FLAIR abnormalities at the first and second time points respectively (see Figure 7.2). We note \mathbf{S}_i for $i = 1, 2, 3, 4$ the sets of K plausible segmentations per modality and time point. In other words, $\mathbf{S}_i = \{S_i^k\}_{k=1, \dots, K}$ where each S_i^k is a plausible sample from S_i^0 , the i -th clinician segmentation.

Figure 7.3 shows examples of such samples for $K = 5$. The samples automatically respect boundaries of the tumor progression such as the ventricles, because of the presence of large intensity gradients. The five presented samples per abnormality correspond to an average DICE of 87%, which is comparable with the inter-expert DICE measured in the BraTS Challenge for brain tumors delineation [Menze et al., 2015]. Comparing the output of the forward tumor growth model with these plausible noisy segmentations allows to include the uncertainty we have in the original clinician segmentation.

7.3 Tumor Growth Model

The tumor growth model is based on the reaction-diffusion equation,

$$\frac{\partial u}{\partial t} = \underbrace{\nabla(D \cdot \nabla u)}_{\text{Diffusion}} + \underbrace{\rho u(1 - u)}_{\text{Logistic Proliferation}} \quad (7.1)$$

$$D \nabla u \cdot \vec{n}_{\partial\Omega} = 0 \quad (7.2)$$

Equation (7.1) describes the spatio-temporal evolution of the tumor cell density u , which infiltrates neighboring tissues with a diffusion tensor D , and proliferates with a net proliferation rate ρ . Equation (7.2) enforces Neumann boundary conditions on the brain parenchyma domain Ω . Following [Lê et al., 2015a], we define the diffusion tensor as $D = d_w \mathbb{I}$ in the white matter, and $D = d_w/10 \mathbb{I}$ in the gray matter, where \mathbb{I} is the 3x3 identity matrix. We further identify the scalar parameter d_w with D .

The solution of the reaction-diffusion equation (7.1) is a tumor cell density u computed over the whole brain domain. In order to relate the tumor cell density u to the MRIs, the frontier of the visible abnormalities is assumed to correspond to a threshold value of the tumor cell density u . We note τ_1 the value of the tumor cell density u corresponding to the frontier of the T1Gd abnormality, and τ_2 the value corresponding to the frontier of the T2-FLAIR abnormality (see Figure 7.2).

The initialization of the tumor cell density $u(t = t_1, x)$ at the time of the first acquisition is of particular importance, as it impacts the rest of the simulation. In this work, the tumor tail extrapolation algorithm described by [Konukoglu et al., 2010a] is used. The tumor cell density is computed outward (and inward) of one of the T1Gd abnormality segmentations, as a static approximation of the wave-like solution of equation (7.1) with parameters (D, ρ) . It only depends on the invisibility index $\lambda = \sqrt{D/\rho}$. By construction of the initialization, the T1Gd abnormality falls exactly on the threshold τ_1 of the tumor cell density at the first time point.

The reaction-diffusion equation is solved using the Lattice Boltzmann Method [Lê et al., 2015a, Yoshida and Nagaoka, 2010, Yu et al., 2003] which allows an easy parallelization and fast computations.

7.4 Personalization

The personalization of the tumor growth model will be combined to a dose response model in order to define the radiotherapy planning. We compare three different scenarios. First we only use a single time point (the second acquisition) to personalize the model such that the radiotherapy plan will be defined using a single acquisition, similarly to what is being done in clinic. Second we use two time points in order to take into account the temporal evolution of the two abnormalities, and not only their extent at the second time point. The radiotherapy plan will then be defined on the latest acquisition. Third, we use two time points and include the uncertainty in the segmentations of the two abnormalities at the two instants.

7.4.1 Scenario 1: One time point only

In this section, we are interested in the posterior probability of the model parameter $\theta = (D, \rho)$, knowing the clinical segmentations S_3^0 on the T1Gd and S_4^0 on the T2-FLAIR at the second time point. To cast the problem in a probabilistic framework, we follow Bayes rule: $P(\theta|S_3^0, S_4^0) \propto P(S_3^0, S_4^0|\theta) P(\theta)$. The likelihood is modeled as

$$P(S_3^0, S_4^0|\theta) \propto \exp\left(-\frac{H(D, \rho, S_3^0, S_4^0)^2}{\sigma^2}\right) \quad (7.3)$$

where $H(D, \rho, S_3^0, S_4^0)$ is the 95th percentile of the symmetric Hausdorff distance between the border of the segmentation S_4^0 , and the isoline at τ_2 of the simulated tumor cell density u using (D, ρ) , and initialized with the segmentation S_3^0 . We further model the prior as log-uniform and independent between the parameters,

$$P(\theta) = P(D)P(\rho) \quad (7.4)$$

We sample from the posterior distribution using a Metropolis-Hasting algorithm. Note that this section only uses the initialization algorithm (see Section 7.3) which only depends on the invisibility index $\lambda = \sqrt{D/\rho}$.

7.4.2 Scenario 2: Two time points

In this section, we are interested in the posterior probability of the model parameter $\theta = (D, \rho)$, knowing the clinical segmentations S_i^0 for $i = 1, 2, 3, 4$ on the T1Gd and T2-FLAIR at the first and second time point respectively. In this case, the likelihood is modeled as

$$P(\{S_i^0\}_{i=1,2,3,4}|\theta) \propto \exp\left(-\frac{1}{\sigma^2} \left(\frac{\sum_{i=2}^4 H_i(D, \rho, S_1^0, S_i^0)}{3}\right)^2\right) \quad (7.5)$$

where $H_i(D, \rho, S_1^0, S_i^0)$ is the 95th percentile of the symmetric Hausdorff distance between the border of the segmentation S_i^0 for $i = 2, 3, 4$, and the isoline of the simulated tumor cell density u using (D, ρ) , and initialized with the segmentation S_1^0 . We model the prior as described in Section 7.4.1.

We sample from the posterior distribution using the Gaussian Process Hamiltonian Monte Carlo (GPHMC) algorithm first described by [Rasmussen, 2003], and used for tumor growth personalization in [Lê et al., 2015a].

7.4.3 Scenario 3: Two time points and segmentation uncertainty

In this section, we want to include the uncertainty in the segmentation to the personalization process. We denote the set of plausible segmentations by $S = \{S_i\}_{i=1,2,3,4}$ (see Section 7.2). We introduce the random variables $\mathcal{Z}_i = (\mathcal{Z}_{i1}, \dots, \mathcal{Z}_{iK})$ for

$i = 1, 2, 3, 4$, which are one-hot binary vectors where $P(\mathcal{Z}_{ij} = 1|S) \propto P(S_{ij})$, and $\mathcal{Z}_{il} = 0$ for $l \neq j$ when $\mathcal{Z}_{ij} = 1$. The random variable \mathcal{Z}_i is a measure of the plausibility of the samples. We are interested in the posterior probability of the model parameter $\boldsymbol{\theta} = (D, \rho, \mathcal{Z}_1, \mathcal{Z}_2, \mathcal{Z}_3, \mathcal{Z}_4)$, knowing the observations S . We model the likelihood as

$$P(S|\boldsymbol{\theta}) \propto \exp\left(-\frac{1}{\sigma^2} \left(\frac{\sum_{i=2}^4 H_i(D, \rho, \mathcal{Z}_1, \mathcal{Z}_i)}{3}\right)^2\right) \quad (7.6)$$

where $H_i(D, \rho, \mathcal{Z}_1, \mathcal{Z}_i)$ is the 95th percentile of the symmetric Hausdorff distance between the border of the segmentation indexed by \mathcal{Z}_i , and the isolines of the simulated tumor cell density u using (D, ρ) , and initialized with the contour selected with \mathcal{Z}_1 . We model the prior independent between the parameters, and log-uniform for D and ρ ,

$$P(\boldsymbol{\theta}) = P(D)P(\rho) \prod_{i=1}^4 P(\mathcal{Z}_i) \quad (7.7)$$

We sample from the posterior distribution using the GPHMC like in Section 7.4.2. The only difference is that at each iteration, we randomly sample segmentations from the prior $P(\mathcal{Z}_i)$.

7.5 Radiotherapy Planning

In this section, we detail how we use the personalization of the tumor growth model in order to define the best radiotherapy plan at the time of the second acquisition. We start by coupling the estimated tumor cell density with a cell survival model (Section 7.5.1). We then detail how to compute the **prescription doses** in Section 7.5.2, and how to compute the **delivered dose** in Section 7.5.3.

7.5.1 Cell survival

Cell survival after irradiation is often modeled using the linear-quadratic cell survival model. In this chapter, we follow the derivations of [Unkelbach et al., 2014b], and consider the linear approximation of the linear-quadratic model. In this framework, the density of surviving tumor cells s after irradiation with a cumulative dose d in Gray (Gy = Joules / kg) is given by

$$s = u \exp(-\bar{\alpha}d) \quad (7.8)$$

where u is the tumor cell density before irradiation, and $\bar{\alpha}$ is the radiosensitivity parameter, corrected for the fact that we consider a linear approximation of the linear-quadratic model.

7.5.2 Prescription Dose Optimization

A prescription dose can be defined as the dose minimizing the surviving fraction of tumor cells. This is formally defined as the dose solving the following optimization problem [Unkelbach et al., 2014b],

$$\underset{d}{\text{minimize}} \quad f(d, u) = \sum_{i \in I} u_i \exp(-\bar{\alpha} d_i) \quad (7.9)$$

$$\text{subject to} \quad \sum_{i \in I} d_i \leq d^{\text{int}} \quad (7.10)$$

$$d_i \geq 0 \quad (7.11)$$

where I is the set of voxels in the image. Equation (7.9) aims at minimizing the number of surviving tumor cells. Equation (7.10) constrains the integral dose to be lower or equal to a user defined value d^{int} , in order to avoid the trivial solution of delivering an infinite dose. The parameter d^{int} can be defined based on clinical considerations related to the total dose a brain can tolerate. Equation (7.11) represents the non-negativity constraint for the dose.

The optimal prescription dose can be found by setting to zero the derivative of the corresponding Lagrangian, resulting in

$$d_i = \max \left[0, \frac{1}{\bar{\alpha}} \ln \left(\frac{u_i \bar{\alpha}}{\mu} \right) \right] \quad (7.12)$$

where μ is the Lagrange multiplier of the integral dose constraint. This solution leads to a surviving tumor cell density $s = \mu/\bar{\alpha}$ when the dose is strictly positive, and $s < \mu/\bar{\alpha}$ elsewhere. On the discrete grid formed by the image, we denote $\{t_1, \dots, t_l\}$ the ordered list from which the tumor cell density u takes its value. To compute the solution of the optimization problem, the voxels with highest value t_l are targeted with the dose needed to set the cell density to t_{l-1} (i.e. $t_l - t_{l-1}$ cells are killed with the dose). In other word, we set the largest tumor cell density equal to the second largest using a certain dose. This is done iteratively until the integral dose constraint is activated (i.e. there is no dose left to use, see [Unkelbach et al., 2014a]). A local maximum dose constraint of 60 Gy following clinical recommendation is also included.

The personalization of the tumor growth model provides samples $\{\theta_i\}$ from the posterior distribution $P(\theta|S)$. We propose below three different principled methods to compute prescription doses based on the computed samples.

7.5.2.1 MAP Dose

The MAP (Maximum A Posterior) dose is defined as the dose minimizing the surviving fraction of the most probable tumor cell density noted $u(\theta^{\text{MAP}})$. This dose does not take into account the uncertainty in the personalization.

7.5.2.2 Probabilistic Dose

The probabilistic dose is defined as the dose minimizing the expectation of the survival fraction of tumor cell density. This expectation can be estimated using samples from the posterior distribution as follows,

$$\mathbb{E}_\theta [f(d, u(\boldsymbol{\theta}))] = \mathbb{E}_\theta \left[\sum_{i \in I} u_i(\boldsymbol{\theta}) \exp(-\bar{\alpha}d_i) \right] \quad (7.13)$$

$$\simeq \sum_{i \in I} \frac{1}{N} \sum_{\theta} u_i(\boldsymbol{\theta}) \exp(-\bar{\alpha}d_i) \quad (7.14)$$

$$\simeq \sum_{i \in I} \hat{u}_i \exp(-\bar{\alpha}d_i) \quad (7.15)$$

$$\simeq f(d, \hat{u}) \quad (7.16)$$

where $\hat{u} = \frac{1}{N} \sum_{\theta} u(\boldsymbol{\theta})$ is the empirical mean of the tumor cell density. Computing the probabilistic dose is then equivalent to minimizing the fraction of surviving tumor cells using the empirical mean tumor cell density \hat{u} .

7.5.2.3 Corrected Dose

The corrected dose is defined as the prescription dose corrected for the presence of neighboring organs at risk (OARs). We minimize the surviving fraction of tumor cell density minus the surviving fraction of the OARs cell density (i.e. we penalize the death of OAR cells) as follows,

$$\underset{d}{\text{minimize}} \quad f(d, \hat{u}) - \delta f(d, \beta c) \quad (7.17)$$

where $\beta(i)$ is the empirical standard deviation of the tumor cell density at the i th voxel (Figure 7.7), c is the cell density of the OARs, and δ is a factor which weighs the impact of the correction. The term βc translates the fact that we only consider the impact of the OARs in the regions of high uncertainty in the tumor cell density. Note that $f(d, \hat{u}) - \delta f(d, \beta c) = f(d, \hat{u} - \delta \beta c)$. Hence taking into account the OARs is equivalent to minimizing the original problem using the corrected tumor cell density $\hat{u} - \delta \beta c$.

7.5.3 IMRT Planning

We optimize an Intensity Modulated Radiation Therapy (IMRT) plan using 9 equally spaced coplanar 6MV photon beams and a piece-wise quadratic objective function, following the formalism of [Unkelbach et al., 2014b, Unkelbach et al., 2014a]. The optimization problem is solved using the L-BFGS quasi-newton method; dose-calculation is performed using the software CERR 3.0 Beta 3 [Deasy et al., 2003]. More specifically, we minimize the following objective function

OAR	ω^o	d^{\max}		ω^o	ω^u	d^{grad}	d^{low}
Brainstem	10	45	Target T	10	20	-	-
Optic nerves	10	30	Unclassified H	10	5	40	20
Chiasm	10	30					
Eye lenses	10	10					
Eye balls	10	10					

Table 7.1: Objective function parameters for the IMRT optimization.

$$g(d) = \sum_{\eta} \frac{\omega_{\eta}^o}{N_{\eta}} \sum_{i \in V_{\eta}} (d_i - d_{\eta}^{\max})_+^2 \quad (7.18)$$

$$+ \frac{\omega_T^u}{N_T} \sum_{i \in T} (d_i^{\text{pres}} - d_i)_+^2 \quad (7.19)$$

$$+ \frac{\omega_T^o}{N_T} \sum_{i \in T} (d_i - d_i^{\text{pres}})_+^2 \quad (7.20)$$

$$+ \frac{\omega_H^u}{N_H} \sum_{i \in H} (d_i^{\text{pres}} - d_i)_+^2 \quad (7.21)$$

$$+ \frac{\omega_H^o}{N_H} \sum_{i \in H} (d_i - d_i^{\max})_+^2 \quad (7.22)$$

The first term (7.18) denotes overdose objectives for the organs at risk (OAR). The second term (7.19) denotes underdose objectives within a confined target volume T . The third term (7.20) denotes overdose objectives within a confined target volume T . The fourth term (7.21) aims at delivering the prescribed dose to voxels outside of T ; and the fifth term (7.22) represents a conformity objective that penalizes dose to unclassified voxels outside of T (including skull, brain tissue, ventricles). The target volume T is defined as an isocontour of the average tumor cell density \hat{u} which encloses the same volume as the Clinical Target Volume (CTV) defined by the clinician. Following [Unkelbach et al., 2014a] the conformity objective is defined at each voxel as

$$d_i^{\max} = \max \left[d^{\text{low}}, \max_j \left(d_j^{\text{pres}} - z_{ij} d^{\text{grad}} \right) \right] \quad (7.23)$$

where z_{ij} denotes the Euclidean distance of the voxel i from another voxel j which has a non-zero prescription dose d_j^{pres} . The parameter d^{grad} is specified in Gy per cm and describes the desired dose falloff in healthy tissue; d_i^{low} is a lower dose threshold below which dose is not penalized. This conformity objective allows to penalize reasonably regions such as the ventricles where the prescription dose d^{pres} is null. The parameters of the objective function are summarized in Table 7.1.

7.6 Results

We present the results for a high grade glioma patient. This patient was not subject to surgical resection, but was under a complex treatment of concurrent chemo- and radiotherapy. We picked two time points separated by 28 days which revealed a visible growth to conduct our experiments. The CT is used for the IMRT dose calculations.

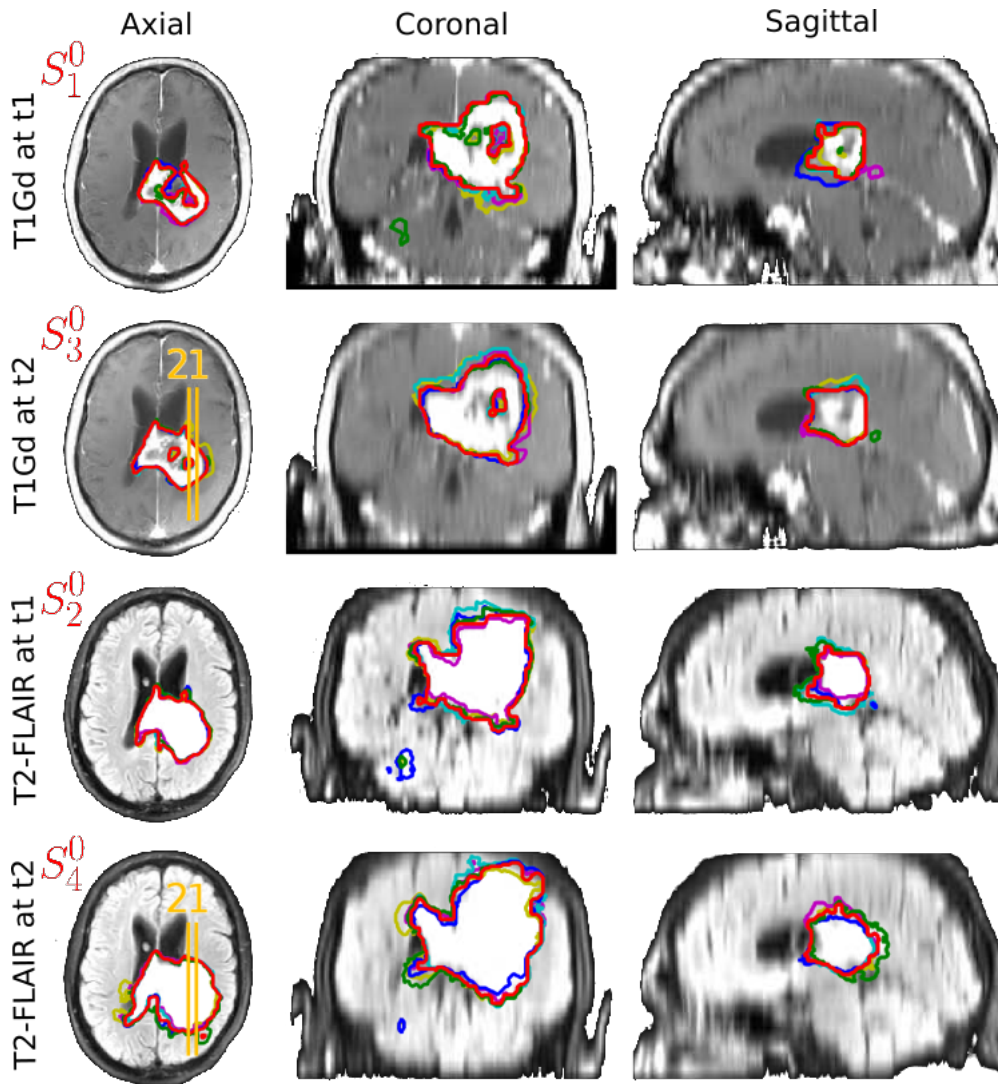


Figure 7.3: From top to bottom: segmentation samples for the T1Gd at the first and second time points, and for the T2-FLAIR at the first and second time points. The sample are generated independently for the different time points and modalities. The different colors correspond to the different samples. The original clinical segmentation S_i^0 for $i = 1, 2, 3, 4$ is in red on the different modalities. The yellow bars are indications for Figure 7.6.

The threshold for the T1Gd and T2-FLAIR abnormalities is set to $\tau_1 = 80\%$ and $\tau_2 = 16\%$ respectively [Swanson et al., 2008]. The log-uniform prior is bounded such that $D \in [10^{-4}, 10]$ mm²/days, and $\rho \in [10^{-5}, 10]$ days⁻¹ which encloses clinically expected values [Harpold et al., 2007]. Following the previous chapter, the noise level is set to $\sigma = 5$ mm for the likelihood. For the scenario 1, 4000 samples are drawn from the posterior with a normal distribution with standard deviation 0.3 for the proposal function, leading to an acceptance rate of 30%. For scenarios 2 and 3, 2000 samples are drawn from the posterior distribution, leading to an acceptance rate of 60%.

Figure 7.4 shows the histograms of the invisibility index $\lambda = \sqrt{D/\rho}$ for the three scenarios. Including the second time point, and the uncertainty in the segmentation, increases the uncertainty in the invisibility index. Indeed, the histogram is rather peaked when using a single time point, and it becomes less peaked when including the second time point. Moreover, including the second time point changes the value of the invisibility index to smaller values. Figure 7.5 shows the samples from the posterior density of the parameters D and ρ knowing the considered segmentations when using two time points (Left) and when including the uncertainty in the segmentation (Middle). We can see that the presence of two close modes in the region of high probability disappears when the uncertainty in the segmentation is considered. The samples reveal an asymmetric posterior distribution where the mode and mean are different, hinting the fact the probabilistic and MAP dose distributions will be different as well. Moreover, the histograms of the random variable \mathcal{Z}_i for $i = 1, 2, 3, 4$ (Figure 7.5 Right) show that all the segmentation samples are equally probable.

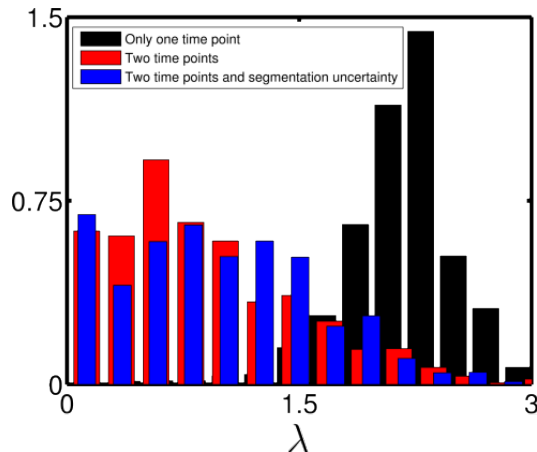


Figure 7.4: Normalized histogram of the distribution of the invisibility index $\lambda = \sqrt{D/\rho}$. The distribution using a single time point t_2 is more peaked (in black) than using two time points (in red), or two time points and the segmentation uncertainty (in blue). The mean value is greater using a single time point t_2 than using two time points, or two time points and the segmentation uncertainty.

Figure 7.2 (Right) shows the most probable tumor cell density taking into account the uncertainty in the segmentation, along with the extracted contours for the T1Gd and T2-FLAIR abnormalities. In the remainder of the chapter, we use 100 random samples from the posterior to compute the empirical mean and the standard deviation of the tumor cell density for the different scenarios.

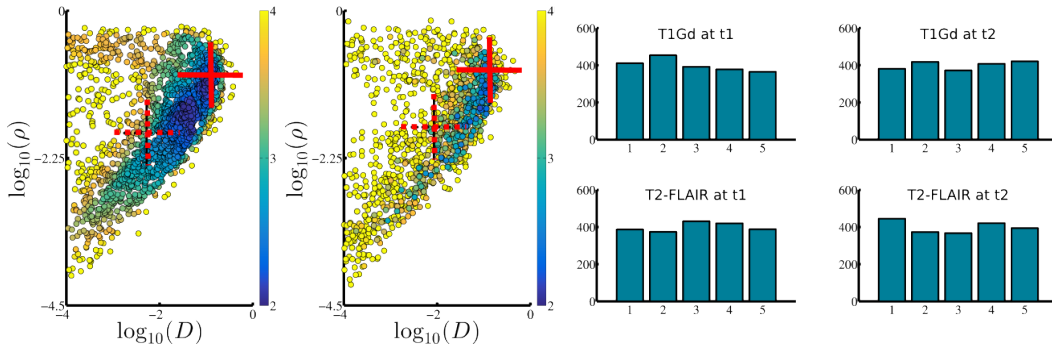


Figure 7.5: Posterior density of the joint probability $P(D, \rho|S)$ using only the clinical segmentations (Left) and taking into account the uncertainty in the segmentations (Middle). The colorbar indicates the negative log likelihood of the samples (yellow unlikely, blue very likely). The most probable sample is indicated with the crossing solid red lines, the mean is indicated with the dashed red lines. The histograms of the random variable Z_i are on the right.

Figure 7.6 shows the personalized tumor cell density profile extracted along two different lines at the second time point in the case of scenario 3, along with the boundaries of the segmentation samples. This allows to visualize the uncertainty in the computed tumor cell density. Figure 7.7 shows the axial, coronal, and sagittal views of the 3D empirical mean and standard deviation of the tumor cell density at the second time point for scenario 3. Those two figures highlights the two sources of uncertainty for scenario 3: the uncertainty in the segmentation, and the uncertainty in the infiltration of the tumor.

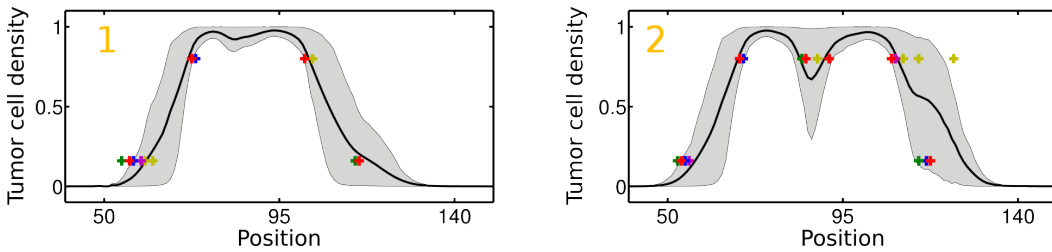


Figure 7.6: Visualization of the 3D tumor cell density profile extracted along 2 lines (in orange on Figure 7.3, identified by an orange number). The empirical mean of the tumor cell density is the solid black line, and the shaded area encloses the 10th to 90th percentiles. The colored crosses corresponds to the boundaries of the different segmentations visible on Figure 7.3 with the same color code.

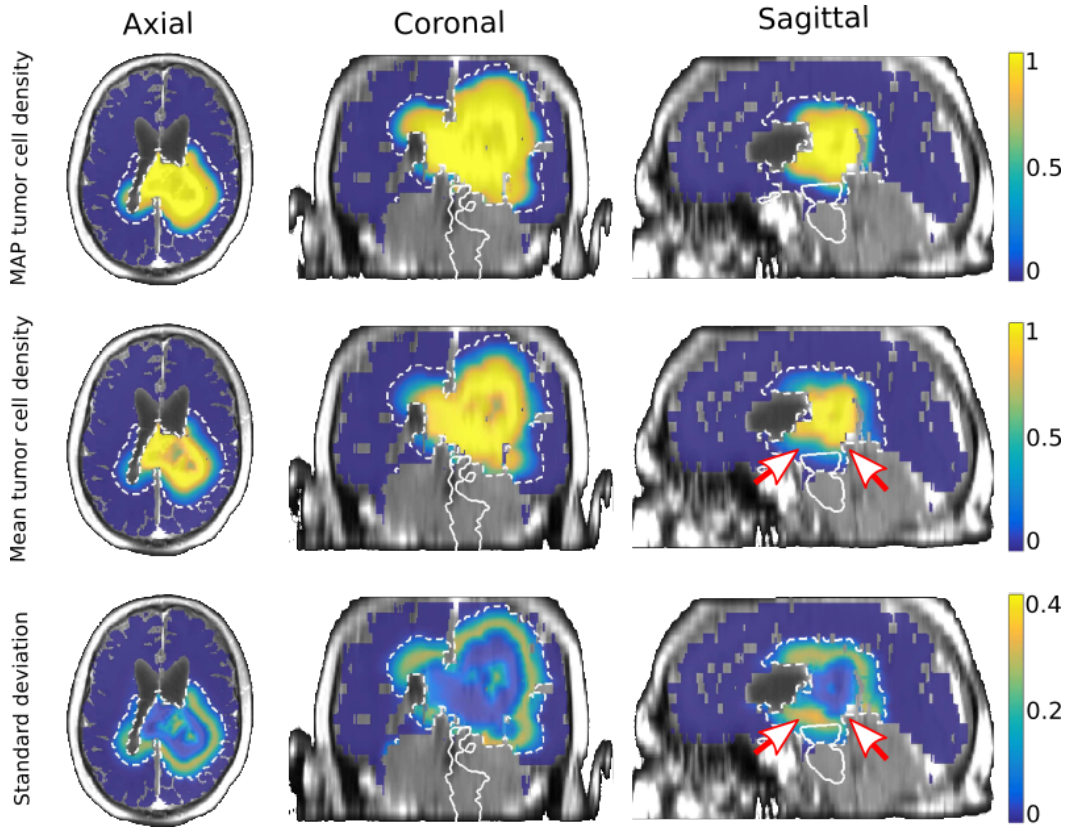


Figure 7.7: MAP (Top), mean (Middle), and standard deviation (Bottom) of the tumor cell density at the second time point computed with 100 random samples of the posterior, when taking into account two time points and the uncertainty in the segmentations. From left to right: axial, coronal, and sagittal views. The brainstem is outlined in white, and the target volume T is outlined with a dashed white line. The arrows indicate regions of varying uncertainty above the brainstem (see Figure 7.13).

The integral dose constraint is set equal to the total dose a patient would receive during a treatment following standard guidelines [Mason et al., 2007]. For that, we simulate a clinical target volume (CTV) by expanding with a 2cm margin the T1Gd abnormality visible on the second time point. To respect the boundaries of the tumor progression - much like a clinician would do - we define the CTV as the isoline of the average tumor cell density using only the second time point which is totally included in a 2cm expansion of the T1Gd abnormality. The clinical radiotherapy planning consists of targeting 60Gy inside the CTV, and 0 elsewhere (see Figure 7.8 Top). We compute the IMRT optimization of the clinical plan visible on Figure 7.9 (Top). We then set $d^{\text{int}} = 4.4e + 07 \text{ Gy}\cdot\text{mm}^3$ which corresponds to the IMRT dose delivered on the brain tissues (i.e. excluding the skull and cerebrospinal fluid). The radiosensitivity parameters $\bar{\alpha}$ is set to 0.35 1/Gy.

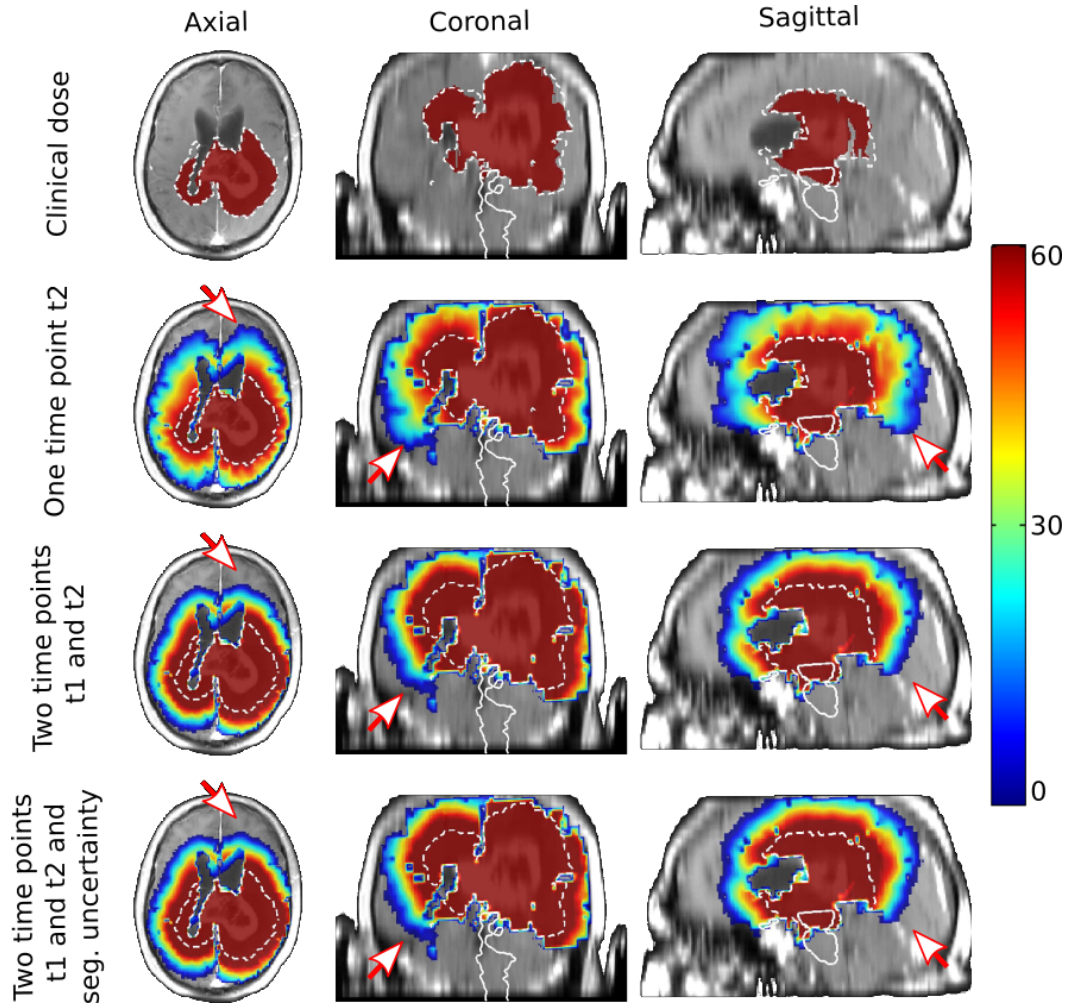


Figure 7.8: Prescription MAP doses in Gray for the clinical plan and the three different personalized plans. From top to bottom: clinical plan, using only the second time point, using the two time points, using the two time points and the segmentation uncertainty. From left to right: axial, coronal, and sagittal views. The arrows emphasize the difference of falloff between the different scenarios.

Figure 7.8 shows the prescription MAP doses in the three scenarios: i) using only the second time point, ii) using the two time points, iii) using the two time points and the segmentation uncertainty. In accordance with the histograms of invisibility index (Figure 7.4), we can see that the MAP dose using a single time point is more infiltrative compared to the doses using two time points (see the arrows on the different views of Figure 7.8). Furthermore, there is almost no difference between considering or not the impact of segmentation uncertainty (i.e. between scenario 2 and 3). Figure 7.9 shows the corresponding IMRT optimization of the MAP doses. We can see that the differences between the doses is largely attenuated by the smoothing effect of the IMRT optimization. This is confirmed by Figure 7.12 (Left) which shows the DICE coefficient of the 50Gy isolines of the different doses

before and after the IMRT optimization: the DICE coefficient is greater (on average 95%) after IMRT than before (on average 91%).

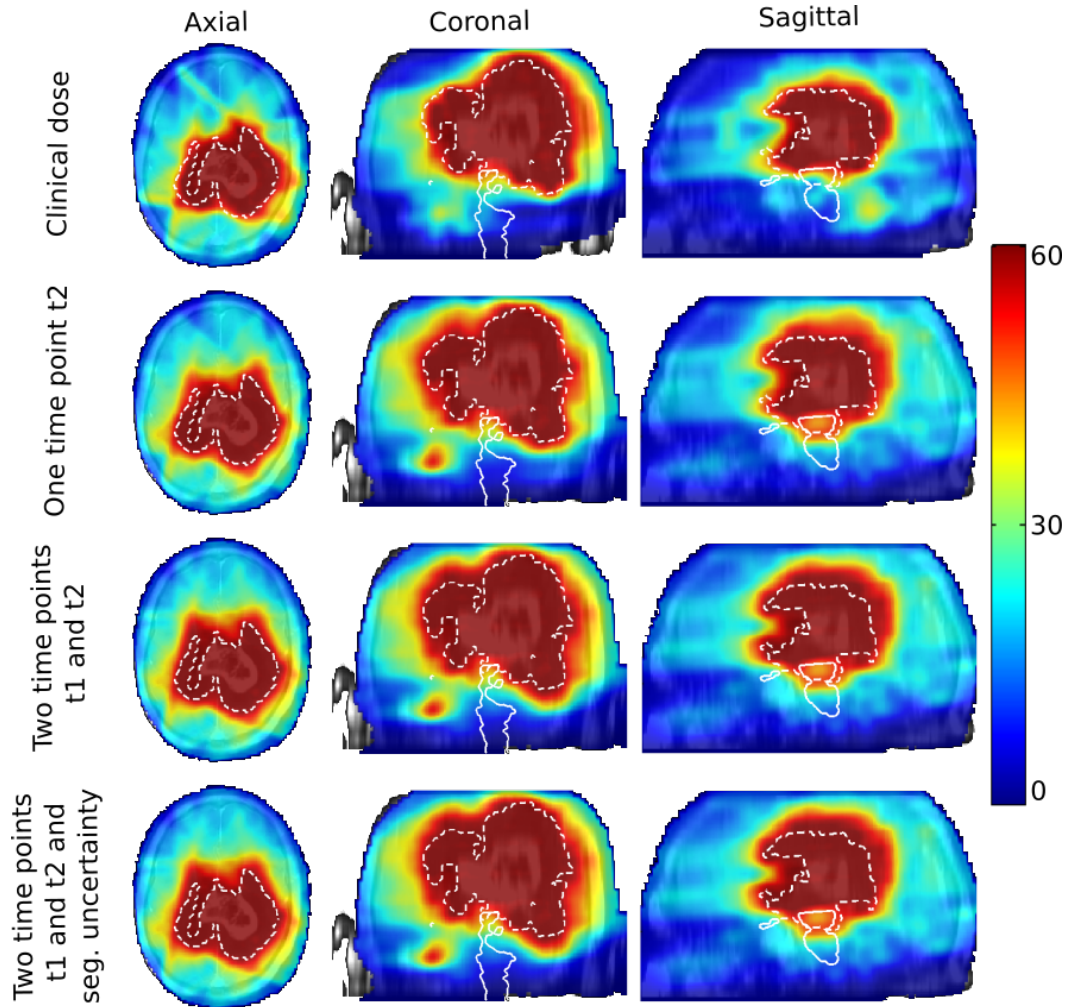


Figure 7.9: IMRT MAP doses in Gray for the clinical plan and the three different personalized plans. From top to bottom: clinical plan, using only the second time point, using the two time points, using the two time points and the segmentation uncertainty. From left to right: axial, coronal, and sagittal views.

Figure 7.10 shows the prescription probabilistic doses in the three scenarios. In this case, the difference between the scenarios is not as important (see the DICE coefficients on Figure 7.12 right). However, we can note that the infiltration of the prescription dose is this time greater for the scenarios taking into account the two time points, contrary to what happens using the MAP doses (see the arrows on the axial view of Figure 7.10). This is because the larger uncertainty in the invisibility index leads to a smoother falloff of the dose. Moreover, we can see the effect of taking into account the uncertainty on the segmentations on the coronal view (see the arrows on the coronal view of Figure 7.10). A part of the tumor near

the cerebellum is more strongly targeted with the third scenario. This is because this tumor is located near boundaries of the tumor progression and as such, the delineation of the segmentation has a big impact. Figure 7.11 shows that this effect is still very present after the IMRT optimization (see the arrows on the coronal view of Figure 7.11).

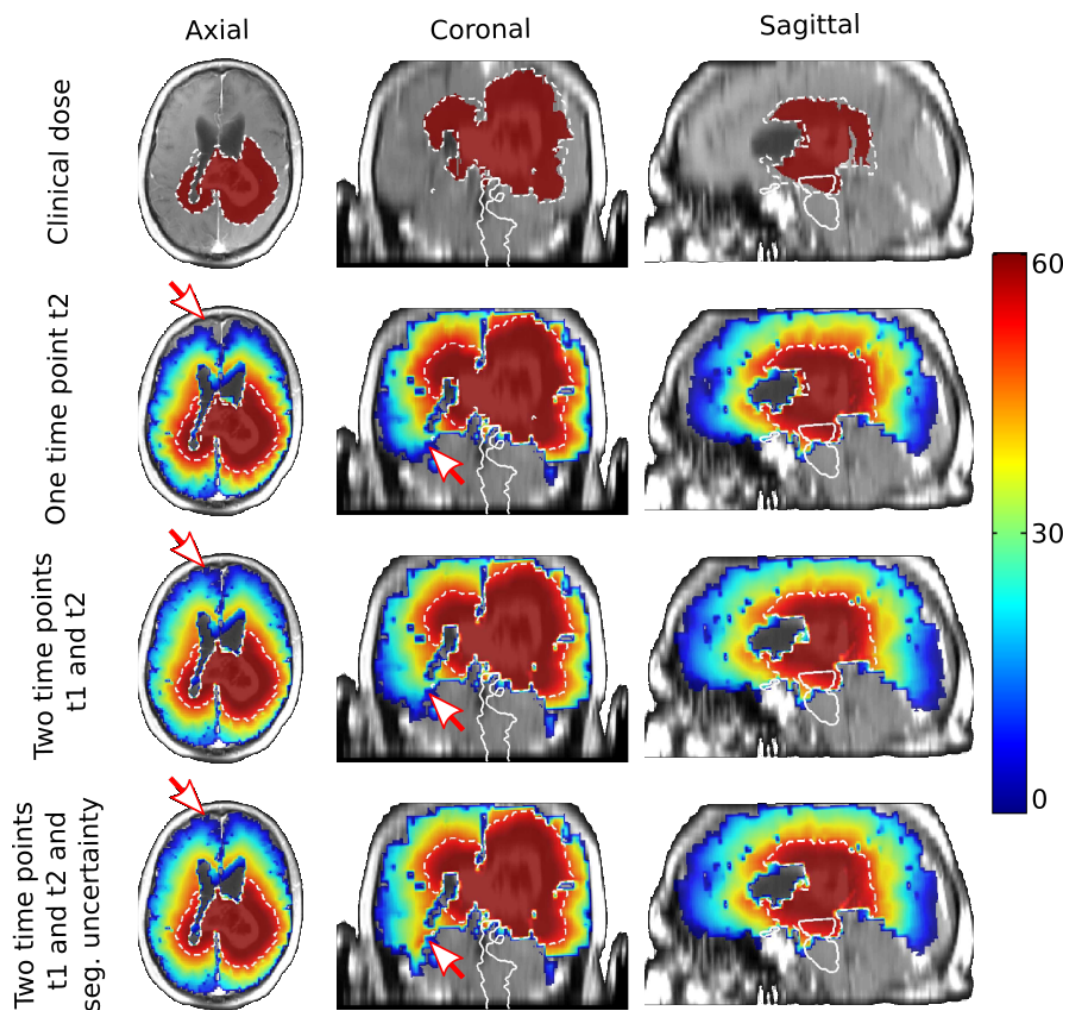


Figure 7.10: Prescription probabilistic doses in Gray for the clinical plan and the three different personalized plans. From top to bottom: clinical plan, using only the second time point, using the two time points, using the two time points and the segmentation uncertainty. From left to right: axial, coronal, and sagittal views. The arrows emphasize the difference of falloff between the different scenarios.

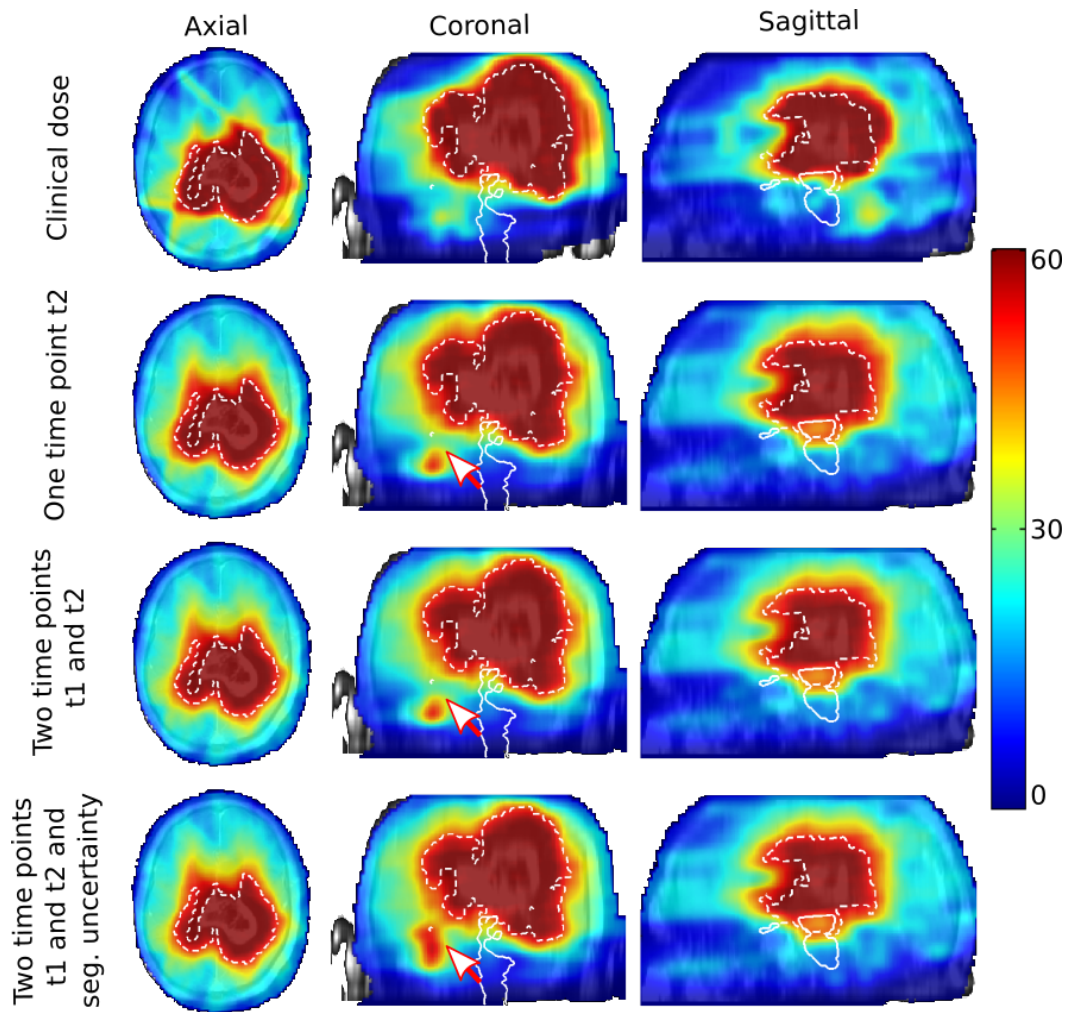


Figure 7.11: IMRT probabilistic doses in Gray for the clinical plan and the three different personalized plans. From top to bottom: clinical plan, using only the second time point, using the two time points, using the two time points and the segmentation uncertainty. From left to right: axial, coronal, and sagittal views. The arrows emphasize the difference of falloff between the different scenarios.

	OTP	TTP	TTPS	OTP	TTP	TTPS	
OTP		87	87		91	92	<div style="display: flex; align-items: center;"> <div style="width: 20px; height: 20px; background-color: #ADD8E6; margin-right: 5px;"></div> Prescription </div> <div style="display: flex; align-items: center; margin-top: 5px;"> <div style="width: 20px; height: 20px; background-color: #FFB6C1; margin-right: 5px;"></div> IMRT </div> <p style="font-size: small; margin-top: 5px;"> OTP: One Time Point t2 TTP: Two Time Points t1 and t2 TTPS: Two Time Points and seg. uncertainty </p>
TTP	93		99	94		97	
TTPS	92	99		95	97		
	MAP			Probabilistic			

Figure 7.12: DICE coefficient of the dose binarized with a 50Gy threshold for the different scenarios: using only one time point (OTP), using two time points (TTP), using two time points and the segmentation uncertainty (TTPS). The DICE coefficient is presented for the MAP doses (Left) and probabilistic doses (Right), and for the prescription doses (light blue) and the IMRT doses (light pink). One can note that the TTP and TTPS scenarios are the closest, and that the IMRT optimization reduces the differences between the doses.

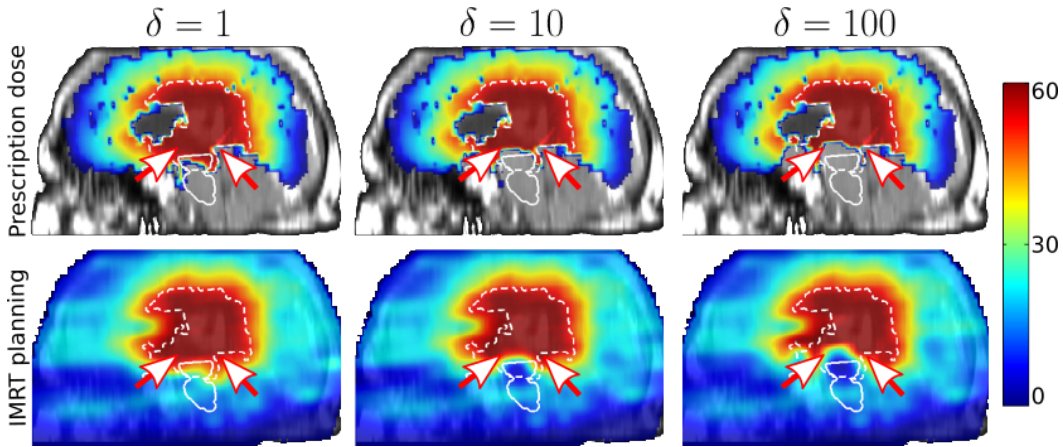


Figure 7.13: Prescription (Top) and IMRT (Bottom) doses in Gray for increasing values of δ (from left to right). We can see that with increasing δ , the dose around the brainstem is re-distributed (see the arrows).

Figure 7.13 shows a sagittal view of the corrected dose (Top) for different values of δ , and the corresponding IMRT dose (Bottom). The total amount of dose is the same for the three presented dose distributions since they respect the dose constraint. However, because of the correction factor, the dose prescribed inside the brainstem (outlined in white) is being re-targeted in other regions of the brain where the brainstem cell density and the uncertainty in the tumor cell density is lower. The white arrows on Figure 7.13 and 7.7 (sagittal view) show how the part of the dose where the tumor cell density is lower and the uncertainty higher (arrow on the left) is reduced whereas the dose where the tumor cell density is higher and the uncertainty lower (arrow on the right) is not redistributed. This translates in reduced delivered dose after the IMRT optimization. This can be more clearly observed by looking at the dose volume histograms on Figure 7.14. One can see

that, with increasing values of δ , the dose delivered to the brainstem is reduced, while the dose delivered to the target volume T as defined in section 7.5.3 remains the same.

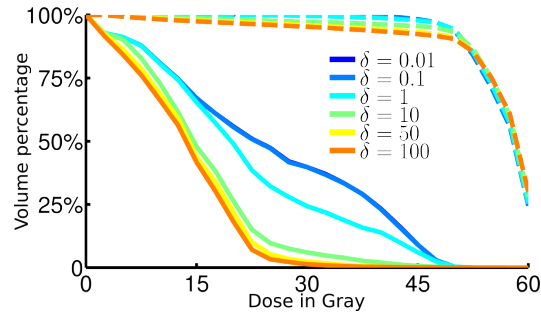


Figure 7.14: Dose volume histogram for the brainstem (solid lines) and the target volume T (dashed lines) for different values of δ . The x axis is the dose and the y axis is the percentage of volume targeted with this dose. Increasing the value of δ reduces the dose delivered to the brainstem while keeping the dose delivered to the target volume T approximately constant.

Finally, the knowledge of the delivered IMRT dose and the tumor cell density allows one to compute the tumor cell density after the therapy. Figure 7.15 shows the difference between the tumor cell density before and after therapy in the case of using only the second time point (scenario 1). We can see the huge drop in the tumor cell density as well as its standard deviation. Moreover, note that the standard deviation in the tumor cell density before therapy is greater when taking into account the two time points and the uncertainty on the segmentation (Figure 7.7).

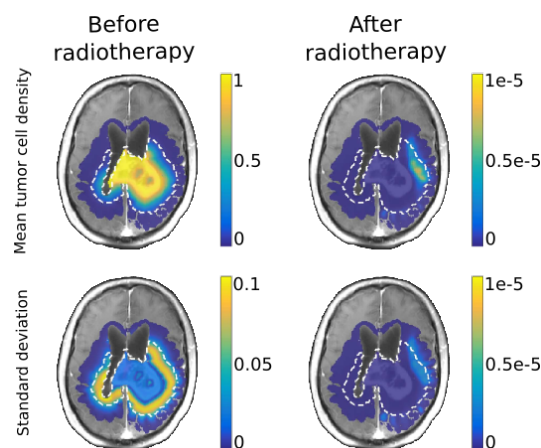


Figure 7.15: Mean (Top) and standard deviation (Bottom) of the tumor cell density before (Left) and after (Right) therapy in the first scenario (i.e. taking into account only the second time point).

7.7 Second Patient

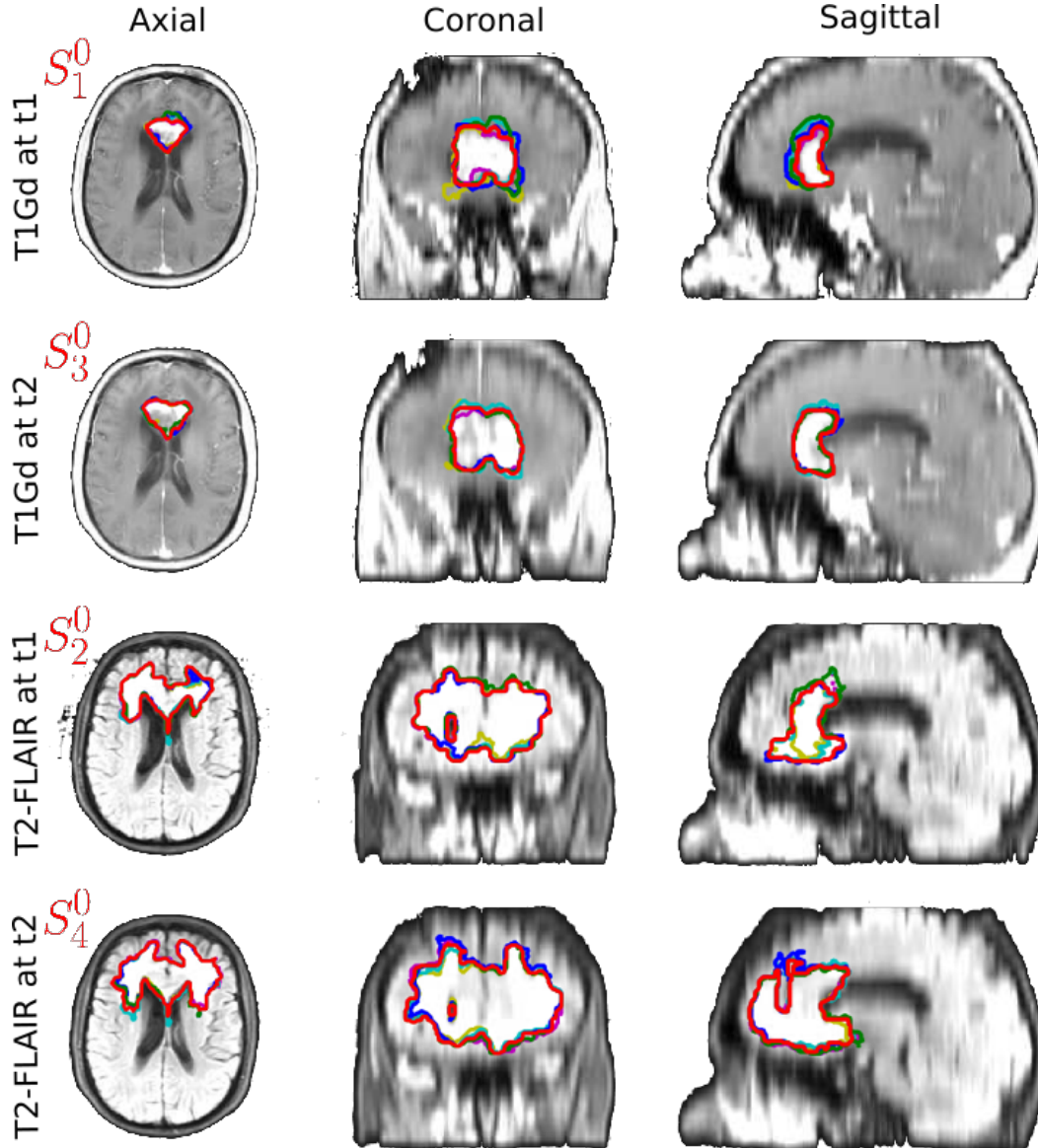


Figure 7.16: From top to bottom: segmentation samples for the T1Gd at the first and second time points, and for the T2-FLAIR at the first and second time points. The sample are generated independently for the different time points and modalities. The different colors correspond to the different samples. The original clinical segmentation S_i^0 for $i = 1, 2, 3, 4$ is in red on the different modalities.

The same method was applied to a second patient. The different segmentation samples used are on Figure 7.16. The histogram of the invisibility index on Figure 7.17 shows that, similarly to the previous patient, including a second time point and the uncertainty on the segmentation increases the uncertainty on the invis-

bility index. The samples from the posterior probability are on Figure 7.18. The mean and standard deviation of the tumor cell density are on Figure 7.19. Figure 7.20 and 7.21 shows the prescription and IMRT MAP doses. We can see that the infiltration is larger on the dose using a single time point. Figure 7.22 and 7.23 shows the prescription and IMRT probabilistic doses. The difference is very small between the different scenarios. Figure 7.24 shows the DICE coefficient between the different scenarios for the prescription and the IMRT doses. We can see that the IMRT smoothes out the differences between the prescription doses. The corrected prescription dose and its corresponding IMRT optimized dose for different values of δ are on Figure 7.25. The dose volume histograms of the IMRT corrected dose for different values of δ for the target volume and the brainstem are on Figure 7.26.

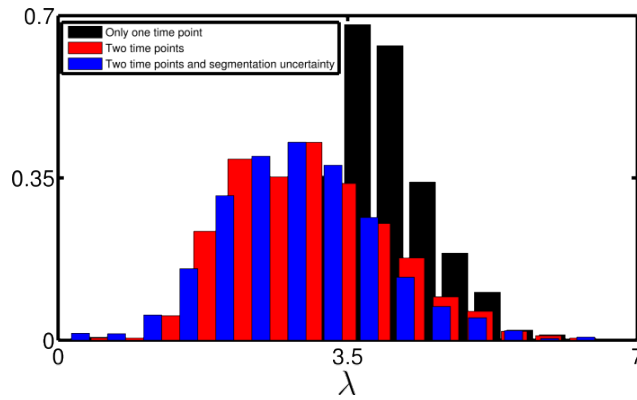


Figure 7.17: Normalized histogram of the distribution of the invisibility index $\lambda = \sqrt{D/\rho}$. The distribution using a single time point t_2 is more peaked (in black) than using two time points (in red), or two time points and the segmentation uncertainty (in blue).

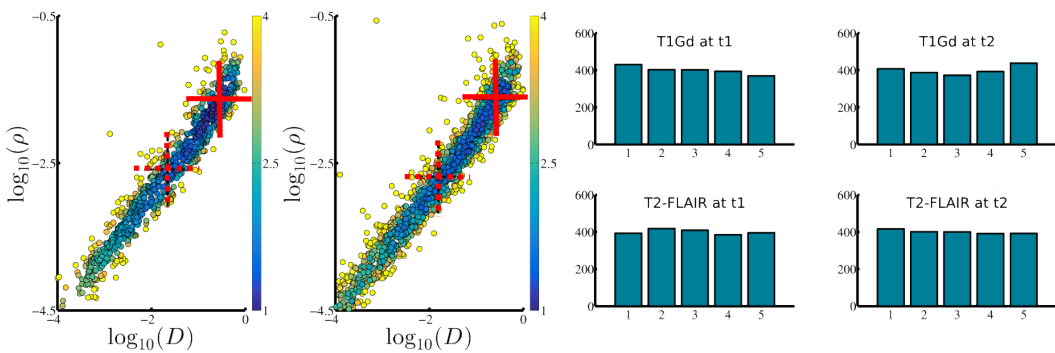


Figure 7.18: Posterior density of the joint probability $P(D, \rho|S)$ using only the clinical segmentations (Left) and taking into account the uncertainty in the segmentations (Middle). The colorbar indicates the negative log likelihood of the samples (yellow unlikely, blue very likely). The most probable sample is indicated with the crossing solid red lines, the mean is indicated with the dashed red lines. The histograms of the random variable Z_i are on the right.

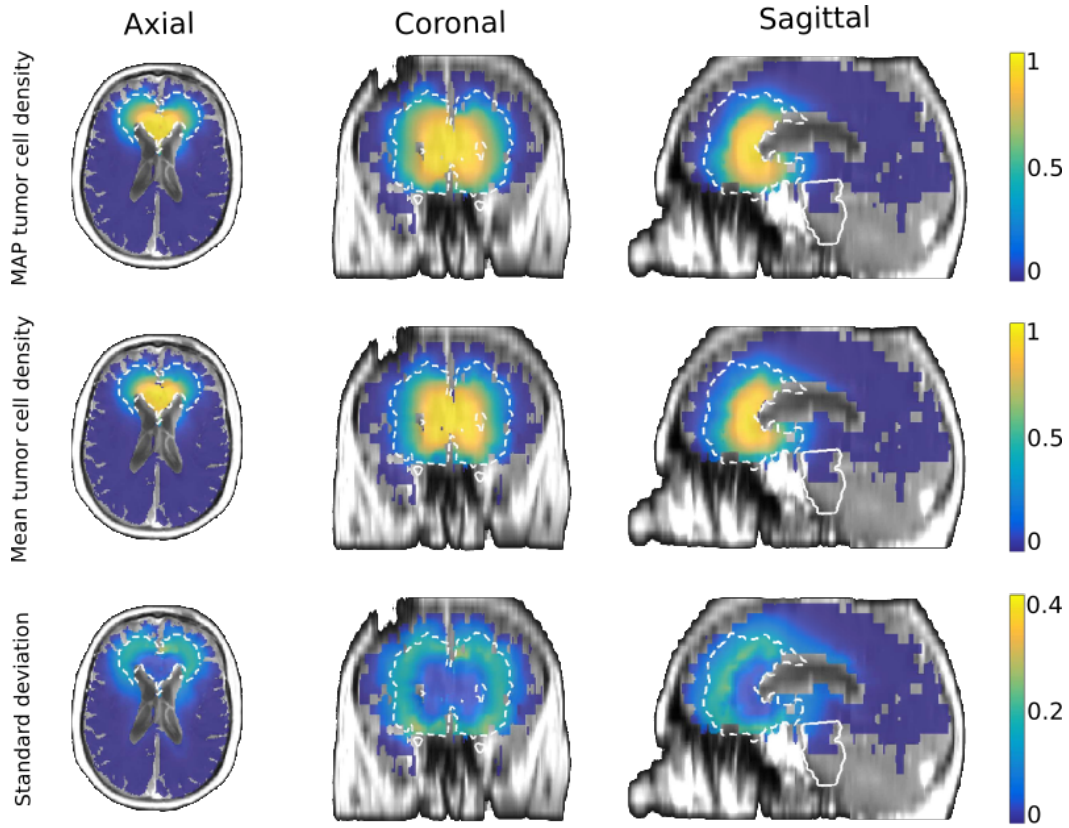


Figure 7.19: MAP (Top), mean (Middle) and standard deviation (Bottom) of the tumor cell density computed with 100 random samples of the posterior. From left to right: axial, coronal, and sagittal views. The brainstem is outlined in white, and the confined target volume T is outlined with a dashed black line.

	OTP	TTP	TTPS	OTP	TTP	TTPS	
OTP		79	90		83	83	<div style="display: flex; flex-direction: column; align-items: center;"> <div style="display: flex; align-items: center; margin-bottom: 5px;"> <div style="width: 20px; height: 10px; background-color: lightblue; margin-right: 5px;"></div> Prescription </div> <div style="display: flex; align-items: center; margin-bottom: 5px;"> <div style="width: 20px; height: 10px; background-color: lightpink; margin-right: 5px;"></div> IMRT </div> <div style="font-size: 0.8em; margin-top: 5px;"> OTP: One Time Point t2 TTP: Two Time Points t1 and t2 TTPS: Two Time Points and seg. uncertainty </div> </div>
TTP	85		88	83		99	
TTPS	93	91		83	99		
	MAP			Probabilistic			

Figure 7.24: DICE coefficient of the dose binarized with a 40Gy threshold for the different scenarios: using only one time point (OTP), using two time points (TTP), using two time points and the segmentation uncertainty (TTPS). The DICE coefficient is presented for the MAP doses (Left) and probabilistic doses (Right), and for the prescription doses (light blue) and the IMRT doses (light pink). One can note that the TTP and TTPS scenarios are the closest, and that the IMRT optimization reduces the differences between the doses.

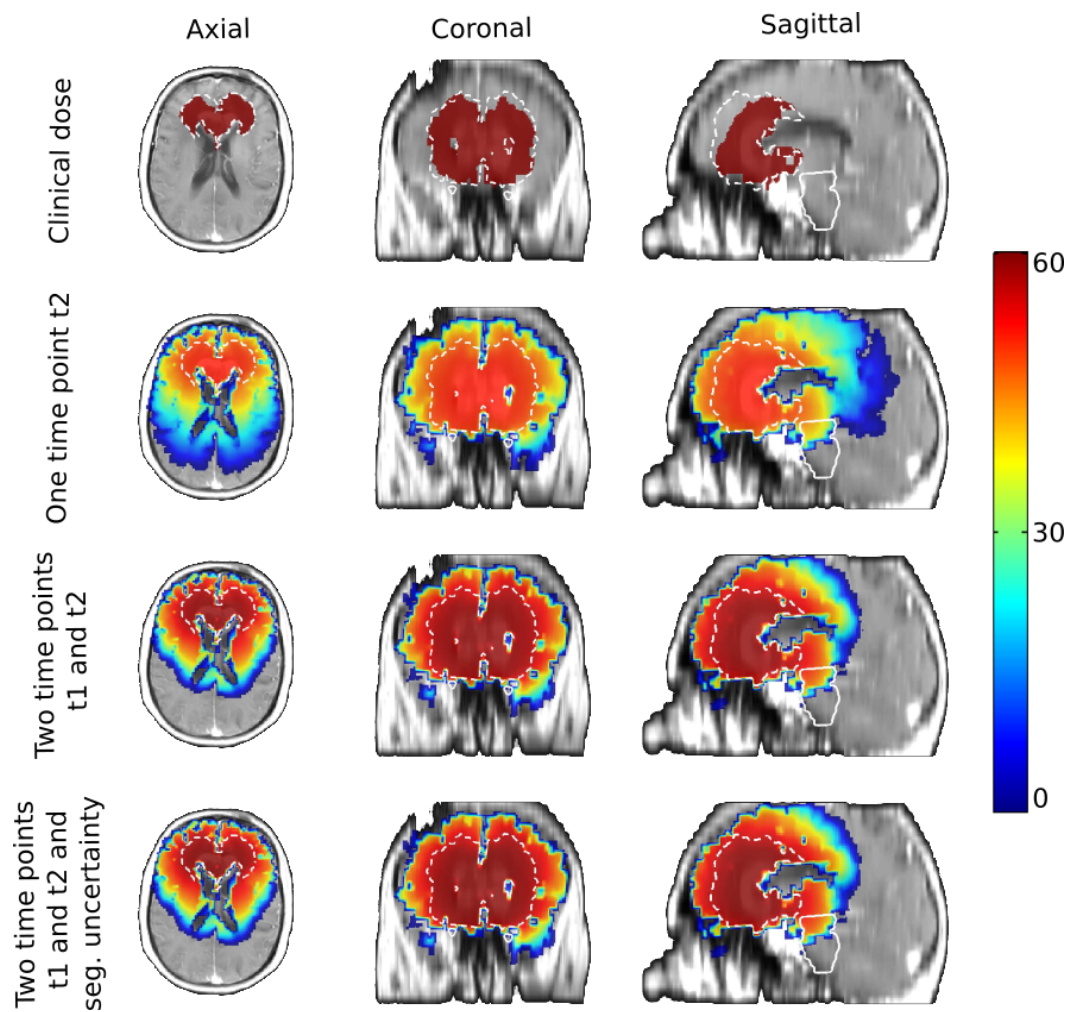


Figure 7.20: Prescription MAP doses in Gray for the clinical plan and the three different personalized plans. From top to bottom: clinical plan, using only the second time point, using the two time points, using the two time points and the segmentation uncertainty. From left to right: axial, coronal, and sagittal views.

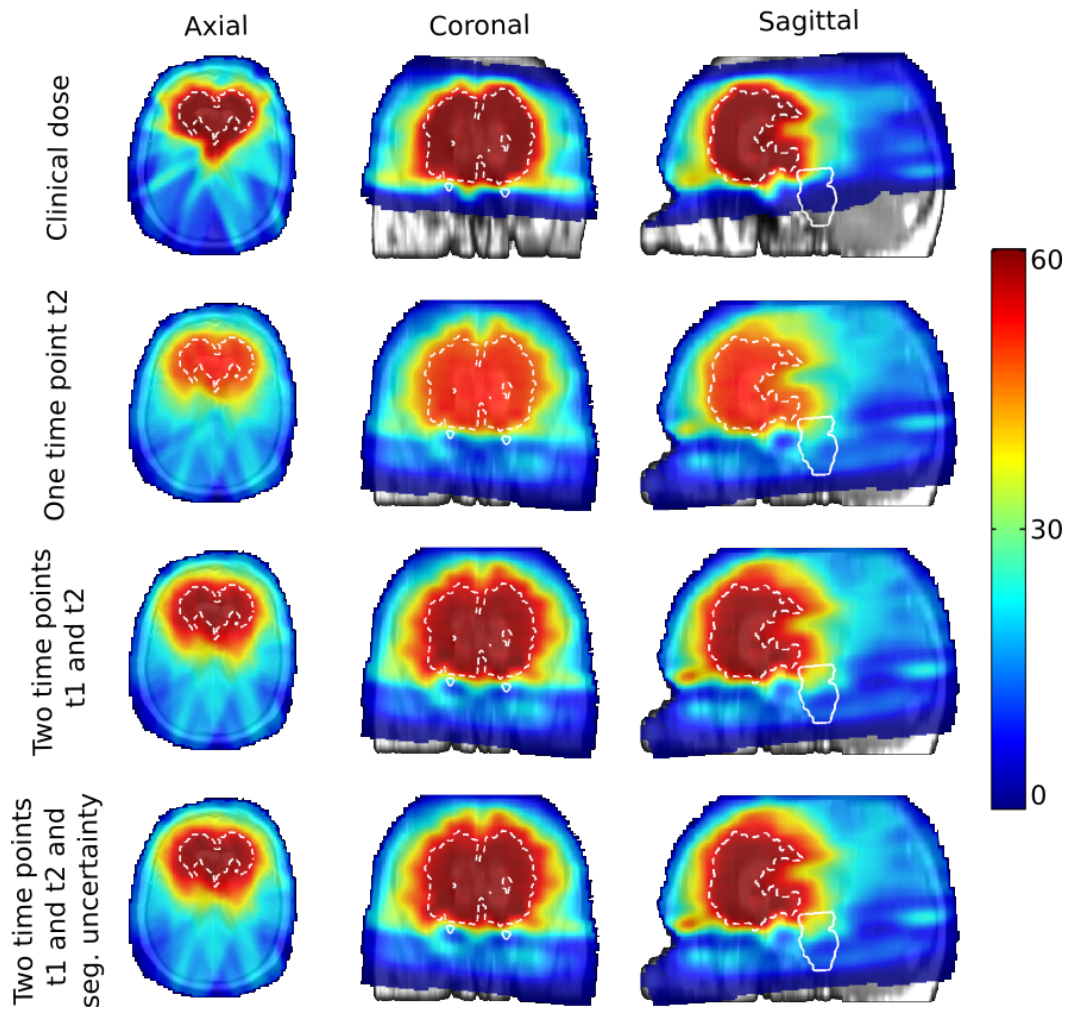


Figure 7.21: IMRT MAP doses in Gray for the clinical plan and the three different personalized plans. From top to bottom: clinical plan, using only the second time point, using the two time points, using the two time points and the segmentation uncertainty. From left to right: axial, coronal, and sagittal views.

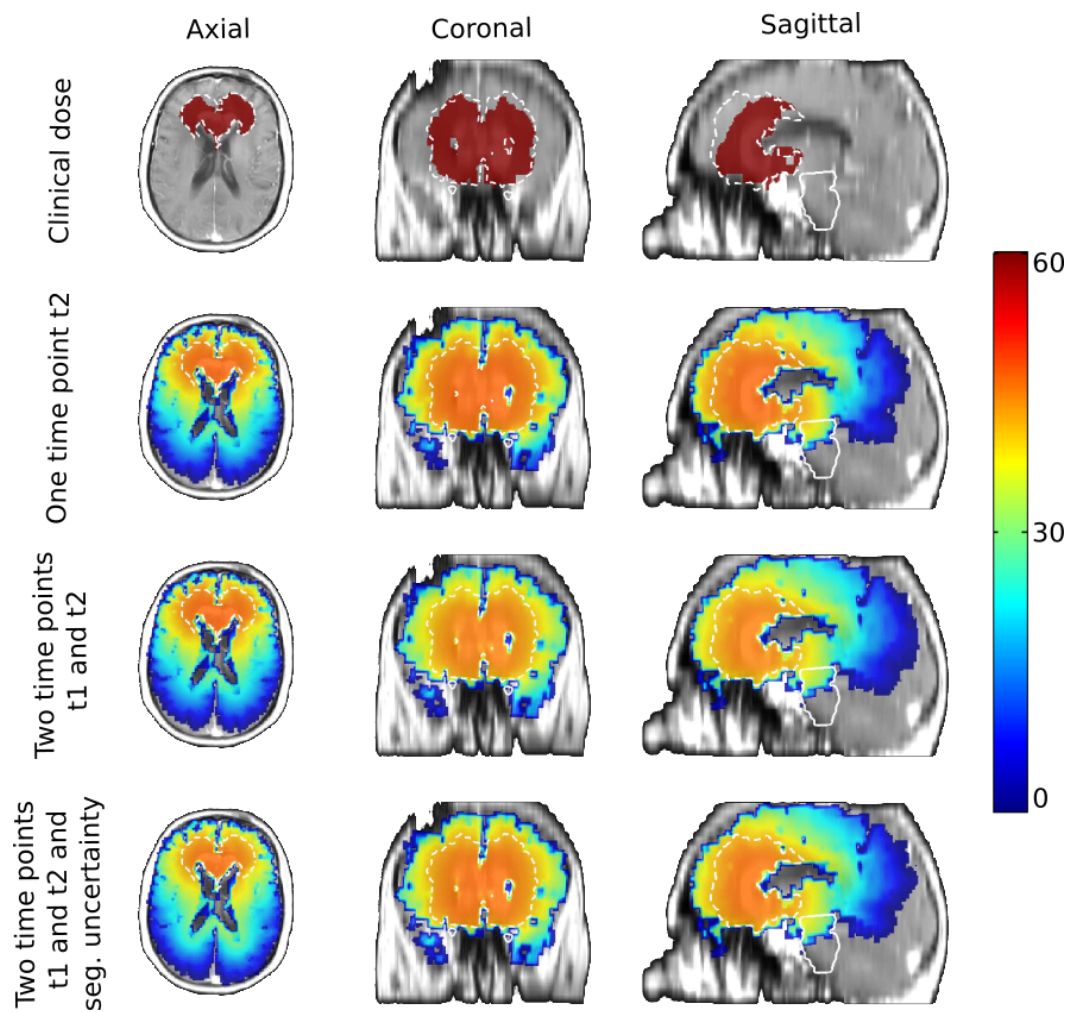


Figure 7.22: Prescription probabilistic doses in Gray for the clinical plan and the three different personalized plans. From top to bottom: clinical plan, using only the second time point, using the two time points, using the two time points and the segmentation uncertainty. From left to right: axial, coronal, and sagittal views.

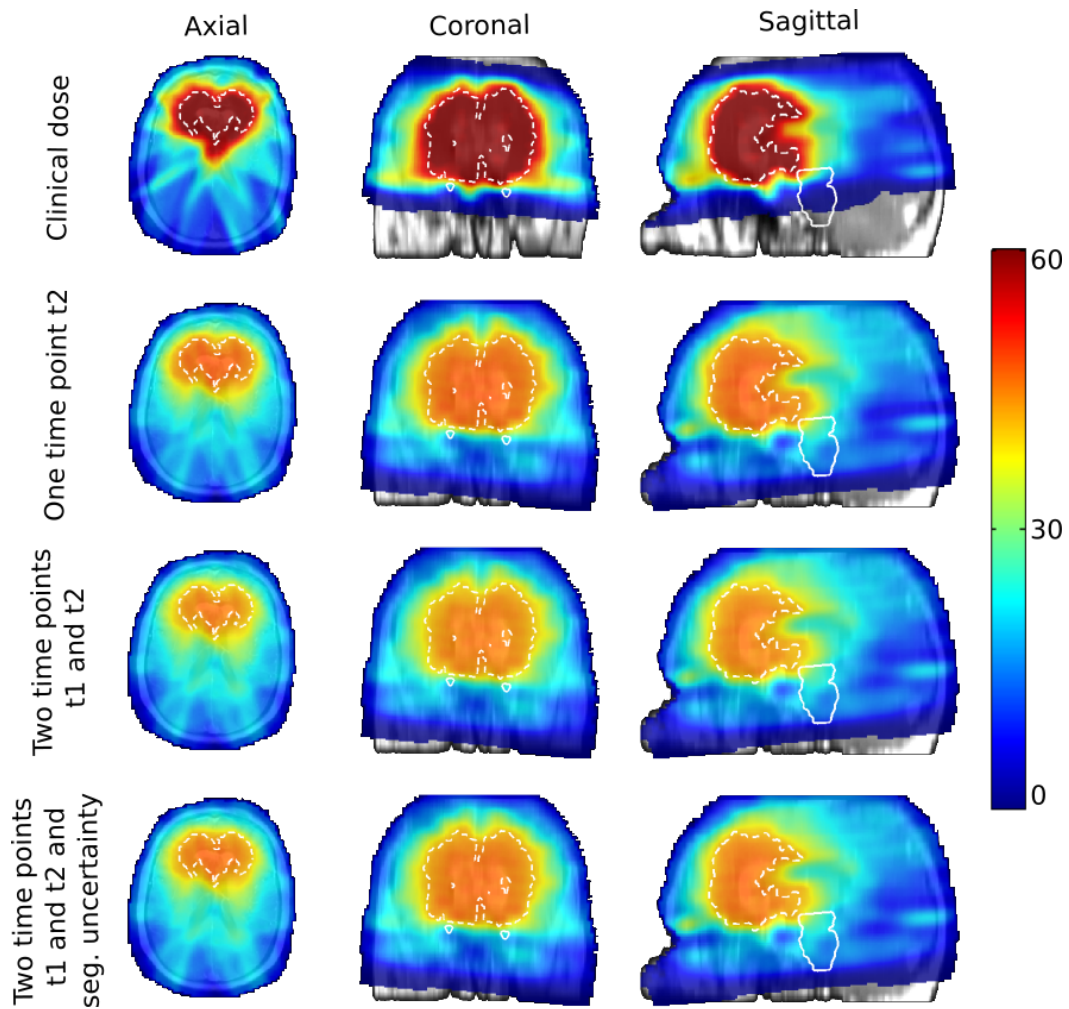


Figure 7.23: IMRT probabilistic doses in Gray for the clinical plan and the three different personalized plans. From top to bottom: clinical plan, using only the second time point, using the two time points, using the two time points and the segmentation uncertainty. From left to right: axial, coronal, and sagittal views.

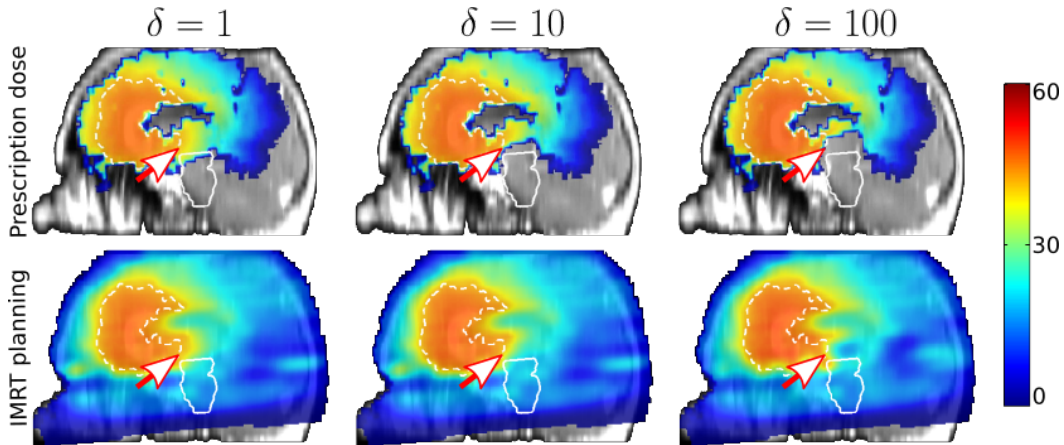


Figure 7.25: Prescription (Top) and IMRT (Bottom) doses in Gray for increasing values of δ (from left to right). We can see that with increasing δ , the dose around the brainstem is re-distributed. The arrows indicate the parts of the brain where the dose is re-distributed.

7.8 Conclusion

We presented a method to combine a computational model of tumor growth and a dose response model in order to optimize radiotherapy planning, which takes into account the uncertainty in the model parameters and the clinical segmentations. We presented and compared three different scenarios. In the first one, we only consider one MRI acquisition before therapy, as it would usually be the case in clinic. In the second one, we use two time points in order to personalize the model and plan radiotherapy. In the third one, we include the uncertainty in the segmentation process. Based on those different scenarios, we proposed three principled approaches in order to define patient specific dose planning, and discussed the difference between them. The MAP dose minimizes surviving tumor cells after irradiation of the most probable situation, while the probabilistic dose allows to take into account the uncertainty by minimizing the expected surviving tumor cells. The proposed density are automatically conformal to the T1Gd and T2-FLAIR abnormalities. We showed that including a second time point increased the uncertainty in the invisibility index and resulted in less peaked probabilistic doses. However, the difference between the prescription doses are partly smoothed out by the IMRT optimization. We also showed that including the uncertainty in the segmentation did not change the results much. We also proposed a proof-of-concept method in order to redistribute the dose to take into account the uncertainty in the tumor cell density, and the presence of neighboring OARs such as the brainstem. We believe that this method could be beneficial in risky situations, when the tumor is close to an organ at risk.

In the future, the inclusion of the fractionation scheme of the delivered dose could be optimized. In this case, the personalization on two different time points before therapy would be crucial in order to estimate the speed of growth of the tumor, and

simulate its progression during radiotherapy. The impact of the presented planning should also be further investigated on a larger cohort of patients. To that end, the model should be further extended in order to take into account the complex therapy the patient is undergoing. As such, the model could be applied to any presented patient given the therapy schedule. Finally, in order to make the personalization of the prescription dose more impactful on the delivered dose, one could use more conformal dose delivery techniques such as proton therapy.

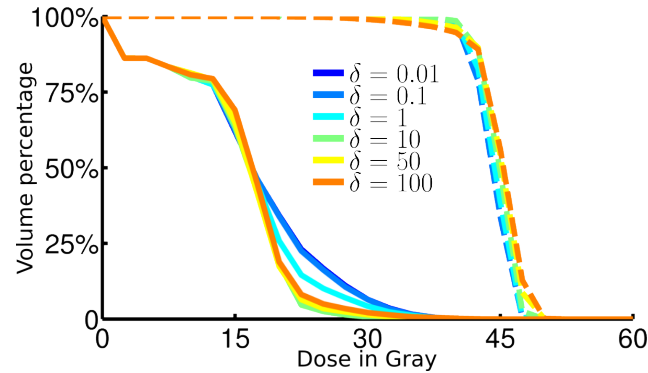


Figure 7.26: Dose volume histogram for the brainstem (solid lines) and the target volume T (dashed lines) for different values of δ . The x axis is the dose and the y axis is the percentage of volume targeted with this dose. Increasing the value of δ reduces the dose delivered to the brainstem while keeping the dose delivered to the target volume T approximately constant.

Conclusion and Perspectives

Contents

8.1	Main Contributions	111
8.1.1	Analysis of the Vasogenic Edema	111
8.1.2	Segmentation Sampling for Uncertainty Quantification	112
8.1.3	Bayesian Personalization of a Tumor Growth Model	112
8.1.4	Personalized Radiotherapy Planning	113
8.2	Perspectives	113
8.2.1	Segmentation Sampling	113
8.2.2	Imaging Gliomas	113
8.2.3	Tumor Growth Model Improvements	114
8.2.4	Personalization Strategies	114
8.2.5	Dose Response Model Improvements	114

The main objective of this thesis was the development of tools in order to personalize radiotherapy planning based on computational models of tumor growth. To that end, we investigated the relationship between the available images and the radiotherapy plan, the uncertainty in the tumor segmentation, the personalization of a tumor growth model, and its combination with a dose response model to automatically define patient-specific radiotherapy planning. In this chapter, we summarize the main contributions of our work, and detail the perspectives which should be the topic of future research.

8.1 Main Contributions

8.1.1 Analysis of the Vasogenic Edema

In current practice, radiotherapy planning is primarily based upon T2 FLAIR MRI despite its known lack of specificity in the detection of tumor infiltration. While hyperintensity on T2 FLAIR is widely considered to represent infiltrative tumor, it may also be caused by the presence of vasogenic edema. We investigated if multi-modal MR imaging can identify vasogenic edema prior to radiotherapy [Lê et al., 2014]. In our approach, the distance from the contrast enhancing tumor is the single best feature to segment the vasogenic edema, reflecting the observation that for most patients, infiltrative tumor is adjacent to the T1Gd abnormality. We showed

how excluding the vasogenic edema - which does not necessarily harbor tumor cells - from the radiotherapy target delineation would enable reduction in target volumes, with the potential of exposing less radiation to surrounding normal brain tissue.

8.1.2 Segmentation Sampling for Uncertainty Quantification

Medical image segmentation is probably the task most often required in computer aided diagnosis or therapy planning and guidance. Due to its ill-posed nature, the quantification of segmentation accuracy and uncertainty is crucial to assess the overall performance of other applications. Usually, this uncertainty is assessed by estimating inter-expert variability on a few cases, but it cannot be applied on large databases due to the amount of resources required. We presented an original image segmentation sampling framework to generate plausible segmentations close to an input one [Lê et al., 2015b, Lê et al., 2016]. The approach leads to spatially smooth contours which take into account the presence of salient features of the region of interest in the image. Samples are efficiently generated, with a variability around a reference segmentation easily controlled by a single scalar. Several extensions have been proposed such as the sampling of several neighboring structures, taking into account under and over segmentation with a simple scalar parameter, and forcing the inclusion or the exclusion of certain part of the image from the samples. We provide a method to apply this sampling method to more general non-stationary covariance functions using supervoxels.

8.1.3 Bayesian Personalization of a Tumor Growth Model

Estimating the parameters of a tumor growth model is difficult because of the lack of identifiability of the parameters, the uncertainty in the tumor segmentations, and the model approximation, which cannot perfectly capture the complex dynamics of the tumor evolution. We presented an approach to analyze the uncertainty in the patient specific parameters of a reaction-diffusion tumor growth model, by sampling from the posterior probability of the parameters knowing the magnetic resonance images of a given patient [Lê et al., 2015a, Le et al., 2016]. Our method is based on an efficient implementation of the reaction-diffusion equation based on the Lattice Boltzmann Method, and a high acceptance rate Monte Carlo technique called Gaussian Process Hamiltonian Monte Carlo. We compared this personalization approach with two commonly used approaches based on the spherical asymptotic analysis of the reaction-diffusion model, and on a derivative-free optimization algorithm. We demonstrated the performance of the method on synthetic data, and on seven patients with a glioblastoma. This Bayesian personalization produces more informative results. In particular, it provides samples from the regions of interest and highlights the presence of several modes for some patients. In contrast, previous approaches based on optimization strategies fail to reveal the presence of different modes, and correlation between parameters.

8.1.4 Personalized Radiotherapy Planning

We presented a method to combine a computational model of tumor growth and a dose response model in order to optimize radiotherapy planning, which takes into account the uncertainty in the model parameters and the clinical segmentations. We presented and compared three different scenarios. In the first one, we only consider one MRI acquisition before therapy, as it would usually be the case in clinic. In the second one, we use two time points in order to personalize the model and plan radiotherapy. In the third one, we include the uncertainty in the segmentation process. Based on those different scenarios, we proposed three principled approaches in order to define patient specific dose planning, and discussed the difference between them. The MAP dose minimizes surviving tumor cells after irradiation of the most probable situation, while the probabilistic dose allows to take into account the uncertainty by minimizing the expected surviving tumor cells. The proposed density are automatically conformal to the T1Gd and T2-FLAIR abnormalities. We showed that including a second time point increased the uncertainty in the invisibility index and resulted in more shallow probabilistic doses. However, the difference between the prescription doses are partly smoothed out by the IMRT optimization. We also showed that including the uncertainty in the segmentation did not change the results much. We also proposed a proof-of-concept method in order to redistribute the dose to take into account the uncertainty in the tumor cell density, and the presence of neighboring OARs such as the brainstem. We believe that this method could be beneficial in more risky situations, for instance when the tumor is close to the cochlea.

8.2 Perspectives

8.2.1 Segmentation Sampling

The segmentation sampling method proposed in Chapter 5 could have several additional applications. For instance, it could be used in order to produce consensus segmentations from several expert ones. Indeed, the probabilistic model could be reversed in order to assume that several expert segmentations are samples from a "real" latent segmentation. Algorithms such as expectation-maximization could then be used to compute the consensus. However, this is currently limited because we only observe a single contour of the hypothesized level-set. Moreover, the proposed algorithm could be used in order to assess the confidence of the performance of segmentation algorithms in the context of segmentation challenges, by providing several likely segmentations around the ground truth segmentations.

8.2.2 Imaging Gliomas

The study of less conventional MR modalities could be beneficial to study the vasogenic edema and improve the tumor growth model. It was noted on the study

of the vasogenic edema that the T1Gd and T2-FLAIR MRI are not always predictors of the presence of tumor cells. Other MRI modalities such as spectroscopic or PET images are better predictors for the presence of tumor cells. However, these modalities are not as standard in clinical settings. Moreover, spectroscopic images currently present very coarse resolutions which do not make them easily usable in our case.

8.2.3 Tumor Growth Model Improvements

The proposed reaction-diffusion model is a fairly simple one which could be improved in several ways. First, the mass effect of the tumor could be explicitly modeled [Clatz et al., 2005, Hoge et al., 2008]. This would avoid registering the images which is a source of uncertainty. Second, the observed heterogeneity of the tumor could be explicitly modeled using for instance a multi-compartment model as presented in Chapter 3. Third, the model could include the impact of different kinds of therapy, such as chemotherapy [Tracqui et al., 1995]. This would allow one to apply the model to any patient given the applied therapy. Related to Section 8.2.2, the model should be extended in order to take into account other imaging modalities. This could be done either by providing the information coming from the additional MR images to the model, or by modifying the likelihood in order to include them. Although the reaction-diffusion model of tumor growth and the linear-quadratic dose response model are fairly standard, further validation should be investigated. This could be attained by comparing personalized models on large cohort of patient with histologic slices, or more specific MR such as spectroscopic images.

8.2.4 Personalization Strategies

The proposed personalization strategy is agnostic to the used model. As such, model extension should not pose any problem to the personalization method. However, the extension of the model could increase the dimension of the problem with additional parameters. This would require a more thorough initialization in order to have enough information to build a reasonable proposal function for the Monte Carlo algorithm. Moreover, extending the model could make it computationally heavier. Methods based on surrogate or reduced order models could be adapted to be apply in the proposed framework [Konukoglu et al., 2011, Menze et al., 2011a].

8.2.5 Dose Response Model Improvements

There is a vast body of work on trying to understand the microscopic effect of the delivered dose to the different tissues depending on their type, location, vascularization,... These different aspects could be included in the dose response model in order to more finely define the prescription dose. Moreover, the effect of dose fractions should be further investigated. Finally, in order to make the personalization of the prescription dose more impactful on the delivered dose, one could use more conformal dose delivery techniques such as proton therapy.

List of Publications

Contents

9.1	First Author	115
9.2	Co-author	116
9.3	Invited Talks	116
9.4	Challenge Participation	117
9.5	Award	117

The presented work lead to several published and submitted publications.

9.1 First Author

Journal Papers

- [Lê et al., 2016]
Lê, Matthieu and Unkelbach, Jan and Ayache, Nicholas and Delingette, Hervé. "Sampling Image Segmentations for Uncertainty Quantification." Elsevier Medical Image Analysis (2016).
- [Le et al., 2016]
Lê, Matthieu and Delingette, Hervé and Kalpathy-Cramer, Jayashree and Gerstner, Elisabeth and Batchelor, Tracy and Unkelbach, Jan and Ayache, Nicholas. "MRI Based Bayesian Personalization of a Brain Tumor Growth Model." IEEE Transactions on Medical Imaging (2016).
- Submitted to IEEE Transactions on Medical Imaging,
Lê, Matthieu and Delingette, Hervé and Kalpathy-Cramer, Jayashree and Gerstner, Elisabeth and Batchelor, Tracy and Unkelbach, Jan and Ayache, Nicholas. "Personalized Radiotherapy Planning Based on a Computational Tumor Growth Model: A Case Study."

Peer-Reviewed Conference and Workshop Papers

- [Lê et al., 2014]
Lê, Matthieu and Delingette, Hervé and Kalpathy-Cramer, Jayashree and Gerstner, Elisabeth and Shih, Helen A. and Batchelor, Tracy and Unkelbach, Jan and Ayache, Nicholas. "Multimodal Analysis of Vasogenic Edema

in Glioblastoma Patients for Radiotherapy Planning." *In MICCAI Workshop Image-Guided Adaptive Radiation Therapy 2014*.

- [Lê et al., 2015b]
Lê, Matthieu and Unkelbach, Jan and Ayache, Nicholas and Delingette, Hervé. "GPSSI: Gaussian Process for Sampling Segmentations of Images." *In Medical Image Computing and Computer-Assisted Intervention–MICCAI 2015*. Springer International Publishing, 2015. 38-46..
- [Lê et al., 2015a]
Lê, Matthieu and Delingette, Hervé and Kalpathy-Cramer, Jayashree and Gerstner, Elisabeth and Batchelor, Tracy and Unkelbach, Jan and Ayache, Nicholas. "Bayesian Personalization of Brain Tumor Growth Model." *In Medical Image Computing and Computer-Assisted Intervention–MICCAI 2015*. Springer International Publishing, 2015. 424-432.

9.2 Co-author

Journal Papers

- [Unkelbach et al., 2014b]
Unkelbach, Jan and Menze, Bjoern H. and Konukoglu, Ender and Dittmann, Florian and Lê, Matthieu and Ayache, Nicholas and Shih, Helen A. "Radiotherapy planning for glioblastoma based on a tumor growth model: improving target volume delineation." *Physics in medicine and biology* 59, no. 3 (2014): 747.
- Accepted with minor revisions to IEEE Transactions on Medical Imaging, Cordier, Nicolas and Delingette, Hervé and Lê, Matthieu and Ayache, Nicholas. "Extended Modality Propagation: Image Synthesis of Pathological Cases."

9.3 Invited Talks

- Matthieu Lê, Brain tumor growth modeling and application to radiotherapy planning. *GDR METICE: Mathématiques appliquées aux espèces, tissus et cellules, November, 20th, 2014, Paris, France*.
- Matthieu Lê, Bayesian personalization of tumor growth model. *ICTM15: International Workshop on Intracranial Tumors Modeling, September, 22nd, 2015, Bordeaux, France*.

9.4 Challenge Participation

I participated in the MICCAI 2014 Machine Learning Challenge where I ranked second in the classification challenge using a method based on the Bolasso [Bach, 2008].

9.5 Award

MICCAI Young Scientist Award 2015 for the paper:

Lê, Matthieu and Unkelbach, Jan and Ayache, Nicholas and Delingette, Hervé. "GPSSI: Gaussian Process for Sampling Segmentations of Images." *In Medical Image Computing and Computer-Assisted Intervention–MICCAI 2015*. Springer International Publishing, 2015. 38-46.

Complex Tumor Growth Model Implementation

I describe the numerical scheme used for the implementation of the multi-compartment model, which is based on coupled reaction-diffusion equations with transitions between the different types of cells. The method is presented in the one dimensional case. The extension to 3 dimensions is straightforward.

A.1 Diffusion

Consider the diffusion equation,

$$\frac{\partial u}{\partial t} = \nabla \cdot (D \nabla u) \tag{A.1}$$

where u is the considered cell density, and D is the diffusion coefficient. The solution u of the equation is discretized on a $\Delta x \times \Delta t$ lattice at location $x = i$ and time $t = n$,

$$u_i^n = u(i\Delta x, n\Delta t) \tag{A.2}$$

The time derivative on the left-hand side of equation A.1 is discretized with a forward scheme. The interior derivative of the right-hand side is discretized with a first order centered Crank-Nicolson. The exterior derivative of the right-hand side is discretized with a first order centered scheme.

$$\begin{aligned}
\left. \frac{\partial u}{\partial t} \right|_i^n &= \frac{u_i^{n+1} - u_i^n}{\Delta t} \\
\nabla \cdot (D\nabla u)|_i^n &= \nabla \cdot \left(\frac{1}{2} \left(D_i^n \frac{u_{i+\frac{1}{2}}^n - u_{i-\frac{1}{2}}^n}{\Delta x} + D_i^{n+1} \frac{u_{i+\frac{1}{2}}^{n+1} - u_{i-\frac{1}{2}}^{n+1}}{\Delta x} \right) \right) \\
&= \frac{1}{2} \frac{D_{i+\frac{1}{2}}^n \frac{u_{i+1}^n - u_i^n}{\Delta x} - D_{i-\frac{1}{2}}^n \frac{u_i^n - u_{i-1}^n}{\Delta x}}{\Delta x} \\
&\quad + \frac{1}{2} \frac{D_{i+\frac{1}{2}}^{n+1} \frac{u_{i+1}^{n+1} - u_i^{n+1}}{\Delta x} - D_{i-\frac{1}{2}}^{n+1} \frac{u_i^{n+1} - u_{i-1}^{n+1}}{\Delta x}}{\Delta x}
\end{aligned}$$

Rearranging the equation, we get,

$$\begin{aligned}
u_{i+1}^{n+1} \left(\frac{D_{i+\frac{1}{2}}^{n+1}}{2\Delta x^2} \right) + u_i^{n+1} \left(-\frac{1}{\Delta t} - \frac{D_{i+\frac{1}{2}}^{n+1} + D_{i-\frac{1}{2}}^{n+1}}{2\Delta x^2} \right) + u_{i-1}^{n+1} \left(\frac{D_{i-\frac{1}{2}}^{n+1}}{2\Delta x^2} \right) = \\
u_{i+1}^n \left(-\frac{D_{i+\frac{1}{2}}^n}{2\Delta x^2} \right) + u_i^n \left(-\frac{1}{\Delta t} + \frac{D_{i+\frac{1}{2}}^n + D_{i-\frac{1}{2}}^n}{2\Delta x^2} \right) + u_{i-1}^n \left(-\frac{D_{i-\frac{1}{2}}^n}{2\Delta x^2} \right) \quad (\text{A.3})
\end{aligned}$$

which is a linear problem of the form

$$B\mathbf{u}^{n+1} = f(u^n) \quad (\text{A.4})$$

The geometric mean is used to compute $D_{i+\frac{1}{2}}$,

$$D_{i+\frac{1}{2}} = 2 \frac{D_i D_{i+1}}{D_i + D_{i+1}} \quad (\text{A.5})$$

Neumann boundary conditions are enforced by setting a null diffusion outside of the brain domain.

Note that discretizing after computing the derivatives leads to an unstable numerical scheme in the presence of steep diffusion. Moreover, the arithmetic mean

$$D_{i+\frac{1}{2}} = \frac{D_i + D_{i+1}}{2} \quad (\text{A.6})$$

is not accurate enough: it lets the cell density u leak into the non-zero diffusion domain.

A.2 Proliferation

Consider the proliferation equation.

$$\frac{\partial P}{\partial t} = \rho P(1 - T) \quad (\text{A.7})$$

This equation is solved using an explicit Euler scheme, using previous notations,

$$P_i^{n+1} = P_i^n + \Delta t \rho P_i^n (1 - T_i^n) \quad (\text{A.8})$$

A.3 Transitions

Consider the transition equations between cells,

$$\frac{\partial P}{\partial t} = -\lambda_{P \rightarrow Q} P - \lambda_{P \rightarrow N} P + \lambda_{Q \rightarrow P} Q \quad (\text{A.9})$$

$$\frac{\partial Q}{\partial t} = -\lambda_{Q \rightarrow P} Q - \lambda_{Q \rightarrow N} Q + \lambda_{P \rightarrow Q} P \quad (\text{A.10})$$

$$\frac{\partial N}{\partial t} = \lambda_{P \rightarrow N} P + \lambda_{Q \rightarrow N} Q \quad (\text{A.11})$$

Using an exponential scheme, we have

$$\begin{pmatrix} P_i^{n+1} \\ Q_i^{n+1} \\ N_i^{n+1} \end{pmatrix} = \begin{pmatrix} P_i^n \\ Q_i^n \\ N_i^n \end{pmatrix} \exp(\Delta t A) \quad (\text{A.12})$$

where $A = \begin{pmatrix} -\lambda_{P \rightarrow Q} - \lambda_{P \rightarrow N} & \lambda_{Q \rightarrow P} & 0 \\ \lambda_{P \rightarrow Q} & -\lambda_{Q \rightarrow P} - \lambda_{Q \rightarrow N} & 0 \\ \lambda_{P \rightarrow N} & \lambda_{Q \rightarrow N} & 0 \end{pmatrix}$

The exponential scheme ensures that the cell density are always positive.

A.4 Vascularization

Consider the vascularization equation,

$$\frac{\partial V}{\partial t} = \alpha P(1 - V) - \beta NV \quad (\text{A.13})$$

$$(\text{A.14})$$

The time derivative is discretized using a forward scheme,

$$\frac{\partial V}{\partial t} = \frac{V_i^{n+1} - V_i^n}{\Delta t} \quad (\text{A.15})$$

and a Crank-Nicolson scheme is used for the right-hand side of the equation,

$$\begin{aligned} & [\alpha P(1 - V) - \beta N V]_i^n = \\ & \alpha P - \frac{V_i^n + V_i^{n+1}}{2} (\alpha P + \beta N) \end{aligned} \quad (\text{A.16})$$

Then, we can get,

$$V_i^{n+1} = \frac{V_i^n + \Delta t \left(\alpha P - \frac{V_i^n}{2} (\alpha P + \beta N) \right)}{1 + \Delta t \frac{\alpha P + \beta N}{2}} \quad (\text{A.17})$$

A.5 Algorithm

The final algorithm to solve the multi-compartment model is as follow:

1. Solve for the diffusion of the proliferative and quiescent cells.
2. Solve for the proliferation of the proliferative cells.
3. Solve for the transition between the proliferative, quiescent, and necrotic cells.
4. Solve for the vascularization.

Lattice Boltzmann Method

B.1 Reaction-Diffusion Equation

The reaction-diffusion equation with Neumann boundary condition can be written as follow,

$$\frac{\partial u}{\partial t} = \underbrace{\nabla(D \cdot \nabla u)}_{\text{Diffusion}} + \underbrace{\rho u(1-u)}_{\text{Logistic Proliferation}} \quad (\text{B.1})$$

$$D \nabla u \cdot \vec{n}_{\partial\Omega} = 0 \quad (\text{B.2})$$

Equation (B.1) describes the spatio-temporal evolution of the tumor cell density u , which infiltrates neighboring tissues with a diffusion tensor D , and proliferates with a net proliferation rate ρ . Equation (B.2) enforces Neumann boundary conditions on the brain domain Ω . In our case, the diffusion tensor is defined as $D = d_g \mathbb{I}$ in the gray matter and $D = d_w \mathbb{I}$ in the white matter, with $\mathbb{I} \in \mathbb{R}^{3 \times 3}$.

B.2 The Lattice Boltzmann Method

The reaction-diffusion equation is solved using the Lattice Boltzmann Method (LBM). The method was described in [Yoshida and Nagaoka, 2010]. It was successfully applied to cardiac electrophysiology [Rapaka et al., 2012], and liver tumor resection [Audigier et al., 2013]. We use the Neumann boundary condition described in [Yu et al., 2003] and [Bouzidi et al., 2001]. The chosen algorithm is called the multiple-relaxation-time (MRT) method, which can be used for anisotropic diffusion coefficient.

In the LBM, the scalar of interest u is projected along the considered velocity directions $\{e_\alpha\}$ such that $u = \sum_\alpha u_\alpha$. The D3Q7 (see Figure B.1) scheme refers to the 3D case with 7 velocity directions $\{e_\alpha\}_{\alpha=0}^6$,

$$[e_0, e_1, e_2, e_3, e_4, e_5, e_6,] = \begin{bmatrix} 0 & 1 & -1 & 0 & 0 & 0 & 0 \\ 0 & 0 & 0 & 1 & -1 & 0 & 0 \\ 0 & 0 & 0 & 0 & 0 & 1 & -1 \end{bmatrix} \quad (\text{B.3})$$

The weight vector

$$w = \{w_\alpha\}_{\alpha=0}^6 = \left[\frac{1}{4} \quad \frac{1}{8} \quad \frac{1}{8} \quad \frac{1}{8} \quad \frac{1}{8} \quad \frac{1}{8} \quad \frac{1}{8} \right] \quad (\text{B.4})$$

is defined according to the connectivity of the grid. The algorithm is made of 4 steps :

1. Initialization

$$u_i = w_i u \quad (\text{B.5})$$

2. Collision

$$u_i^* = u_i - A_{i,j} u_j + \Delta t w_i \rho u (1 - u) \quad (\text{B.6})$$

where $A = M^{-1} S M \in \mathbb{R}^{7 \times 7}$ is the collision matrix. M projects a vector on the moment space, and S is the relaxation time matrix,

$$M = \begin{pmatrix} 1 & 1 & 1 & 1 & 1 & 1 & 1 \\ 0 & 1 & -1 & 0 & 0 & 0 & 0 \\ 0 & 0 & 0 & 1 & -1 & 0 & 0 \\ 0 & 0 & 0 & 0 & 0 & 1 & -1 \\ 6 & -1 & -1 & -1 & -1 & -1 & -1 \\ 0 & 2 & 2 & -1 & -1 & -1 & -1 \\ 0 & 0 & 0 & 1 & 1 & -1 & -1 \end{pmatrix} \quad (\text{B.7})$$

(B.8)

$$S^{-1} = \begin{pmatrix} \tau_0 & 0 & 0 & 0 & 0 & 0 & 0 \\ 0 & \tau_{xx} & \tau_{xy} & \tau_{xz} & 0 & 0 & 0 \\ 0 & \tau_{xy} & \tau_{yy} & \tau_{yz} & 0 & 0 & 0 \\ 0 & \tau_{xz} & \tau_{yz} & \tau_{zz} & 0 & 0 & 0 \\ 0 & 0 & 0 & 0 & \tau_4 & 0 & 0 \\ 0 & 0 & 0 & 0 & 0 & \tau_5 & 0 \\ 0 & 0 & 0 & 0 & 0 & 0 & \tau_6 \end{pmatrix} \quad (\text{B.9})$$

with $\tau_{ij} = \frac{1}{2} \delta_{ij} + \frac{\Delta t}{\varepsilon \Delta x^2} D_{ij}$, $\tau_k = 1.33$, $\varepsilon = \frac{1}{4}$ and D is the diffusion tensor.

3. Streaming

$$u_i(x + \Delta x e_i, t + \Delta t) = u_i^*(x, t) \quad (\text{B.10})$$

4. Neumann boundary condition

$$u_{\bar{i}}(x, t + \Delta t) = \frac{1}{2\Delta} u_i(x, t) + \frac{2\Delta - 1}{2\Delta} u_{\bar{i}}(x, t), \quad \text{if } \Delta > \frac{1}{2} \quad (\text{B.11})$$

$$u_{\bar{i}}(x, t + \Delta t) = 2\Delta u_i(x, t) + (1 - 2\Delta) u_{\bar{i}}(x - \Delta x e_i, t), \quad \text{if } \Delta \leq \frac{1}{2} \quad (\text{B.12})$$

where Δ is the distance between the particle and the boundary, which can be approximated with a level set [Yu et al., 2003] (see Figure B.2).

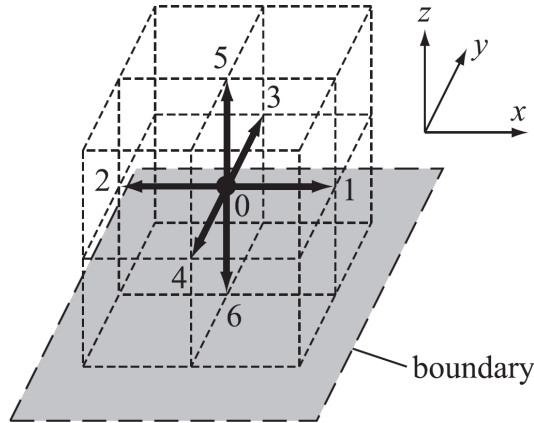


Figure B.1: Illustration of the seven velocity directions used for the D3Q7 LBM scheme. Picture taken from [Yoshida and Nagaoka, 2010].

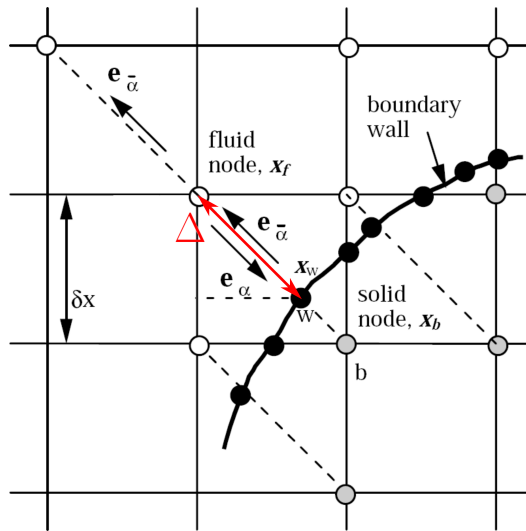


Figure B.2: Layout of the regularly spaced lattices and curved wall boundary. Picture adapted from [Yu et al., 2003]

B.3 Comparison with Analytic Solution

The LBM was checked against the analytic solution of the diffusion equation,

$$\frac{\partial u}{\partial t} = \nabla(D \cdot \nabla u)$$

We set $u_0(r) = u(r, t = 0)$ the initial distribution,

$$u_0(r) = \begin{cases} N_0 & \text{if } r = 0 \\ 0 & \text{else} \end{cases} \tag{B.13}$$

In 3D, the solution of the equation with initial distribution u_0 is

$$u(r, t) = \frac{N_0}{(4\pi Dt)^{\frac{3}{2}}} \exp\left(-\frac{r^2}{4Dt}\right) \quad (\text{B.14})$$

We note $u_D(r, t)$ the solution of Equation (B.3) function of the diffusion coefficient D . For a range of values of D , the LBM simulation was run for 30 days with $\Delta t = 0.1$ day, $\Delta x = 0.5$ mm and $N_0 = 1000$ on a $100 \text{ mm} \times 100 \text{ mm} \times 100 \text{ mm}$ grid with initial distribution $u_D(r, t_0 = 50)$. On ten regularly spaced time points, we compute the validity of the simulation as follows:

1. For each time point, select 50 regularly spaced threshold values between the minimum and the maximum of the tumor.
2. For each time point, for each threshold value, for the simulation and the ground truth, define a binary mask corresponding to the thresholded tumor cell density u . When u is greater than the threshold, the mask is equal to one, when u is lower than the threshold, the mask is equal to zero.
3. Compute the Dice score between the two computed masks.
4. Average the Dice score for the different threshold values and time points.

Figure B.4 (Left) shows the results for different values of D . We can see that the mean value of the Dice score for the different simulations is really good as it never goes below 90%. However, the plotted standard deviation shows that for fairly low ($\approx 10^{-2} \text{ mm}^2 \cdot \text{day}^{-1}$) or high ($\approx 1 \text{ mm}^2 \cdot \text{day}^{-1}$) values of D , the average Dice coefficient minus the standard deviation can decrease to 70%.

We can see on Figure B.3 the results of the 3D simulation for a fairly low value of $D = 0.01 \text{ mm}^2 \cdot \text{day}^{-1}$. The error comes from the peak of the cell density. Indeed, the lower D , the steeper will be the initialization $u_D(r, t_0)$. The value of the cell density computed at the peak is underestimated at the beginning of the simulation, because of the sharpness of the peak. This leads to errors in Dice coefficient in this area. However, we can note that the simulation still leads to good results. The results of the simulation for $D = 0.3 \text{ mm}^2 \cdot \text{day}^{-1}$. The simulation for $D = 0.3$ leads to very good results and it is not distinguishable with the ground truth (Figure B.3). For $D = 1.8 \text{ mm}^2 \cdot \text{day}^{-1}$, the value of the cell density is slightly over-estimated by the simulation at the peak. Moreover, with higher diffusion coefficient value, the boundary begins to have some impact on the difference between the simulation and the ground truth.

Overall, we can see that the simulations are visually extremely close to the analytic solution. The decrease in the Dice coefficient can be explained by some numerical imprecision at the peak, or the very bottom of the distribution. To emphasize this effect, we computed the mean Dice coefficient by excluding the first 10 and the last 10 threshold values ordered from the smallest to the greatest. This means that we focus the study on the front of the cell density, excluding the very

low values of cell density, as well as the values at the peak. We can see on Figure B.4 (Right) that this leads to much better results, for low and high diffusion values. The value of the Dice coefficient minus the standard deviation does not go below 85%.

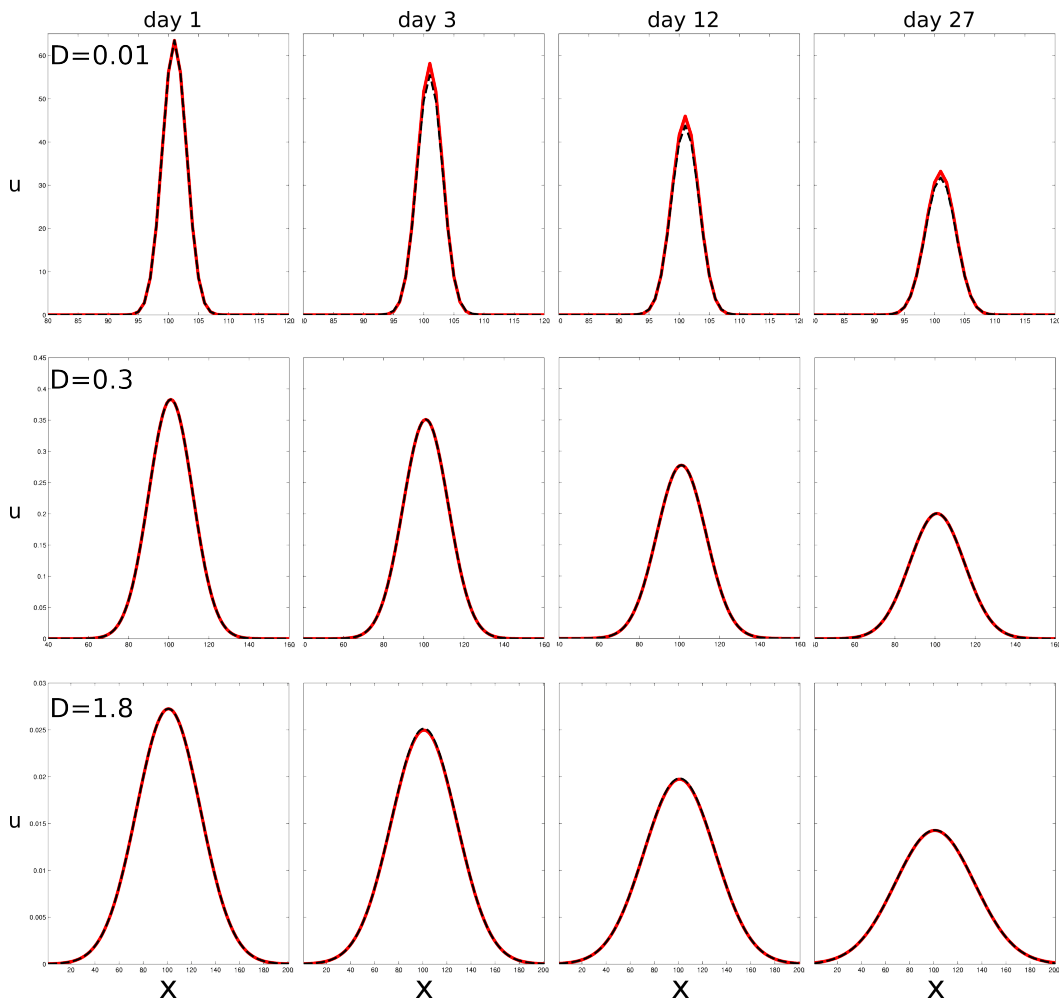


Figure B.3: Simulation (black dashed line) and ground truth (thick red line) for $D = 0.01, 0.3, 1.8 \text{ mm}^2 \cdot \text{day}^{-1}$ (resp. from top to bottom). We show one line extracted from the 3D simulation at the center of cube.

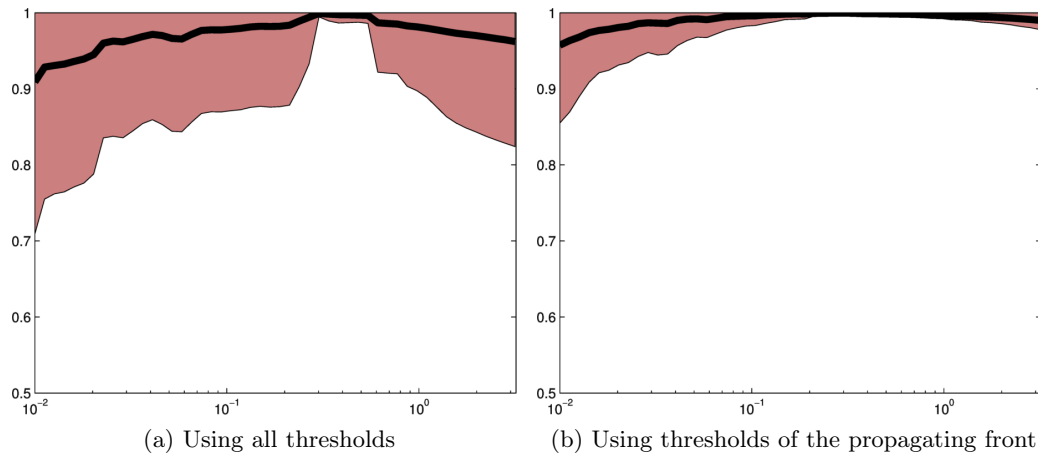


Figure B.4: Mean Dice coefficient function of the diffusion coefficient D (thick black line) using all the thresholds (Left) or the threshold of the propagating front (Right). The red area corresponds to the first mode of variation.

Bibliography

- [Achanta et al., 2012] Achanta, R., Shaji, A., Smith, K., Lucchi, A., Fua, P., and Susstrunk, S. (2012). SLIC superpixels compared to state-of-the-art superpixel methods. *IEEE Transactions on Pattern Analysis and Machine Intelligence*, 34(11):2274–2282. (Cited on page 55.)
- [Andersson et al., 2007] Andersson, J. L., Jenkinson, M., Smith, S., et al. (2007). Non-linear registration, aka spatial normalisation FMRIB technical report TR07JA2. *FMRIB Analysis Group of the University of Oxford*. (Cited on page 68.)
- [Angelini et al., 2007] Angelini, E. D., Clatz, O., Mandonnet, E., Konukoglu, E., Capelle, L., and Duffau, H. (2007). Glioma dynamics and computational models: a review of segmentation, registration, and in silico growth algorithms and their clinical applications. *Current Medical Imaging Reviews*, 3(4):262–276. (Cited on pages 18 and 64.)
- [Audigier et al., 2015] Audigier, C., Mansi, T., Delingette, H., Rapaka, S., Mihalef, V., Carnegie, D., Boctor, E., Choti, M., Kamen, A., Ayache, N., et al. (2015). Efficient lattice Boltzmann solver for patient-specific radiofrequency ablation of hepatic tumors. *IEEE Transactions on Medical Imaging*, 34(7):1576–1589. (Cited on page 69.)
- [Audigier et al., 2013] Audigier, C., Mansi, T., Delingette, H., Rapaka, S., Mihalef, V., Sharma, P., Carnegie, D., Boctor, E., Choti, M., Kamen, A., et al. (2013). Lattice boltzmann method for fast patient-specific simulation of liver tumor ablation from ct images. In *Medical Image Computing and Computer-Assisted Intervention–MICCAI 2013*, pages 323–330. Springer. (Cited on page 123.)
- [Bach, 2008] Bach, F. R. (2008). Bolasso: model consistent lasso estimation through the bootstrap. In *Proceedings of the 25th international conference on Machine learning*, pages 33–40. ACM. (Cited on page 117.)
- [Badoual et al., 2014] Badoual, M., Gerin, C., Deroulers, C., Grammaticos, B., Llitjos, J.-F., Oppenheim, C., Varlet, P., and Pallud, J. (2014). Oedema-based model for diffuse low-grade gliomas: application to clinical cases under radiotherapy. *Cell proliferation*, 47(4):369–380. (Cited on pages 19 and 65.)
- [Betancourt, 2010] Betancourt, M. (2010). Nested sampling with constrained hamiltonian monte carlo. *arXiv preprint arXiv:1005.0157*. (Cited on page 73.)
- [Billy, 2009] Billy, F. (2009). *Modélisation mathématique multi-échelle de l'angiogenèse tumorale. Analyse de la réponse tumorale aux traitements anti-angiogéniques*. PhD thesis, Université Claude Bernard Lyon 1. (Cited on pages 9 and 23.)

- [Bouzidi et al., 2001] Bouzidi, M., Firdaouss, M., and Lallemand, P. (2001). Momentum transfer of a boltzmann-lattice fluid with boundaries. *Physics of Fluids*, 13(11):3452–3459. (Cited on page 123.)
- [Breiman et al., 1984] Breiman, L., Friedman, J., Stone, C. J., and Olshen, R. A. (1984). *Classification and regression trees*. CRC press. (Cited on page 37.)
- [CancerResearchUK, 2014] CancerResearchUK (2014). Brain tumours, In Cancer Research UK. <http://www.cancerresearchuk.org/about-cancer/type/brain-tumour/about/types-of-primary-brain-tumours>. Accessed: 20/09/2014. (Cited on page 5.)
- [Carrabba et al., 2010] Carrabba, G., Mukhopadhyay, D., and Guha, A. (2010). Aberrant signalling complexes in gbms: Prognostic and therapeutic implications. In *Glioblastoma*, pages 95–129. Springer. (Cited on page 5.)
- [Chang and Fisher III, 2011] Chang, J. and Fisher III, J. W. (2011). Efficient MCMC sampling with implicit shape representations. In *IEEE Conference on Computer Vision and Pattern Recognition (CVPR), 2011*, pages 2081–2088. IEEE. (Cited on page 43.)
- [Chaplain, 1996] Chaplain, M. (1996). Avascular growth, angiogenesis and vascular growth in solid tumours: The mathematical modelling of the stages of tumour development. *Mathematical and computer modelling*, 23(6):47–87. (Cited on pages 18 and 64.)
- [Choudhury et al., 2010] Choudhury, S. R., Karmakar, S., Banik, N. L., and Ray, S. K. (2010). Role of angiogenesis in the pathogenesis of glioblastoma and antiangiogenic therapies for controlling glioblastoma. In *Glioblastoma*, pages 217–241. Springer. (Cited on page 7.)
- [Clatz et al., 2005] Clatz, O., Sermesant, M., Bondiau, P., Delingette, H., Warfield, S., Malandain, G., and Ayache, N. (2005). Realistic simulation of the 3D growth of brain tumors in MR images coupling diffusion with biomechanical deformation. *IEEE Transactions on Medical Imaging*, 24(10):1334–1346. (Cited on pages 18, 65 and 114.)
- [Cloughesy et al., 2008] Cloughesy, T., Prados, M., Wen, P., Mikkelsen, T., Abrey, L., Schiff, D., Yung, W., Maoxia, Z., Dimery, I., and Friedman, H. (2008). A phase II, randomized, non-comparative clinical trial of the effect of bevacizumab (BV) alone or in combination with irinotecan (CPT) on 6-month progression free survival (PFS6) in recurrent, treatment-refractory glioblastoma (GBM). *Journal of Clinical Oncology*, 26(15S):2010b. (Cited on page 11.)
- [Coons, 1999] Coons, S. W. (1999). *The gliomas*, chapter Anatomy and growth patterns of diffuse gliomas, pages 210–225. W.B. Saunders Company, Philadelphia, PA, USA. (Cited on pages 1, 5 and 31.)

- [Corwin et al., 2013] Corwin, D., Holdsworth, C., Rockne, R. C., Trister, A. D., Mrugala, M. M., Rockhill, J. K., Stewart, R. D., Phillips, M., and Swanson, K. R. (2013). Toward patient-specific, biologically optimized radiation therapy plans for the treatment of glioblastoma. *PloS one*, 8(11):e79115. (Cited on pages 19, 20, 63, 66, 67, 70, 71 and 83.)
- [Criminisi et al., 2008] Criminisi, A., Sharp, T., and Blake, A. (2008). Geos: Geodesic image segmentation. In *Computer Vision—ECCV 2008*, pages 99–112. Springer. (Cited on page 46.)
- [Cristini and Lowengrub, 2010] Cristini, V. and Lowengrub, J. (2010). *Multiscale modeling of cancer : an integrated experimental and mathematical modeling approach*. Cambridge University Press. (Cited on page 18.)
- [Da Veiga and Marrel, 2012] Da Veiga, S. and Marrel, A. (2012). Gaussian process modeling with inequality constraints. In *Annales de la Faculté des Sciences de Toulouse*, volume 21, pages 529–555. (Cited on page 60.)
- [De Bruijne and Nielsen, 2004] De Bruijne, M. and Nielsen, M. (2004). Image segmentation by shape particle filtering. In *Proceedings of the 17th International Conference on Pattern Recognition, 2004*, volume 3, pages 722–725. IEEE. (Cited on page 43.)
- [DeAngelis, 2001] DeAngelis, L. M. (2001). Brain tumors. *New England Journal of Medicine*, 344(2):114–123. (Cited on pages 6 and 8.)
- [Deasy et al., 2003] Deasy, J. O., Blanco, A. I., and Clark, V. H. (2003). CERR: a computational environment for radiotherapy research. *Medical physics*, 30(5):979–985. (Cited on pages 36 and 90.)
- [Deisboeck and Stamatakos, 2010] Deisboeck, T. and Stamatakos, G. (2010). *Multiscale cancer modeling*, volume 34. CRC Press. (Cited on page 18.)
- [Dietrich and Newsam, 1997] Dietrich, C. and Newsam, G. N. (1997). Fast and exact simulation of stationary gaussian processes through circulant embedding of the covariance matrix. *SIAM Journal on Scientific Computing*, 18(4):1088–1107. (Cited on page 48.)
- [Dittmann et al., 2013] Dittmann, F., Menze, B., Konukoglu, E., and Unkelbach, J. (2013). Use of diffusion tensor images in glioma growth modeling for radiotherapy target delineation. In *Multimodal Brain Image Analysis*, pages 63–73. Springer. (Cited on page 67.)
- [Dolecek et al., 2012] Dolecek, T. A., Propp, J. M., Stroup, N. E., and Kruchko, C. (2012). CBTRUS statistical report: primary brain and central nervous system tumors diagnosed in the united states in 2005–2009. *Neuro-oncology*, 14(suppl 5):v1–v49. (Cited on pages 1, 6, 7 and 64.)

- [Fan et al., 2007] Fan, A. C., Fisher III, J. W., Wells III, W. M., Levitt, J. J., and Willsky, A. S. (2007). MCMC curve sampling for image segmentation. In *Medical Image Computing and Computer-Assisted Intervention–MICCAI 2007*, pages 477–485. Springer. (Cited on page 43.)
- [Gerardo-Castro et al., 2013] Gerardo-Castro, M. P., Peynot, T., and Ramos, F. (2013). Laser-radar data fusion with Gaussian process implicit surfaces. In Corke, P., Mejias, L., and Roberts, J., editors, *The 9th International Conference on Field and Service Robotics*, Brisbane, Australia. (Cited on page 46.)
- [Gibbs, 1998] Gibbs, M. N. (1998). *Bayesian Gaussian processes for regression and classification*. PhD thesis, University of Cambridge. (Cited on page 55.)
- [Gilboa et al., 2015] Gilboa, E., Saatçi, Y., and Cunningham, J. P. (2015). Scaling multidimensional inference for structured gaussian processes. *IEEE Transactions on Pattern Analysis and Machine Intelligence*, 37(2):424–436. (Cited on page 49.)
- [Gooya et al., 2012] Gooya, A., Pohl, K. M., Bilello, M., Cirillo, L., Biros, G., Melhem, E. R., and Davatzikos, C. (2012). GLISTR: glioma image segmentation and registration. *IEEE Transactions on Medical Imaging*, 31(10):1941–1954. (Cited on pages 28 and 66.)
- [Harpold et al., 2007] Harpold, H. L., Alvord Jr, E. C., and Swanson, K. R. (2007). The evolution of mathematical modeling of glioma proliferation and invasion. *Journal of Neuropathology & Experimental Neurology*, 66(1):1–9. (Cited on pages 28, 65, 66, 67, 70, 71, 74 and 93.)
- [Hawkins-Daarud et al., 2013] Hawkins-Daarud, A., Rockne, R. C., Anderson, A., and Swanson, K. R. (2013). Modeling tumor-associated edema in gliomas during anti-angiogenic therapy and its impact on imageable tumor. *Frontiers in oncology*, 3(66.10):3389. (Cited on pages 19 and 65.)
- [Hogea et al., 2008] Hogea, C., Davatzikos, C., and Biros, G. (2008). An image-driven parameter estimation problem for a reaction-diffusion glioma growth model with mass effects. *Journal of mathematical biology*, 56(6):793–825. (Cited on pages 18, 28, 65 and 114.)
- [Holdsworth et al., 2012] Holdsworth, C. H., Corwin, D., Stewart, R. D., Rockne, R., Trister, A. D., Swanson, K. R., and Phillips, M. (2012). Adaptive IMRT using a multiobjective evolutionary algorithm integrated with a diffusion-invasion model of glioblastoma. *Physics in Medicine and Biology*, 57(24):8271. (Cited on page 83.)
- [Iglesias et al., 2011] Iglesias, J. E., Liu, C.-Y., Thompson, P. M., and Tu, Z. (2011). Robust brain extraction across datasets and comparison with publicly available methods. *IEEE Transactions on Medical Imaging*, 30(9):1617–1634. (Cited on page 69.)

- [Jansen et al., 2004] Jansen, M., de Witt Hamer, P. C., Witmer, A. N., Troost, D., and van Noorden, C. J. (2004). Current perspectives on antiangiogenesis strategies in the treatment of malignant gliomas. *Brain research reviews*, 45(3):143–163. (Cited on page 7.)
- [Jbabdi et al., 2005] Jbabdi, S., Mandonnet, E., Duffau, H., Capelle, L., Swanson, K. R., Péligrini-Issac, M., Guillevin, R., and Benali, H. (2005). Simulation of anisotropic growth of low-grade gliomas using diffusion tensor imaging. *Magnetic Resonance in Medicine*, 54(3):616–624. (Cited on page 18.)
- [Jenkinson et al., 2002] Jenkinson, M., Bannister, P., Brady, M., and Smith, S. (2002). Improved optimization for the robust and accurate linear registration and motion correction of brain images. *Neuroimage*, 17(2):825–841. (Cited on page 68.)
- [Jenkinson et al., 2012] Jenkinson, M., Beckmann, C. F., Behrens, T. E., Woolrich, M. W., and Smith, S. M. (2012). FSL. *Neuroimage*, 62(2):782–790. (Cited on page 68.)
- [Kansal et al., 2000] Kansal, A., Torquato, S., Harsh, G., Chiocca, E., and Deisboeck, T. (2000). Simulated brain tumor growth dynamics using a three-dimensional cellular automaton. *Journal of theoretical biology*, 203(4):367–382. (Cited on page 17.)
- [Kelly, 1993] Kelly, P. J. (1993). Computed tomography and histologic limits in glial neoplasms: tumor types and selection for volumetric resection. *Surgical neurology*, 39(6):458–465. (Cited on page 31.)
- [Kinoshita et al., 2012] Kinoshita, M., , Goto, T., Arita, H., Okita, Y., Isohashi, K., Kagawa, N., Fujimoto, Y., Kishima, H., Shimosegawa, E., Saitoh, Y., et al. (2012). Imaging 18F-fluorodeoxy glucose/11C-methionine uptake decoupling for identification of tumor cell infiltration in peritumoral brain edema. *Journal of Neuro-Oncology*, 106(2):417–425. (Cited on page 32.)
- [Konukoglu et al., 2010a] Konukoglu, E., Clatz, O., Bondiau, P.-Y., Delingette, H., and Ayache, N. (2010a). Extrapolating glioma invasion margin in brain magnetic resonance images: suggesting new irradiation margins. *Medical image analysis*, 14(2):111–125. (Cited on pages 58, 69 and 86.)
- [Konukoglu et al., 2010b] Konukoglu, E., Clatz, O., Menze, B., Stieltjes, B., Weber, M., Mandonnet, E., Delingette, H., and Ayache, N. (2010b). Image guided personalization of reaction-diffusion type tumor growth models using modified anisotropic eikonal equations. *IEEE Transactions on Medical Imaging*, 29(1):77–95. (Cited on pages 18, 20, 28, 64, 65, 66, 70 and 72.)
- [Konukoglu et al., 2011] Konukoglu, E., Relan, J., Cilingir, U., Menze, B. H., Chinchapatnam, P., Jadidi, A., Cochet, H., Hocini, M., Delingette, H., Jaïs, P., et al.

- (2011). Efficient probabilistic model personalization integrating uncertainty on data and parameters: Application to Eikonal-diffusion models in cardiac electrophysiology. *Progress in biophysics and molecular biology*, 107(1):134–146. (Cited on pages 28, 66 and 114.)
- [Kozintsev, 1999] Kozintsev, B. (1999). *Computations with Gaussian random fields*. PhD thesis, University of Maryland. (Cited on page 48.)
- [Kozintsev and Kedem, 2000] Kozintsev, B. and Kedem, B. (2000). Generation of similar images from a given discrete image. *Journal of Computational and Graphical Statistics*, 9(2):286–302. (Cited on page 48.)
- [Kristiansen et al., 1981] Kristiansen, K., Hagen, S., Kollevold, T., Torvik, A., Holme, I., Stat, M., Nesbakken, R., Hatlevoll, R., Lindgren, M., Brun, A., et al. (1981). Combined modality therapy of operated astrocytomas grade III and IV. Confirmation of the value of postoperative irradiation and lack of potentiation of bleomycin on survival time: a prospective multicenter trial of the Scandinavian Glioblastoma Study Group. *Cancer*, 47(4):649–652. (Cited on pages 10 and 83.)
- [Lacroix et al., 2001] Lacroix, M., Abi-Said, D., Fourney, D. R., Gokaslan, Z. L., Shi, W., DeMonte, F., Lang, F. F., McCutcheon, I. E., Hassenbusch, S. J., Holland, E., et al. (2001). A multivariate analysis of 416 patients with glioblastoma multiforme: prognosis, extent of resection, and survival. *Journal of neurosurgery*, 95(2):190–198. (Cited on page 9.)
- [Le et al., 2016] Le, M., Delingette, H., Kalpathy-Cramer, J., Gerstner, E., Batchelor, T., Unkelbach, J., and Ayache, N. (2016). Mri based bayesian personalization of a tumor growth model. *IEEE Transactions on Medical Imaging*. (Cited on pages 61, 112 and 115.)
- [Lê et al., 2014] Lê, M., Delingette, H., Kalpathy-Cramer, J., Gerstner, E., Shih, H. A., Batchelor, T., Unkelbach, J., and Ayache, N. (2014). Multimodal analysis of vasogenic edema in glioblastoma patients for radiotherapy planning. In *Workshop Image-Guided Adaptive Radiation Therapy*. (Cited on pages 29, 41, 111 and 115.)
- [Lê et al., 2015a] Lê, M., Delingette, H., Kalpathy-Cramer, J., Gerstner, E. R., Batchelor, T., Unkelbach, J., and Ayache, N. (2015a). Bayesian personalization of brain tumor growth model. In *Medical Image Computing and Computer-Assisted Intervention–MICCAI 2015*, pages 424–432. Springer. (Cited on pages 60, 61, 75, 78, 80, 86, 87, 112 and 116.)
- [Lê et al., 2015b] Lê, M., Unkelbach, J., Ayache, N., and Delingette, H. (2015b). GPSSI: Gaussian Process for Sampling Segmentations of Images. In *Medical Image Computing and Computer-Assisted Intervention–MICCAI 2015*, pages 38–46. Springer. (Cited on pages 80, 83, 84, 112 and 116.)

- [Lê et al., 2016] Lê, M., Unkelbach, J., Ayache, N., and Delingette, H. (2016). Sampling image segmentations for uncertainty quantification. *Medical image analysis*. (Cited on pages 41, 112 and 115.)
- [Lorenzi et al., 2015] Lorenzi, M., Ziegler, G., Alexander, D. C., and Ourselin, S. (2015). Efficient Gaussian process-based modelling and prediction of image time series. In *Information Processing in Medical Imaging*, pages 626–637. Springer. (Cited on page 49.)
- [Louis et al., 2007] Louis, D. N., Ohgaki, H., Wiestler, O. D., Cavenee, W. K., Burger, P. C., Jouvet, A., Scheithauer, B. W., and Kleihues, P. (2007). The 2007 WHO classification of tumours of the central nervous system. *Acta neuropathologica*, 114(2):97–109. (Cited on page 6.)
- [Lu et al., 2004] Lu, S., Ahn, D., Johnson, G., Law, M., Zagzag, D., and Grossman, R. I. (2004). DTI of intracranial neoplasia and associated peritumoral edema: introduction of the tumor infiltration index. *Radiology*, 232(1):221–228. (Cited on page 32.)
- [Mason et al., 2007] Mason, W., Del Maestro, R., Eisenstat, D., Forsyth, P., Fulton, D., Laperrière, N., Macdonald, D., Perry, J., Thiessen, B., Committee, C. G. R., et al. (2007). Canadian recommendations for the treatment of glioblastoma multiforme. *Current Oncology*, 14(3):110. (Cited on pages 1, 15, 58 and 95.)
- [Mazziotta et al., 2001] Mazziotta, J., Toga, A., Evans, A., Fox, P., Lancaster, J., Zilles, K., Woods, R., Paus, T., Simpson, G., Pike, B., et al. (2001). A probabilistic atlas and reference system for the human brain: International Consortium for Brain Mapping (ICBM). *Philosophical Transactions of the Royal Society B: Biological Sciences*, 356(1412):1293–1322. (Cited on page 74.)
- [McInerney and Terzopoulos, 1996] McInerney, T. and Terzopoulos, D. (1996). Deformable models in medical image analysis: a survey. *Medical image analysis*, 1(2):91–108. (Cited on page 43.)
- [MDguidelines, 2014] MDguidelines (2014). Astrocytoma, In MDGuidelines. <http://www.mdguidelines.com/astrocytoma>. Accessed: 20/09/2014. (Cited on page 7.)
- [Menze et al., 2015] Menze, B., Jakab, A., Bauer, S., Kalpathy-Cramer, J., Farahani, K., et al. (2015). The multimodal brain tumor image segmentation benchmark (BRATS). *IEEE Transactions on Medical Imaging*, 34(10):1993–2024. (Cited on pages 27, 56 and 85.)
- [Menze et al., 2011a] Menze, B. H., Stretton, E., Konukoglu, E., and Ayache, N. (2011a). Image-based modeling of tumor growth in patients with glioma. *Optimal control in image processing*. (Cited on pages 18 and 114.)

- [Menze et al., 2011b] Menze, B. H., Van Leemput, K., et al. (2011b). A generative approach for image-based modeling of tumor growth. In *IPMI*, pages 735–747. Springer. (Cited on pages 28, 65 and 66.)
- [Min et al., 2013] Min, Z.-G., Niu, C., Rana, N., Ji, H.-M., and Zhang, M. (2013). Differentiation of pure vasogenic edema and tumor-infiltrated edema in patients with peritumoral edema by analyzing the relationship of axial and radial diffusivities on 3.0 t mri. *Clinical Neurology and Neurosurgery*. (Cited on page 32.)
- [Mirimanoff et al., 2006] Mirimanoff, R.-O., Gorlia, T., Mason, W., Van den Bent, M. J., Kortmann, R.-D., Fisher, B., Reni, M., Brandes, A. A., Curschmann, J., Villa, S., et al. (2006). Radiotherapy and temozolomide for newly diagnosed glioblastoma: recursive partitioning analysis of the EORTC 26981/22981-NCIC CE3 phase III randomized trial. *Journal of Clinical Oncology*, 24(16):2563–2569. (Cited on pages 11 and 15.)
- [Mosayebi et al., 2012] Mosayebi, P., Cobzas, D., Murtha, A., and Jagersand, M. (2012). Tumor invasion margin on the riemannian space of brain fibers. *Medical image analysis*, 16(2):361–373. (Cited on pages 18 and 65.)
- [Murray, 2002] Murray, J. (2002). *Mathematical biology*, volume 2. Springer. (Cited on pages 18 and 64.)
- [Neal et al., 2013] Neal, M. L., Trister, A. D., Ahn, S., Baldock, A., Bridge, C. A., Guyman, L., Lange, J., Sodt, R., Cloke, T., Lai, A., Cloughesy, T. F., et al. (2013). Response classification based on a minimal model of glioblastoma growth is prognostic for clinical outcomes and distinguishes progression from pseudoprogression. *Cancer research*, 73(10):2976–2986. (Cited on page 63.)
- [Neal et al., 2011] Neal, R. M. et al. (2011). MCMC using Hamiltonian dynamics. *Handbook of Markov Chain Monte Carlo*, 2:113–162. (Cited on page 72.)
- [Neumann et al., 2014] Neumann, D., Mansi, T., Georgescu, B., Kamen, A., Kayvanpour, E., Amr, A., Sedaghat-Hamedani, F., Haas, J., Katus, H., Meder, B., et al. (2014). Robust image-based estimation of cardiac tissue parameters and their uncertainty from noisy data. In *Medical Image Computing and Computer-Assisted Intervention–MICCAI 2014*, pages 9–16. Springer. (Cited on pages 28, 66 and 69.)
- [Niethammer et al., 2015] Niethammer, M., Pohl, K. M., Janoos, F., and Wells, III, W. M. (2015). Active mean fields for probabilistic image segmentation: Connections with chan-vese and rudin-osher-fatemi models. *ArXiv e-prints*. (Cited on page 43.)
- [Oden et al., 2013] Oden, J. T., Prudencio, E. E., and Hawkins-Daarud, A. (2013). Selection and assessment of phenomenological models of tumor growth. *Mathematical Models and Methods in Applied Sciences*, 23(07):1309–1338. (Cited on page 80.)

- [Özüğurlu, 2015] Özüğurlu, E. (2015). A note on the numerical approach for the reaction-diffusion problem to model the density of the tumor growth dynamics. *Computers & Mathematics with Applications*, 69(12):1504–1517. (Cited on page 69.)
- [Pedregosa et al., 2011] Pedregosa, F., Varoquaux, G., Gramfort, A., Michel, V., Thirion, B., Grisel, O., Blondel, M., Prettenhofer, P., Weiss, R., Dubourg, V., Vanderplas, J., Passos, A., Cournapeau, D., Brucher, M., Perrot, M., and Duchesnay, E. (2011). Scikit-learn: Machine learning in Python. *Journal of Machine Learning Research*, 12:2825–2830. (Cited on page 34.)
- [Petersen et al., 2010] Petersen, K., Nielsen, M., and Brandt, S. S. (2010). A static SMC sampler on shapes for the automated segmentation of aortic calcifications. In *Computer Vision—ECCV 2010*, pages 666–679. Springer. (Cited on page 43.)
- [Pohl et al., 2006] Pohl, K. et al. (2006). Logarithm odds maps for shape representation. In *Medical Image Computing and Computer-Assisted Intervention—MICCAI 2006*, pages 955–963. Springer. (Cited on page 34.)
- [Pohl et al., 2007] Pohl, K. M., Fisher, J., Bouix, S., Shenton, M., McCarley, R. W., Grimson, W. E. L., Kikinis, R., and Wells, W. M. (2007). Using the logarithm of odds to define a vector space on probabilistic atlases. *Medical Image Analysis*, 11(5):465–477. (Cited on page 44.)
- [Powell, 2009] Powell, M. J. (2009). The BOBYQA algorithm for bound constrained optimization without derivatives. *Cambridge NA Report NA2009/06*. (Cited on pages 28, 65 and 72.)
- [radiologyinfo, 2016] radiologyinfo (2016). Linear accelerator. <http://www.radiologyinfo.org/en/info.cfm?pg=linac>. Accessed: 01/04/2016. (Cited on page 10.)
- [Raman et al., 2016] Raman, F., Scribner, E., Saut, O., Wenger, C., Colin, T., and Fathallah-Shaykh, H. M. (2016). Computational trials: Unraveling motility phenotypes, progression patterns, and treatment options for glioblastoma multiforme. *PLoS ONE*, 11(1):1–26. (Cited on pages 19 and 65.)
- [Rapaka et al., 2012] Rapaka, S., Mansi, T., Georgescu, B., Pop, M., Wright, G. A., Kamen, A., and Comaniciu, D. (2012). LBM-EP: Lattice-boltzmann method for fast cardiac electrophysiology simulation from 3D images. In *Medical Image Computing and Computer-Assisted Intervention—MICCAI 2012*, pages 33–40. Springer. (Cited on pages 69 and 123.)
- [Rasmussen, 2003] Rasmussen, C. E. (2003). Gaussian processes to speed up hybrid Monte Carlo for expensive Bayesian integrals. volume 7, pages 651–659. (Cited on pages 72, 73, 75 and 87.)

- [Ray, 2009] Ray, S. (2009). *Glioblastoma: Molecular Mechanisms of Pathogenesis and Current Therapeutic Strategies*. Springer. (Cited on pages 5 and 9.)
- [Ray-Chaudhury, 2010] Ray-Chaudhury, A. (2010). Pathology of glioblastoma multiforme. In *Glioblastoma*, pages 77–84. Springer. (Cited on pages 7 and 8.)
- [Ribba et al., 2012] Ribba, B., Kaloshi, G., Peyre, M., Ricard, D., Calvez, V., Tod, M., Čajavec-Bernard, B., Idbaih, A., Psimaras, D., Dainese, L., et al. (2012). A tumor growth inhibition model for low-grade glioma treated with chemotherapy or radiotherapy. *Clinical Cancer Research*, 18(18):5071–5080. (Cited on page 17.)
- [Rockne et al., 2009] Rockne, R., Alvord Jr, E., Rockhill, J., and Swanson, K. (2009). A mathematical model for brain tumor response to radiation therapy. *Journal of mathematical biology*, 58(4-5):561–578. (Cited on pages 19, 80 and 83.)
- [Rockne et al., 2010] Rockne, R., Rockhill, J. K., Mrugala, M., Spence, A. M., Kalet, I., Hendrickson, K., Lai, A., Cloughesy, T., Jr, E. C. A., and Swanson, K. R. (2010). Predicting the efficacy of radiotherapy in individual glioblastoma patients in vivo: a mathematical modeling approach. *Physics in Medicine and Biology*, 55(12):3271. (Cited on page 83.)
- [Rockne et al., 2015] Rockne, R. C., Trister, A. D., Jacobs, J., Hawkins-Daarud, A. J., Neal, M. L., Hendrickson, K., Mrugala, M. M., Rockhill, J. K., Kinahan, P., Krohn, K. A., et al. (2015). A patient-specific computational model of hypoxia-modulated radiation resistance in glioblastoma using 18F-FMISO-PET. *Journal of The Royal Society Interface*, 12(103):20141174. (Cited on page 83.)
- [Saatçi, 2012] Saatçi, Y. (2012). *Scalable inference for structured Gaussian process models*. PhD thesis, University of Cambridge. (Cited on page 49.)
- [Sabuncu et al., 2010] Sabuncu, M. R., Yeo, B. T., Van Leemput, K., Fischl, B., and Golland, P. (2010). A generative model for image segmentation based on label fusion. *IEEE Transactions on Medical Imaging*, 29(10):1714–1729. (Cited on page 44.)
- [Saut et al., 2014] Saut, O., Lagaert, J.-B., Colin, T., and Fathallah-Shaykh, H. M. (2014). A multilayer grow-or-go model for gbm: effects of invasive cells and anti-angiogenesis on growth. *Bulletin of mathematical biology*, 76(9):2306–2333. (Cited on pages 19, 22, 23, 65 and 83.)
- [Scribner et al., 2014] Scribner, E., Saut, O., Province, P., Bag, A., Colin, T., and Fathallah-Shaykh, H. M. (2014). Effects of anti-angiogenesis on glioblastoma growth and migration: Model to clinical predictions. *PLoS ONE*, 9(12):1–21. (Cited on pages 19 and 65.)
- [Stretton et al., 2013] Stretton, E., Geremia, E., Menze, B. H., Delingette, H., and Ayache, N. (2013). Importance of patient DTI’s to accurately model glioma

- growth using the reaction diffusion equation. In *IEEE ISBI*, pages 1130–32, San Francisco, CA, United States. IEEE. (Cited on page 67.)
- [Stretton et al., 2012] Stretton, E., Mandonnet, E., Geremia, E., Menze, B. H., Delingette, H., and Ayache, N. (2012). Predicting the location of glioma recurrence after a resection surgery. In *Proceedings of 2nd International MICCAI Workshop on Spatiotemporal Image Analysis for Longitudinal and Time-Series Image Data (STIA'12)*, pages 113–123. Springer. (Cited on pages 19 and 83.)
- [Stupp et al., 2002] Stupp, R., Dietrich, P.-Y., Kraljevic, S. O., Pica, A., Miallard, I., Maeder, P., Meuli, R., Janzer, R., Pizzolato, G., Miralbell, R., et al. (2002). Promising survival for patients with newly diagnosed glioblastoma multiforme treated with concomitant radiation plus temozolomide followed by adjuvant temozolomide. *Journal of Clinical Oncology*, 20(5):1375–1382. (Cited on page 11.)
- [Swanson et al., 2003] Swanson, K., Alvord, E., and Murray, J. (2003). Virtual resection of gliomas: effect of extent of resection on recurrence. *Mathematical and Computer Modelling*, 37(11):1177–1190. (Cited on page 83.)
- [Swanson et al., 2011] Swanson, K., Rockne, R., Claridge, J., Chaplain, M., Alvord Jr, E., and Anderson, A. (2011). Quantifying the role of angiogenesis in malignant progression of gliomas: In silico modeling integrates imaging and histology. *Cancer research*, 71(24):7366–7375. (Cited on pages 19, 22 and 65.)
- [Swanson et al., 2008] Swanson, K., Rostomily, R., and Alvord, E. (2008). A mathematical modelling tool for predicting survival of individual patients following resection of glioblastoma: a proof of principle. *British journal of cancer*, 98(1):113–119. (Cited on pages 19 and 93.)
- [Swanson et al., 2000] Swanson, K. R., Alvord, E., and Murray, J. (2000). A quantitative model for differential motility of gliomas in grey and white matter. *Cell proliferation*, 33(5):317–329. (Cited on page 17.)
- [Swanson et al., 2002] Swanson, K. R., Alvord, E., and Murray, J. (2002). Virtual brain tumours (gliomas) enhance the reality of medical imaging and highlight inadequacies of current therapy. *British journal of cancer*, 86(1):14–18. (Cited on pages 18 and 64.)
- [Tofts, 2003] Tofts, P. (2003). *Quantitative MRI of the brain: measuring changes caused by disease*. John Wiley & Sons. (Cited on page 13.)
- [Toivanen, 1996] Toivanen, P. J. (1996). New geodesic distance transforms for gray-scale images. *Pattern Recognition Letters*, 17(5):437–450. (Cited on page 46.)
- [Tracqui et al., 1995] Tracqui, P., Cruywagen, G., Woodward, D., Bartoo, G., Murray, J., and Alvord, E. (1995). A mathematical model of glioma growth: the effect of chemotherapy on spatio-temporal growth. *Cell proliferation*, 28(1):17–31. (Cited on pages 18, 19, 64, 83 and 114.)

- [Unkelbach et al., 2014a] Unkelbach, J., Menze, B. H., Konukoglu, E., Dittmann, F., Ayache, N., and Shih, H. A. (2014a). Radiotherapy planning for glioblastoma based on a tumor growth model: implications for spatial dose redistribution. *Physics in medicine and biology*, 59(3):771. (Cited on pages 19, 80, 83, 89, 90 and 91.)
- [Unkelbach et al., 2014b] Unkelbach, J., Menze, B. H., Konukoglu, E., Dittmann, F., Le, M., Ayache, N., and Shih, H. A. (2014b). Radiotherapy planning for glioblastoma based on a tumor growth model: improving target volume delineation. *Physics in medicine and biology*, 59(3):747. (Cited on pages 19, 36, 80, 83, 88, 89, 90 and 116.)
- [Vese and Chan, 2002] Vese, L. A. and Chan, T. F. (2002). A multiphase level set framework for image segmentation using the Mumford and Shah model. *International journal of computer vision*, 50(3):271–293. (Cited on page 52.)
- [Walker et al., 1978] Walker, M. D., Alexander Jr, E., Hunt, W. E., MacCarty, C. S., Mahaley Jr, M. S., Mealey Jr, J., Norrell, H. A., Owens, G., Ransohoff, J., Wilson, C. B., et al. (1978). Evaluation of BCNU and/or radiotherapy in the treatment of anaplastic gliomas: a cooperative clinical trial. *Journal of neurosurgery*, 49(3):333–343. (Cited on page 10.)
- [Walker et al., 1979] Walker, M. D., Strike, T. A., and Sheline, G. E. (1979). An analysis of dose-effect relationship in the radiotherapy of malignant gliomas. *International Journal of Radiation Oncology Biology Physics*, 5(10):1725–1731. (Cited on page 10.)
- [Wang et al., 2013] Wang, C., Komodakis, N., and Paragios, N. (2013). Markov random field modeling, inference & learning in computer vision & image understanding: A survey. *Computer Vision and Image Understanding*, 117(11):1610–1627. (Cited on page 43.)
- [Wang et al., 2009] Wang, C. H., Rockhill, J. K., Mrugala, M., Peacock, D. L., Lai, A., Jusenius, K., Wardlaw, J. M., Cloughesy, T., Spence, A. M., et al. (2009). Prognostic significance of growth kinetics in newly diagnosed GBM revealed by combining serial imaging with a novel biomathematical model. *Cancer research*, 69(23):9133–9140. (Cited on page 63.)
- [Warfield et al., 2004] Warfield, S. K., Zou, K. H., and Wells, W. M. (2004). Simultaneous truth and performance level estimation (STAPLE): an algorithm for the validation of image segmentation. *IEEE Transactions on Medical Imaging*, 23(7):903–921. (Cited on page 44.)
- [Welsh, 2010] Welsh, C. T. (2010). Molecular mechanisms of pathogenesis in glioblastoma and current therapeutic strategies. In *Glioblastoma*, pages 85–93. Springer. (Cited on page 8.)

- [Williams and Rasmussen, 2006] Williams, C. K. and Rasmussen, C. E. (2006). Gaussian processes for machine learning. *Cambridge: MIT Press*. (Cited on pages 47, 55 and 74.)
- [Williams and Fitzgibbon, 2007] Williams, O. and Fitzgibbon, A. (2007). Gaussian process implicit surfaces. In *Gaussian Process in Practice*. (Cited on page 46.)
- [Yoshida and Nagaoka, 2010] Yoshida, H. and Nagaoka, M. (2010). Multiple-relaxation-time lattice boltzmann model for the convection and anisotropic diffusion equation. *Journal of Computational Physics*, 229(20):7774–7795. (Cited on pages 86, 123 and 125.)
- [Yu et al., 2003] Yu, D., Mei, R., Luo, L.-S., and Shyy, W. (2003). Viscous flow computations with the method of lattice boltzmann equation. *Progress in Aerospace Sciences*, 39(5):329–367. (Cited on pages 86, 123, 124 and 125.)
- [Zhang and Tsai, 2007] Zhang, D. and Tsai, J. J. (2007). *Advances in machine learning applications in software engineering*. Igi Global. (Cited on page 34.)
- [Zhang et al., 2001] Zhang, Y., Brady, M., and Smith, S. (2001). Segmentation of brain mr images through a hidden markov random field model and the expectation-maximization algorithm. *IEEE Transactions on Medical Imaging*, 20(1):45–57. (Cited on pages 26 and 69.)
- [Zhao et al., 1996] Zhao, H.-K., Chan, T., Merriman, B., and Osher, S. (1996). A variational level set approach to multiphase motion. *Journal of computational physics*, 127(1):179–195. (Cited on page 52.)
- [Zhao et al., 2010] Zhao, L., Ruotsalainen, U., Hirvonen, J., Hietala, J., and Tohka, J. (2010). Automatic cerebral and cerebellar hemisphere segmentation in 3D MRI: adaptive disconnection algorithm. *Medical image analysis*, 14(3):360–372. (Cited on page 69.)

Brain Tumor Growth Modeling, Application to Radiotherapy

Abstract.

Glioblastomas are among the most common and aggressive primary brain tumors. It is usually treated with a combination of surgical resection, followed with concurrent chemo- and radiotherapy. However, the infiltrative nature of the tumor makes its control particularly challenging.

Biophysical model personalization allows one to automatically define patient specific therapy plans which maximize survival rates. In this thesis, we focused on the elaboration of tools to personalize radiotherapy planning.

First, we studied the impact of taking into account the vasogenic edema into the planning. We studied a database of patients treated with anti-angiogenic drug, revealing a posteriori the presence of the edema.

Second, we studied the relationship between the uncertainty in the tumor segmentation and dose distribution. For that, we present an approach in order to efficiently sample multiple plausible segmentations from a single expert one.

Third, we personalized a tumor growth model to seven patients' MR images. We used a Bayesian approach in order to estimate the uncertainty in the personalized parameters of the model.

Finally, we showed how combining a personalized model of tumor growth with a dose response model could be used to automatically define patient specific dose distribution.

The promising results of our approaches offer new perspectives for personalized therapy planning.

KEY WORDS: Medical imaging, biophysical model, personalization, radiotherapy, segmentation, uncertainty
